A STUDY OF EXLUSIVE FINAL STATES IN RADIATIVE ψ DECAYS

Thesis by

Charles David Edwards, Jr.

In Partial Fulfillment of the Requirements

for the Degree of

Doctor of Philosophy

California Institute of Technology

Pasadena, California

1985

(Submitted June, 1984)

ABSTRACT

Using the Crystal Ball Detector at the SPEAR e^+e^- storage ring of the Stanford Linear Accelerator Center, several exclusive final states in radiative ψ decays are studied. Signals are observed for the processes $\psi \to \gamma\pi^0$, $\gamma\gamma\rho^0$, and $\gamma\rho^+\rho^-$, and an upper limit is placed on the decay rate for $\psi \to \eta\eta'$. Experimental results are discussed in light of previous results in radiative ψ decays, and with respect to theoretical predictions for gluonic mesons.

Acknowledgments

It is impossible to adequately thank all the people who contributed to: a) this thesis, b) my education, and c) my general well-being over the last five years. Nevertheless, I must mention several people to whom I owe a great deal. First of all, I want to thank the entire Crystal Ball Collaboration, without whose exceptional efforts this work could not have been accomplished. High energy physics is indeed a collaborative effort, and one could not hope to find a better group of people with whom to work. In particular, Richard Partridge was a constant source of new ideas; his enthusiasm about ψ physics made this work both exciting and enjoyable. Frank Porter was a veritable wealth of knowledge about all aspects of the experiment, and was particularly helpful in introducing me to the many subtleties of kinematic fitting. Peter Ratoff provided many helpful discussions, and was instrumental in carrying out the arduous task of bringing up the Crystal Ball software at Caltech, allowing this analysis to be carried out locally.

I want to particulary thank my advisor, Charles Peck, for five years of patience and help. He gave me countless suggestions throughout the course of this work, and taught me a wealth of physics along the way. I am also very grateful that he managed to convince me to participate in the installation of the Crystal Ball at DESY; that was a most valuable experience. I can only hope that some of his high standards for accurate and thorough work have rubbed off on me.

On the home front, my roommate Chris made life in smoggy Pasadena bearable, and provided some comic relief during the off-hours. Jim, Les, Dave, Bryant, and Joel gave me the chance to pursue my musical goals, far beyond my expectations. Finally, Sandra's friendship supported me from Pasadena to Palo Alto to Hamburg and back.

I thank the Schlumberger Foundation for my first year of financial support, and I thank Caltech and the Department of Energy for the remainder.

To my parents, I am forever indebted to you for the education you made possible for me. This thesis is for you.

Table of Contents

Abstract ii

Acknowledgments iii

1. Introduction 1

References 9

2. The Crystal Ball Experiment 11

2.1 Introduction 11

2.2 The Detector 11

2.3 Experimental Triggers 19

2.4 Data Analysis 21

2.5 Hadron Selection 25

2.6 PIFIT 27

2.7 Selection of Exclusive Final States 35

2.8 Kinematic Fitting 37

References 40

3. Observation of the Decay $\psi \rightarrow \gamma\pi^0$ 41

3.1 Introduction and History 41

3.2 Flavor SU(3) and Vector Dominance 41

3.3 Experimental Analysis 44

3.4 Systematic Errors 53

3.5 Background Checks 57

3.6 Conclusions 58

References 60

4. A Study of the Cascade Decay $\psi \to \gamma X$, $X \to \gamma\rho$ 61

4.1 Introduction 61

4.2 The $\iota(1440)$ and Pseudoscalar Mixing Models 61

4.3 Experimental Analysis 65

4.4 Angular Distributions 86

4.5 Observations by Other Experiments 92

4.6 Conclusions 95

References 97

5. $\psi \to \gamma\rho^+\rho^-$ 98

5.1 Introduction 98

5.2 Experimental Analysis of the $\gamma\pi^+\pi^-\pi^0\pi^0$ Final State 101

5.3 Extraction of the $\rho\rho$ Mass Spectrum 107

5.4 Determination of J^P for the $\rho\rho$ Enhancement 118

5.5 Conclusions 130

References 131

6. A Search for the Decay $\psi \to \gamma\eta\eta'$ 132

6.1 Introduction 132

6.2 Theoretical Predictions 132

6.3 Experimental Analysis 135

6.4 Conclusions 148

References 149

Chapter I

Introduction

Over the last decade, a large number of experimental results have provided evidence supporting the validity of Quantum Chromodynamics (QCD) as the correct theory for describing the strong interactions of hadrons. And yet one of the most fundamental features of the theory remains only indirectly confirmed: namely, the non-Abelian character of the color gauge group SU(3). Both Quantum Electrodynamics (QED) and QCD are gauge theories, in which the fundamental quantum of interaction, the photon for QED and the gluon for QCD, can be understood as a consequence of the local gauge invariance of the theory. The Abelian nature of the gauge group U(1) of QED manifests itself in the fact that the photon carries no charge, and hence does not couple to other photons. For QCD, on the other hand, the gauge group SU(3) is non-Abelian. Physically, this means that the gluons carry the color charge, and thus can couple directly to other gluons. This effect is responsible for the ultraviolet screening of the color charge in QCD, also known as asymptotic freedom [1.1]. One of the other predicted consequences of colored gluons is the possible existence of bound states of gluons [1.2], often referred to as gluonia or glueballs. Observation of such particles would provide a striking and very direct verification of the non-Abelian nature of QCD.

Based on perturbative QCD calculations, several authors have proposed looking for glueballs in the radiative decays of heavy quarkonia such as the ψ [1.3]. The basic hadronic decay of the ψ is shown in Figure 1.1a. The charmed quark and antiquark of the ψ annihilate, producing three gluons in the process. The decay into one gluon is forbidden because a single gluon is a color octet,

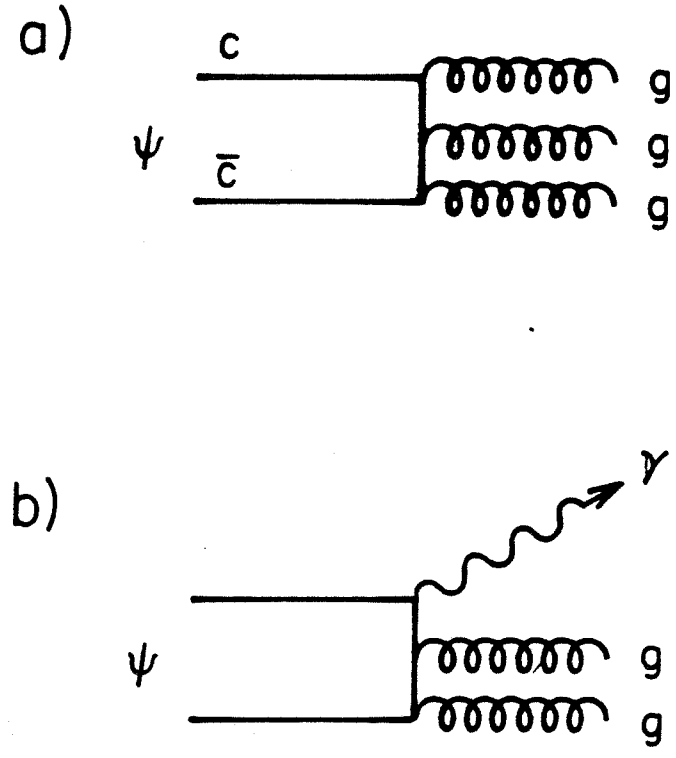

Figure 1.1: a) The three gluon diagram of the ψ; in QCD perturbation theory, this is the leading order diagram for the decay of the ψ into hadrons; b) Radiative ψ decay corresponds to replacing one of the gluons in Fig. 1.1a with a photon.

while the ψ, and all known observable particles, are color singlets. Charge conjugation invariance forbids the decay of the ψ into a color singlet combination of two gluons. Thus three gluons are the minimum number allowed in the decay of the ψ. Assuming that the gluons fragment into hadrons with unit probability, the hadronic decay rate of the ψ should go as the third power of the strong running coupling constant α_s. The observed narrow width of the ψ, 63 KeV [1.4], indicates that at the ψ mass of roughly 3 GeV, we are in a regime in which α_s is fairly small (roughly equal to 0.2), due to the effects of asymptotic freedom.

With this in mind, we consider the radiative ψ decay in Figure 1.1b, in which one of the gluons is replaced by a photon. The ratio of amplitudes for this radiative graph compared to the three gluon decay has been calculated [1.5], with the result

$$\frac{\Gamma(\psi \to \gamma gg)}{\Gamma(\psi \to ggg)} = \frac{16}{5}\frac{\alpha}{\alpha_s}.$$

Numerically, the ratio is about 10% for the value of α_s corresponding to the momentum scale of ψ decays. Thus radiative decays are predicted to account for a substantial portion of the total ψ decay width. Returning to Figure 1.1, we make one more important observation. For the three gluon decay, any pair of gluons is in a color octet. This is because each individual gluon is in an octet representation, while the three gluon final state must be a color singlet. On the other hand, the two gluons in the radiative decay are in a color singlet state. Given the fact that gluons can interact by exchanging gluons, we see that this color singlet gluon pair can resonate as a gluonium state. The mass of the gluonic system is reflected in the energy of the radiative photon, and thus a measurement of the photon spectrum in radiative ψ decays acts as a glueball probe.

Turning this argument around, any new particle produced copiously in radiative ψ decays should be considered as a possible gluonium candidate. However, once such an observation is made, how does one decide if the new particle is indeed a glueball? Unfortunately, at this time the theoretical picture of gluonium is very clouded.

Several different theoretical approaches have been used to study gluonium. Potential models seek to understand the spectrum of glueball states by endowing the gluons with an effective mass and introducing a static intergluon potential motivated by QCD gluon-gluon couplings [1.6]. Lattice calculations provide a non-perturbative approach to the solution of the QCD field equations [1.7]. Finally, the bag model approach solves the problem of confinement through the *ad-hoc* introduction of "bag" boundary conditions [1.8].

While the detailed structure of the gluonium spectrum varies between the different models, the overall features agree quite well, with each model predicting that the lowest lying glueball states should populate the 1-2 GeV region. As an example, Table 1.1 displays the spectrum of lowest mass glueballs based on the lattice calculations of reference [1.9].

Table 1.1: Lattice Glueball Masses [1.9]

J^{PC}	Mass (MeV)
0^{++}	770 ± 30
0^{-+}	1450^{+240}_{-150}
2^{++}	1665^{+110}_{-87}
1^{-+}	1800 ± 230

In addition to the errors listed, there is an overall 15% systematic error for all masses based on the uncertainty in the value of the QCD scale parameter Λ, which was taken to be 200 MeV for these results.

The predictions for glueball widths are much less consistent. The "$\sqrt{OZI}$" rule [1.10] maintains that glueballs should have decay widths on the order of tens of MeV. The argument is based on the fact that while OZI-suppressed processes require the annihilation of the initial $q\bar{q}$ state, followed by the subsequent production of a new $q\bar{q}$ pair, glueball decay simply requires the production of a $q\bar{q}$ pair. Thus the suppression of glueball decay rates relative to the typical allowed hadronic rates should be roughly the square root of the suppression for OZI-forbidden hadronic decays. With OZI-allowed rates of order 100 MeV, and OZI-suppressed rates of order one MeV, this approach predicts glueball decay rates of order ten MeV. Explicit QCD calculations of glueball decays [1.11], however, obtain much smaller decay widths, on the order of 1 MeV.

Another early prediction for glueball decays was that they should preserve flavor SU(3) symmetry and thus, since a glueball is a flavor SU(3) singlet, have flavor independent couplings. Explicit calculations have shown, however, that this is not always the case. For instance, in the decay of a pseudoscalar glueball, helicity factors cause the decay rate to be proportional to the square of the final state quark mass, introducing large flavor symmetry breaking in the decay amplitude and thereby favoring $K\bar{K}$ over $\pi\pi$ decays.

The final, and perhaps most significant, complication in the theoretical understanding of gluonium is the problem of glueball-$q\bar{q}$ mixing. All J^{PC} combinations can be formed from glueball states with two or three gluons. Most of the low mass glueball states have J^{PC} quantum numbers which are also allowed for $q\bar{q}$ mesons. For a $q\bar{q}$ pair with angular momentum L and spin S, we have $P=(-1)^{1+L}$ and $C=(-1)^{L+S}$. This permits the three spin parity sequences:

$$J=j,\ P=(-1)^{j+1},\ C=(-1)^{j} \qquad (j=0,1,\cdots)$$
$$J=j,\ P=(-1)^{j},\ C=(-1)^{j} \qquad (j=0,1,\cdots)$$
$$J=j,\ P=(-1)^{j+1},\ C=(-1)^{j+1} \qquad (j=1,2,\cdots)$$

The state $J^{PC}=0^{--}$, and the sequence $J^{PC} = 0^{+-}, 1^{-+}, 2^{+-}, 3^{-+}, \cdots$ are not allowed for $q\bar{q}$ mesons. Such states, with quantum numbers which are forbidden for $q\bar{q}$ mesons, are known as "oddballs," and would provide very compelling evidence for glueballs. For glueball states with quantum numbers which are allowed for $q\bar{q}$ mesons, the glueball and quarkonic meson states can and in principle will mix, yielding physical states which are combinations of quark and glue. Such mixing can affect the masses, widths, and decay patterns of the physical states.

What, then, is the experimental signature of a glueball? First of all, the existence of a glueball introduces an extra state into the meson spectrum, regardless of how the various quarkonic and gluonic mesons mix. Let us take the pseudoscalar mesons as an example. If a pseudoscalar glueball exists, then we should find an extra 0^- state in addition to the nonet of $q\bar{q}$ mesons. The pure glueball, call it G_0, will mix with the pure isoscalar mesons η_0 and η'_0, generating the physical states G, η, and η'. To untangle this state of affairs, it is necessary to combine our theoretical understanding of the unmixed states with a full mixing model to determine the behavior of the true physical states. Such analyses typically require a large number of experimental observations to adequately constrain the model.

Given this state of affairs, the best strategy for proceeding experimentally is to make accurate measurements of resonance properties (mass and width) for new states, measure the spin and parity of these new states, and look for as many decay modes as possible, in an effort to accumulate enough experimental results to adequately constrain and test the glueball hypothesis.

Table 1.2 States Observed in $\psi \to \gamma X$ [1.4],[1.12]
(Prior to work reported in this thesis)

X	Observed Final State	$J^P(X)$	$BF(\psi \to \gamma X)$
π^0	$\gamma\gamma$	0^-	$(7.3\pm4.7)\times10^{-5}$
η	$\gamma\gamma$	0^-	$(8.55\pm0.86)\times10^{-4}$
η'	$\gamma\rho$, $\gamma\gamma$, $\gamma\gamma\pi^+\pi^-$	0^-	$(3.55\pm0.46)\times10^{-3}$
$\iota(1440)$	$\gamma K\bar{K}\pi$	0^- preferred	$(4.2\pm1.2)\times10^{-3}/\ BF(\iota \to K\bar{K}\pi)$
f	$\gamma\pi\pi$	2^+	$(1.51\pm0.35)\times10^{-3}$
f'	γK^+K^-	2^+	$(1.60\pm0.65)\times10^{-4}$
$\theta(1700)$	$\gamma\eta\eta$ $\gamma K\bar{K}$	2^+ preferred	$(3.8\pm1.6)\times10^{-4}/\ BF(\theta \to \eta\eta)$ $(5.2\pm1.4)\times10^{-4}/\ BF(\theta \to K\bar{K})$
$\xi(2200)$	$\gamma K\bar{K}$	?	$(1.60\pm0.72)\times10^{-4}/\ BF(\xi \to K\bar{K})$
$\rho^0\rho^0$ (Mass < 2 GeV)	$\gamma\pi^+\pi^-\pi^+\pi^-$	?	$(1.25\pm0.75)\times10^{-3}$
$[\eta\pi\pi](1700)$	$\gamma\eta\pi\pi$	?	$(3.3\pm0.7)\times10^{-3}$

Presently, a large number of states have been observed in radiative ψ decays. In Table 1.2 we list these states, along with the decay modes in which they have been observed, and their spin and parity quantum numbers. These results do not include measurements to be reported in this thesis. Many of the states seen in radiative ψ decays are well-known particles such as the π^0, η, and f. However, several previously unknown states have been observed in radiative ψ decays. The $\iota(1440)$ and the $\theta(1700)$, for instance, were both discovered in radiative ψ decays, and based on their large production rates, they are leading candidates to be the $J^{PC} = 0^{-+}$ and 2^{++} gluonium states. If these spin parity assignments are correct, then the ι would mix with the η and η', while the θ would mix with the f and f'.

Other new structures found in radiative ψ decays include the very broad enhancement in $\eta\pi\pi$ seen by the Crystal Ball [1.13]. New results by the Mark III [1.14] seem to indicate that this structure is probably a superposition of several resonances. The $\rho\rho$ enhancement seen near 1700 MeV in $\psi\to\gamma 4\pi$ by the Mark II experiment [1.15] is suggestively close in mass and width to the resonance parameters of the $\theta(1700)$. Finally, the remarkably narrow state $\xi(2200)$, observed by the Mark III in $\psi\to\gamma K^+K^-$ [1.14], has sparked a number of theoretical interpretations, from ordinary $q\bar{q}$ meson to glueball to Higgs.

In this thesis, we will explore several new final states in an effort to add to this list. In Chapter 3, we will search for the decay $\psi\to\gamma\pi^0$, which has been observed only with large statistical and systematic errors up until now. In Chapter 4, we will study the $\gamma\gamma\pi^+\pi^-$ final state, in a search for radiative decays of the ι. Chapter 5 reports the results of a spin-parity analysis of the $\rho\rho$ enhancement near 1700 MeV observed in radiative ψ decays. Finally, in Chapter 6 we place a limit on the decay $\theta(1700)\to\eta\eta'$. Hopefully, these results can contribute towards establishing a clearer understanding of the spectrum of mesons seen in radiative ψ decays.

Chapter I References

[1.1] D. Politzer, Phys. Rep. 14C, 129 (1974).

[1.2] K. Wilson, Phys. Rev. D10, 2445 (1974); H. Fritzsch and P. Minkowski, Nuovo Cimento 30A, 393 (1975); P. Freund and Y. Nambu, Phys. Rev. Lett. 34, 1645 (1975); J. Kogut and L. Susskind, Phys. Rev. 16, 395 (1975); K. Johnson, Phys. Lett. 73B, 203 (1978).

[1.3] S. Brodsky, T. DeGrand, R. Horgan, and D. Coyne, Phys. Lett 73B, 203 (1978); K. Koller and T. Walsh, Nucl. Phys. B140, 449,(1978).

[1.4] Rev. of Mod. Phys. 56, S1 (1984).

[1.5] M. Chanowitz, Phys. Rev. D12, 918 (1975).

[1.6] D. Robson, Nucl. Phys. B130, 328 (1977); J. Coyne, P. Fishbane, and S. Meshkov, Phys. Lett. 91B, 259 (1980).

[1.7] K. Wilson, Phys. Rev. D10, 2445 (1974); J. Kogut, D. Sinclair, and L. Susskind, Nucl. Phys B114, 199 (1976);

[1.8] R. Jaffe and K. Johnson, Phys. Rev. Lett. 34, 1645 (1980); J. Donoghue, K. Johnson, and B. A. Li, Phys. Lett. 99B, 416 (1981).

[1.9] K. Ishikawa, G. Schierholz, and M. Teper, Phys. Lett. 116B, 429 (1982); K. Ishikawa, G. Schierholz, and M. Teper, Phys. Lett. 120B, 387 (1983); B. Berg and A. Billoire, Phys. Lett. 113B, 65 (1982); B. Berg and A. Billoire, Phys. Lett. 114B, 324 (1982);

[1.10] D. Robson, Nucl. Phys. B130,328 (1977);

[1.11] C. Carlson, J. Coyne, P. Fishbane, F. Gross, and S. Meshkov, Phys. Rev. D23, 2765 (1891).

[1.12] The θ mass listed here is higher than the value of 1690 MeV listed in the Reference [1.4], reflecting a new fit of the Crystal Ball data which includes a contribution from $f' \to \eta\eta$, as described in D. L. Scharre, Proceedings of the Orbis Scientiae, 1982, Coral Gables, Florida; also SLAC-PUB-2880 (1982).

[1.13] C. Edwards *et al.*, Phys. Rev. Lett. 51, 859 (1983).

[1.14] W. Toki *et al.*, "MARK III Results from SPEAR", SLAC-PUB-3262, 1983.

[1.15] D. Burke, *et al.*, Phys. Rev. Lett. 49, 632 (1982).

Chapter II

The Crystal Ball Experiment

2.1 Introduction

During the period 1978-1981, the Crystal Ball detector was located in the East pit of the SPEAR e^+e^- storage ring at the Stanford Linear Accelerator Center (SLAC). During that time data were collected at center of mass energies ranging from 3.095 up to 7.4 GeV. The $\psi(3095)$ data analyzed here were collected during three separate running periods: Fall 1978, Spring 1979, and Fall 1980. These data represent an integrated luminosity of 765 nb^{-1} and a total of 2.17×10^6 produced ψ events.

Before proceeding to present results for the analysis of several exclusive final states in radiative ψ decays, it is helpful to review some of the basic properties of the Crystal Ball detector. We will briefly summarize the various components of the detector, commenting on both their resolution and efficiency, and on any systematic effects they may introduce into physics analyses. More detailed descriptions of the detector can be found elsewhere [2.1]. Then we will examine some of the analysis tools which are used throughout this work.

2.2 The Detector

The Crystal Ball detector is illustrated in Figure 2.1. The basic detector components are listed below:

a. The main ball, an array of 672 NaI(Tl) crystals

b. Central tracking chambers

c. Endcap crystals and tracking chambers

d. Luminosity monitor

e. Outer Hadron-Muon Separator (OHMS)

2.2a The Main Ball

The primary component of the Crystal Ball is a segmented spherical array of 672 NaI(Tl) crystals. The geometry of the array is based on an icosahedron, as depicted in Figure 2.2. Each of the 20 triangular faces of the icosahedron, which are referred to as "major triangles," is subdivided into four "minor triangles." In turn, each of these minor triangles is subdivided into nine triangular crystals, or "modules." The vertices of these modules are then projected onto the surface of the sphere circumscribing the icosahedron. The resulting array of 720 crystals contains only 11 distinct crystal shapes. To allow for the passage of the e^+e^- beams through the detector, 24 crystals have been removed from each end of the array, leaving 93% of the solid angle covered by the main ball. The crystals adjacent to these openings are called "tunnel modules."

The crystals comprising the main ball are 16 inches in length, corresponding to 15.7 radiation lengths of NaI. The crystals are in the shape of truncated pyramids: the inner face has an area of roughly 1.7 sq. in., while the outer face has an area of 11.8 sq. in. Individual crystals are optically isolated by a wrapping of aluminized foil. Each crystal is viewed from its outer end by a two inch diameter phototube, which is equipped with two light sources for stability and linearity measurements of the phototube and associated data acquisition system. One source is an LED, while the other source is a fiber optic cable which is

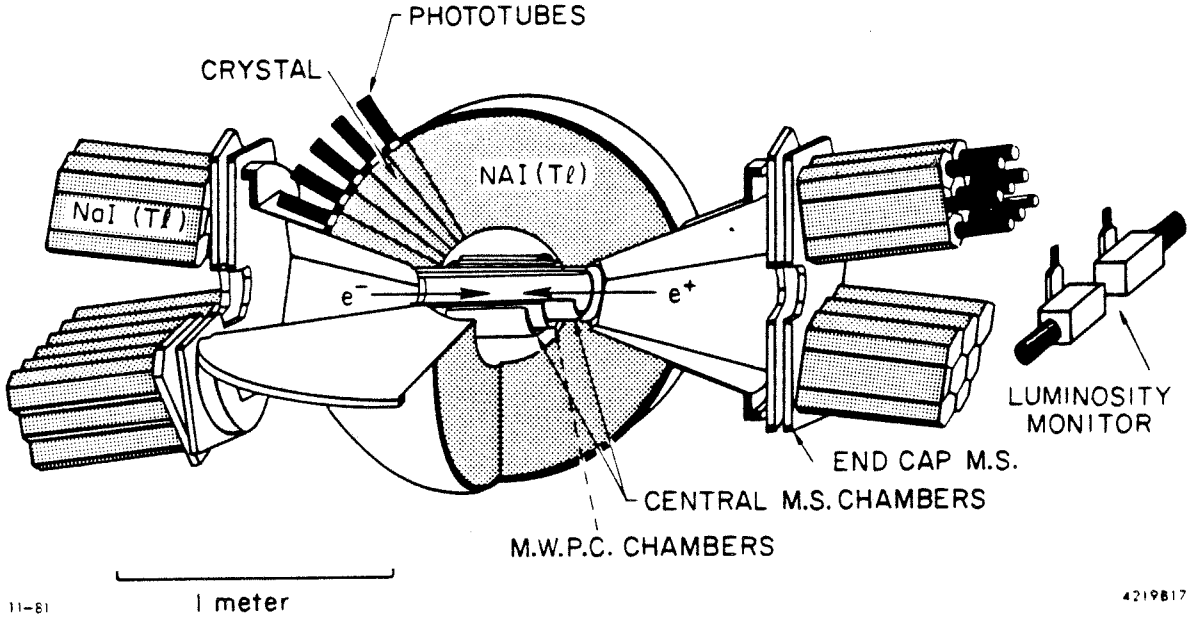

Figure 2.1: An overview of the Crystal Ball detector.

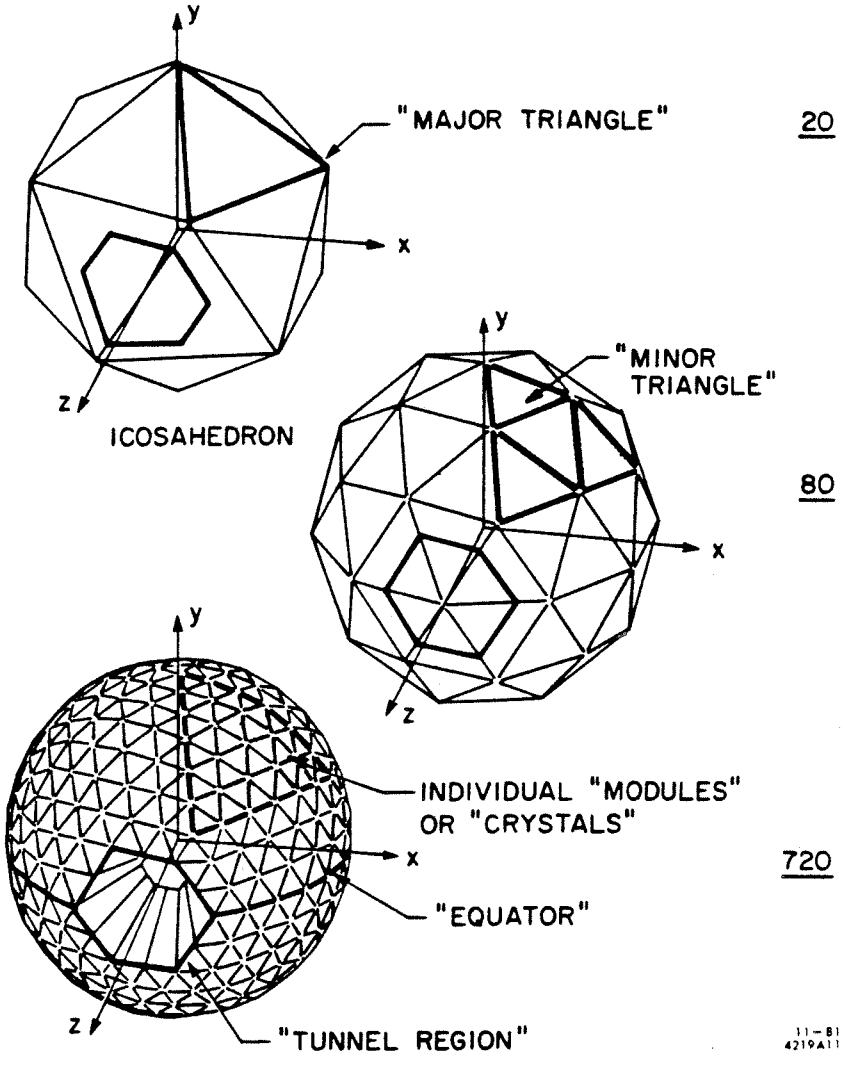

Figure 2.2: Geometry of the crystal array for the main ball.

illuminated by a Xenon flash tube.

The NaI(Tl) crystals provide excellent energy resolution for showering electromagnetic particles (γ's and e's). As a function of energy of the showering particle, the resolution is parametrized by the relation

$$\frac{\sigma_E}{E} = 2.6\% \times E(\mathrm{GeV})^{-1/4}.$$

For the energies of interest, photostatistics do not contribute significantly to the resolution. For instance, consider a 1 GeV photon. Assuming 15% of the dE/dx ionization energy is converted into scintillation light [2.2], and using the fact that the emitted light has an energy of 3 eV, one expects 5×10^7 scintillation photons to be created by a 1 GeV shower. With a 4% transmission efficiency for the light to reach the phototube, and a 20% photocathode efficiency, 4×10^5 photoelectrons will be generated, giving a contribution of only 0.16% to the energy resolution due to photoelectron statistics. The primary contributions to the resolution are fluctuations in the shower leakage out of the crystals, losses in non-active material (such as the actual container which holds the crystals in their array), and intercalibration errors between phototubes.

For hadronic particles, the crystals present a thickness of approximately one hadronic interaction length, implying that roughly 2/3 of all hadrons will interact in the NaI(Tl) and initiate a hadronic shower, much of which will leak out the rear of the crystals. Thus energy measurements cannot be reliably made for hadrons. For those charged hadrons which do not interact, as well as for muons, only dE/dx energy loss will be deposited in the crystals. For a thickness of 16 inches of NaI(Tl), the distribution of energy deposited by a minimum ionizing particle peaks near 210 MeV. Nearly all of this energy will typically be deposited in a single crystal.

Also of interest is the angular resolution of the ball for electromagnetic and hadronic tracks. Since minimum ionizing charged particles leave most of their energy in a single crystal, the angular resolution is intrinsically limited to the size of a crystal, corresponding to an angular error of roughly 70 mr. Photons and electrons have showers which typically spread over the order of ten crystals. Examination of the "shower profile," the actual pattern of energy deposition within these crystals, allows a more accurate determination of track direction for these electromagnetic showering particles. The actual resolution ranges from 25 to 40 mr, with the best resolution for high energy tracks. For interacting hadronic particles, the large fluctuations in shower shape reduce the resolution obtainable by examining the shower profile to approximately 60 mr.

Calibration of the energy scale for the phototubes was achieved with a combination of three methods. Every two weeks during running periods, a calibration was performed using monochromatic 661 KeV photons from a Cs^{137} source. In addition, a monthly calibration was conducted using a Van de Graaff accelerator to initiate the reaction $^{19}F(p,\alpha)\rightarrow{}^{16}O^{*}$, and subsequently observing the monochromatic 6.13 MeV photon resulting from the $^{16}O^{*}$ decay. Finally, large angle Bhabha events were used as a third source to correct the calibrations on a week-to-week basis.

2.2b Central Tracking Chambers

Figure 2.3 depicts the central tracking chambers, consisting of an inner magnetostrictive spark chamber (MSSC), followed by a multiwire proportional counter (MWPC), followed finally by an outer MSSC. Each of the MSSC's contains two spark gaps, and the MWPC contains two anode wire planes and two cathode strip planes. The inner and outer MSSC's cover, respectively, 94% and 71% of the

full solid angle, while the MWPC covers 83%. Table 2.1 shows the resolution of the central chamber components [2.3]. The two gaps in the MWPC have different polar resolutions due to the different geometry of their cathode strips.

Table 2.1 Central Tracking Chamber Parameters

Chamber	Solid Angle Coverage	FWHM Azimuthal Resolution	FWHM Polar Resolution
Inner MSSC	94%	25±5 mr	150±20 mr
MWPC Gap 1	83%	35±2 mr	95-100 mr
MWPC Gap 2	83%	35±2 mr	75-137 mr
Outer MSSC	71%	25±5 mr	115±15 mr

Conversion of photons into e^+e^- pairs in the beam pipe or the chambers can cause photons to appear as charged tracks. For normal incidence, the thicknesses of the various components are: $0.019 X_0$ for the beampipe; $0.02 X_0$ for each MSSC; $0.0035 X_0$ for the MWPC (where X_0 is one radiation length). Thus less than 5% of all photons will be misidentified as charged particles due to conversion in the beampipe.

2.2c Endcap Crystals and Tracking Chambers

As mentioned earlier, 24 crystals have been removed from each end of the main ball to allow for the passage of the beam pipe, reducing the solid angle coverage of the main ball to 93%. To remedy this, 60 hexagonal NaI(Tl) crystals, each 20 radiation lengths thick, have been installed around the beam pipe openings to the ball. These endcaps extend the coverage of the NaI(Tl) to 98% of 4π sr. In front of the endcap crystals is a double-gapped planar MSSC, extending the coverage of the central chambers. In this analysis, endcap information was only used to veto events with tracks lying outside the main ball.

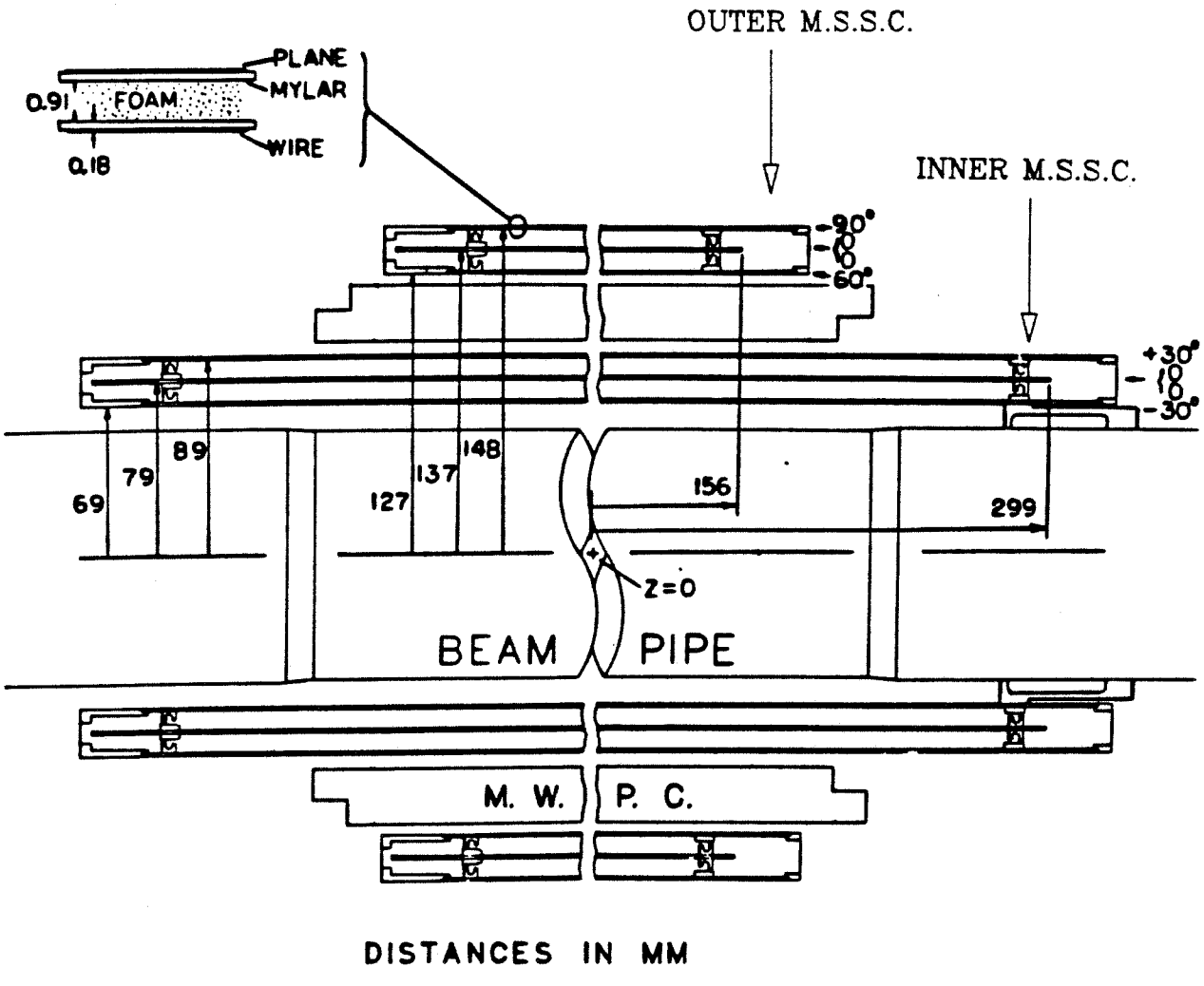

Figure 2.3: The central tracking chamber system for the Crystal Ball, consisting of an inner magnetostrictive spark chamber (MSSC), a multiwire proportional chamber, and an outer MSSC.

2.2d Luminosity Monitor

Four small shower counters, placed at 4° relative to the beam axis, were used to determine the luminosity based on the counting rate for small angle Bhabha events. For this analysis, luminosity information was needed only for estimating the size of QED backgrounds.

2.2e Outer Hadron-Muon Separator

The Outer Hadron-Muon Separator (OHMS), covering 15% of 4π sr, consists of thick iron absorber interspersed with proportional tubes and scintillation counters. OHMS information was not used in this analysis.

2.3 Experimental Triggers

The experiment was triggered when certain calorimetric and/or charged particle tracking requirements were satisfied. The goal was to trigger on all ψ decays, while minimizing the contamination of beam-gas and cosmic ray events. It was also desired to trigger on large angle Bhabha events in which the e^+e^- scattered into the main ball, as a check of the luminosity measurement.

The simplest trigger, called the Total Energy Trigger, simply required the sum of energy deposited in all crystals in the main ball to exceed some threshold. For ψ running, this threshold was set at 1.1 GeV, although some early data were taken with a 1.7 Gev threshold. For periods of high beam-gas backgrounds, the tunnel modules were removed from the total energy sum, reducing the active solid angle of this trigger to 85%. Another trigger using only information from the NaI(Tl) crystals was referred to as the Quark Trigger. Designed to be sensitive to the production of a pair of fractionally charged particles, this trigger required an energy deposition of at least 40 MeV in each of two back-to-

back minor triangles, as well as a total energy deposition of 140 MeV in the entire ball, excluding tunnels and endcaps. The Multiplicity Trigger used a combination of chamber and crystal information to identify events with two or more charged tracks. First a count was made of the number N_{MT} of major triangles with deposited energy greater than 110 MeV (well below the expectation for a minimum ionizing particle). Next, the MWPC hits were scanned for the number of coincidences N_{MWPC} between the two wire planes. The actual Multiplicity Trigger was then defined to be the logical OR of the following requirements on N_{MT} and N_{MWPC}:

1.) $N_{MWPC} > 0$ AND $N_{MT} = 2$

2.) $N_{MWPC} > 0$ AND $N_{MT} = 3$

3.) $N_{MT} \geq 4$.

The Total Energy, Quark, and Multiplicity Triggers were integrated into a single TTL hardware unit, called the Tower Trigger. To allow flexibility for future triggers and to provide redundancy for existing triggers, a second trigger system based on NIM modules was also operated. This trigger, known as Fast Trigger, required at least 650 MeV to be deposited in the main ball, with at least 160 MeV each in the top and bottom hemispheres. In addition, these energy signals were required to be within 8 ns of coincidence with the beam crossing. The final experimental trigger was a logical OR of the three Tower Triggers and the Fast Trigger. Monte Carlo studies indicate that the trigger efficiency for inclusive hadronic decays of the ψ was approximately 99% [2.3]. Of course, certain exclusive decay modes will have significantly lower trigger efficiencies, particularly those with very low multiplicities. For this reason, the trigger requirements were incorporated in the Monte Carlo detector simulation, allowing the trigger efficiency to be properly treated for each final state investigated. For

example, the trigger efficiency for $\psi \to \rho\pi$ was found to be only 92%, due primarily to the low multiplicity.

2.4 Data Analysis

When a trigger was generated, the crystal energies were digitized and written to tape. MSSC and MWPC chamber hits were also written out. These data were later passed through a first-stage analysis, in which particle tracks were reconstructed from the raw data. To better understand some of the possible background problems to be faced in the subsequent physics analyses, it will be illustrative to briefly review the individual steps of this first-stage analysis.

The first step in the analysis is the conversion of the crystal ADC pulse heights into energies, using the pedestals and gains obtained via the Cs^{137}, Van de Graaff, and Bhabha calibrations. Figure 2.4 shows an event display for a typical hadronic ψ decay. In this projection, the 672 NaI(Tl) crystals of the main ball have been "unwrapped" and projected onto a plane, much like a Mercator projection of the Earth. The numbers in each crystal represent the energy in MeV deposited in that crystal. The next step in the analysis is the identification of groups of neighboring crystals in which energy has been deposited. These groups of neighboring crystals are referred to as connected regions, and are formally defined as a set of crystals, each with energy greater than 10 MeV, such that each crystal in the group shares a vertex or an edge with at least one other crystal in the group. Connected regions have been indicated by bold lines in Figure 2.4.

Once these connected regions have been defined, each connected region is in turn examined to determine how many particles created the observed pattern of energy within that connected region. Given the limited size of the connected

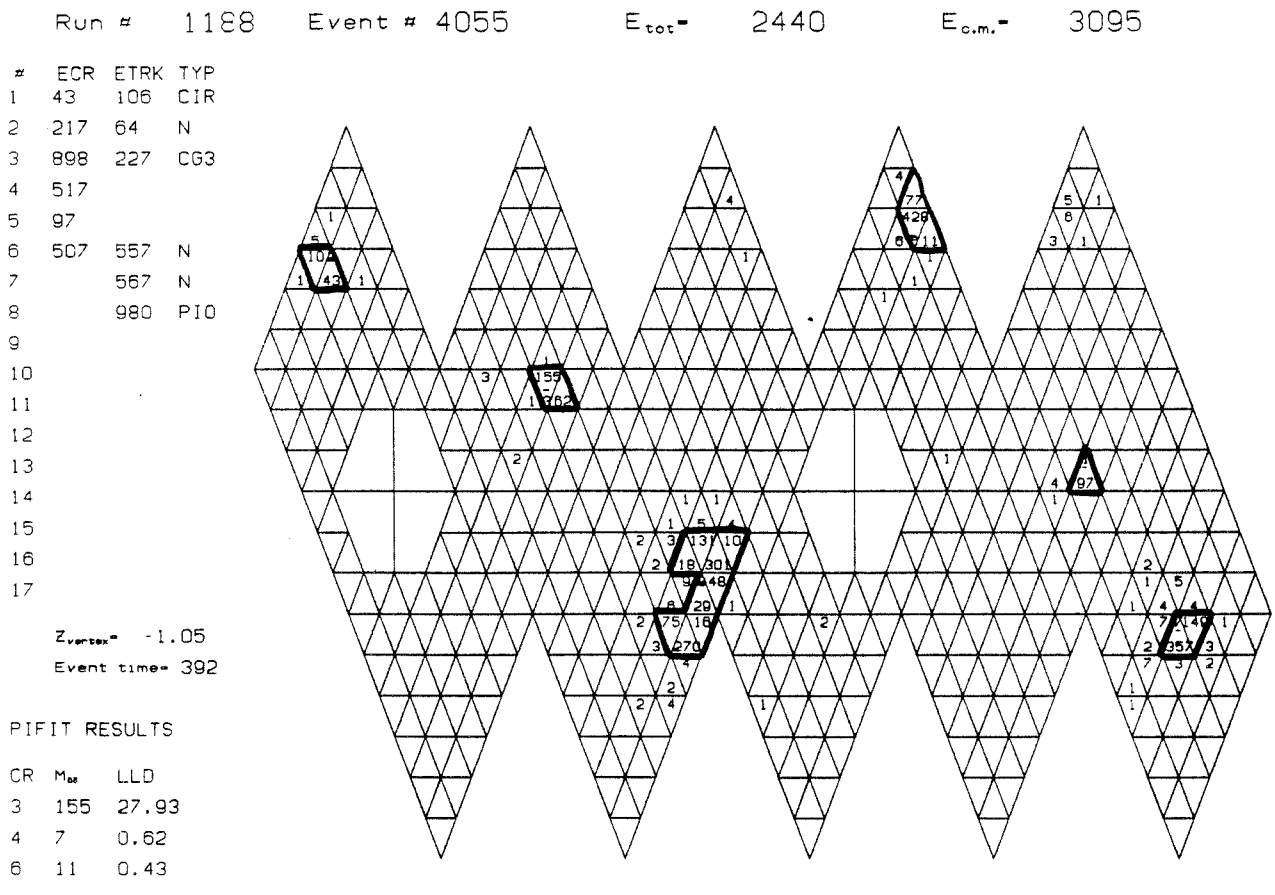

Figure 2.4 An event display for a typical hadronic ψ decay. Connected regions are outlined in bold lines.

regions and the expected ψ final state multiplicities, most connected regions will be due to only one particle track. However, the fine segmentation of the ball allows us to try to identify those connected regions which contain several tracks. This is done by searching for "bumps" in the pattern of energy distribution within a connected region. Care is taken to distinguish real bumps due to separate particles from bumps due to fluctuations in the shower of a single particle. The first bump in a given connected region is assigned to the highest energy crystal within that region. Then, using an algorithm developed from a study of $\psi' \to \pi\pi\psi$ decays, it is determined whether each of the other crystal energies is consistent with being part of the shower from the first bump. This determination is based on the energy in the bump module, the energy in the crystal under consideration, and the distance between the two crystals. If any crystals are found in the connected region whose energies are inconsistent with being a part of the shower from the previous bump, then a new bump is defined. This process is iterated until all crystal energies within the connected region are accounted for. Each bump found is treated as representing a separate particle, with an entry made in a "particle track bank" for that bump.

At this point in the analysis, the tracking chamber information is examined. The analysis of the chamber data is conducted in two stages. First the MSSC's are examined for charged tracks, independent of the crystal information. To reconstruct a track, both the inner and outer MSSC are required to have at least one straight-plane and one crossed plane spark hit. In addition, these hits are required to point back close to the e^+e^- interaction point. Tracks found in this manner are referred to as "IR tracks". Since both inner and outer MSSC hits are required for IR tracks, this method is only efficient over the 71% of 4π sr covered by the outer MSSC. The trajectories of all the IR tracks are used to determine

the z-position (position along the e^+e^- beam direction) of the interaction vertex. The x and y positions of the interaction vertex are assumed to be 0.

After all IR tracks have been found, the second stage of charged particle analysis is performed. In this stage, an attempt is made to correlate the remaining MSSC hits and the MWPC hits with the NaI(Tl) tracks identified in the "bump" analysis. First each IR track found above is matched with a bump in the NaI(Tl) crystals. If no bump is found for a given IR track, a new entry is made in the particle track bank. For each of the NaI(Tl) tracks which is uncorrelated with an IR track, all three chambers are examined for hits along a line joining the interaction vertex with the shower center in the NaI(Tl) crystals. If at least one straight plane and one crossed plane hit are found, the track is called charged. This second stage of charged particle analysis is referred to as "tagging," since the chambers are only used to determine whether the previously identified NaI(Tl) tracks are charged.

The final stage of the standard production analysis consists of assigning energies to each of the particle tracks. Two different algorithms have been developed for this purpose. The ESORT algorithm uses a parametrization of the expected electromagnetic shower profile, obtained from Monte Carlo studies, to assign crystal energies to particle tracks. For nearby tracks, ESORT will attempt to unfold overlapping showers, determining the optimal sharing of each crystal's energy among the tracks to best fit the observed shower profiles. The shower profiles are also used to adjust the direction of neutral tracks. A second energy algorithm, called the E13 energy, is based solely on the energy deposited in the bump module and its immediate neighbors. Most crystals in the main ball are surrounded by twelve neighboring crystals with which they share an edge or a vertex. (The crystals which lie on the corners of major triangles have only 11

neighbors.) For electromagnetic showers, these clusters of 12 or 13 crystals contain on average 97.8% of the total energy deposited by a photon or electron entering the central crystal. A correction factor is applied to correct for the extra energy which leaks outside of this group of crystals. In addition, a small correction is made based on the exact position of the initial particle in the central crystal. Unlike the ESORT method, the E13 approach makes no attempt to untangle overlapping showers from nearby tracks. However, for well-separated showers, the E13 method actually gives better results for electromagnetically showering particles, yielding the previously cited energy resolution of $\sigma(E)/E = 2.6\%/E(GeV)^{1/4}$. For the analysis in this paper, E13 energies were used for all neutral tracks.

2.5 Hadron Selection

Many of the events recorded while running at the ψ are actually due not to ψ decays but to other processes such as QED events, cosmic rays, and beam-gas interactions. After the first-stage production analysis, these background processes were removed to obtain a cleaner sample of hadronic ψ decays. We will discuss briefly the hadron selection here; a full description is available in [2.4]. The selection criteria were obtained by studying several classes of events. Beam gas events were studied by taking data with separated beams; events out of time with the e^+e^- beam crossing were used to understand cosmic ray events; Monte Carlo datasets were generated to study the various QED background processes.

The requirements of the hadron selection are summarized here:

a.) At least three tracks (charged or neutral) are required to be observed in the detector. This primarily eliminates QED, cosmic ray, and beam-gas events, and is nearly 100% efficient for hadronic ψ decays.

b.) The sum of the energies depositied in all crystals must be between 656 and 3445 MeV. Once again, nearly all ψ decays should satisfy this requirement with very high efficiency.

c.) Remaining QED events are removed based on a series of cuts designed to find and reject events in which one or two high energy tracks constitute most of the total observed energy. To improve the efficiency for all-neutral ψ decays, such as $\psi \to \gamma\eta$, $\eta \to \gamma\gamma$, the additional requirement is made that at least one of these high energy tracks be charged.

d.) Beam gas and cosmic ray events are removed by rejecting events which display a very asymmetric distribution of crystal energies with respect to the interaction point. This asymmetry cut proved to be the most inefficient part of the hadron selection for low multiplicity final states. For example, a Monte Carlo study indicated that 10% of all $\psi \to \rho\pi$ decays were rejected by the asymmetry cut. More complicated final states were typically much more efficient. For instance, the inefficiency of the asymmetry cut was found to be 1.3% for the $\gamma K^+ K^- \pi^0 \pi^0$ final state and 2.1% for the decay sequence $\psi \to \gamma\eta'$, $\eta' \to \gamma\rho$, $\rho \to \pi^+\pi^-$.

Table 2.2 reviews the results of the hadron selection for the ψ dataset.

Table 2.2 $\psi(3095)$ Dataset	
Experimental Triggers:	5.7×10^6
Integrated Luminosity:	765 nb^{-1}
# of Events in Final Hadron-Selected Sample:	1.78×10^6
# of Background Events in Sample:	24.5×10^3
Overall Trigger and Hadron-Selection Efficiency:	94 ± 5 %
# of $\psi(3095)$ Produced:	2.17×10^6 ($\pm 5\%$)

2.6 PIFIT

In both the analysis of inclusive photon spectra and the investigation of exclusive final states, the ability to detect and reconstruct π^0's is of great importance. For inclusive analysis, π^0 decay photons provide the major background to the search for monochromatic lines; identifying and removing these π^0 decay photons allow this background to be reduced. For exclusive analysis, π^0 reconstruction is essential in observing the many decay modes involving final state pions. With excellent energy and angular resolution for photons, and nearly complete solid angle coverage, the Crystal Ball is unique in its ability to reconstruct π^0's. For π^0's with energy less than 750 MeV, the decay photons are usually well separated, allowing very good efficiency in their detection, good energy and angular resolution for both photons, and thus good mass resolution for the photon pair. However for π^0's of energy near 1 GeV and above, the decay photons will often be emitted with a small opening angle, resulting in overlapping showers in the NaI(Tl) crystals. These cases are referred to as "merged" π^0's.

It is straightforward to work out the expected distribution of $\gamma\gamma$ opening angles as a function of the π^0 energy. Let θ be the opening angle between the two photons in the lab, and let β and γ be $p_\pi^{lab} / E_\pi^{lab}$ and E_π^{lab} / m_π respectively. Using the fact that the π^0 has a flat angular decay distribution in its center-of-

mass, we obtain the lab opening angle distribution:

$$P(\theta) = \begin{cases} 0 & \text{for } \theta < \text{acos}(1-\frac{2}{\gamma^2}) \\ \frac{\sin\theta}{\beta\gamma^2(1-\cos\theta)^2}\left[1-\frac{2}{\gamma^2(1-\cos\theta)}\right]^{-1/2} & \text{for } \theta > \text{acos}(1-\frac{2}{\gamma^2}). \end{cases}$$

Two observations may be made concerning this distribution. First, the minimum opening angle, $\theta_{min} = \text{acos}(1-\frac{2}{\gamma^2})$, varies roughly as $1/E_\pi^{lab}$ for large pion energy, as can be seen by expanding θ_{min} for $\gamma \gg 1$. Second, the distribution peaks (and actually goes to infinity) at this minimum opening angle, as the factor $[1-\frac{2}{\gamma^2(1-\cos\theta)}]$ equals zero for $\theta = \theta_{min}$. Both of these features are evident in Figure 2.5, which shows a scatterplot of $\gamma\gamma$ opening angle versus π^0 momentum for a sample of Monte Carlo π^0's.

As the π^0 energy approaches 1.5 GeV, the opening angle becomes so small that the standard bump analysis will almost always fail to recognize the overlapping showers as separate tracks. When this occurs, it is of course impossible to reconstruct the π^0 from the standard production track information, and the merged π^0 track becomes a background for high energy photons. Even when the overlapping showers are resolved as separate tracks by the production analysis, the small opening angle results in a poor mass resolution. In addition, although the sum of the two photon energies is well measured, the individual photon energies are not as well determined, due to the overlap.

The PIFIT algorithm was developed with the goal of identifying merged π^0's through a more thorough examination of the pattern of energy distribution among crystals. A complete discussion of the development and details of PIFIT can be found in [2.5]; here we will just review the strategy and discuss the accuracy and efficiency of the algorithm. The heart of the PIFIT approach is the

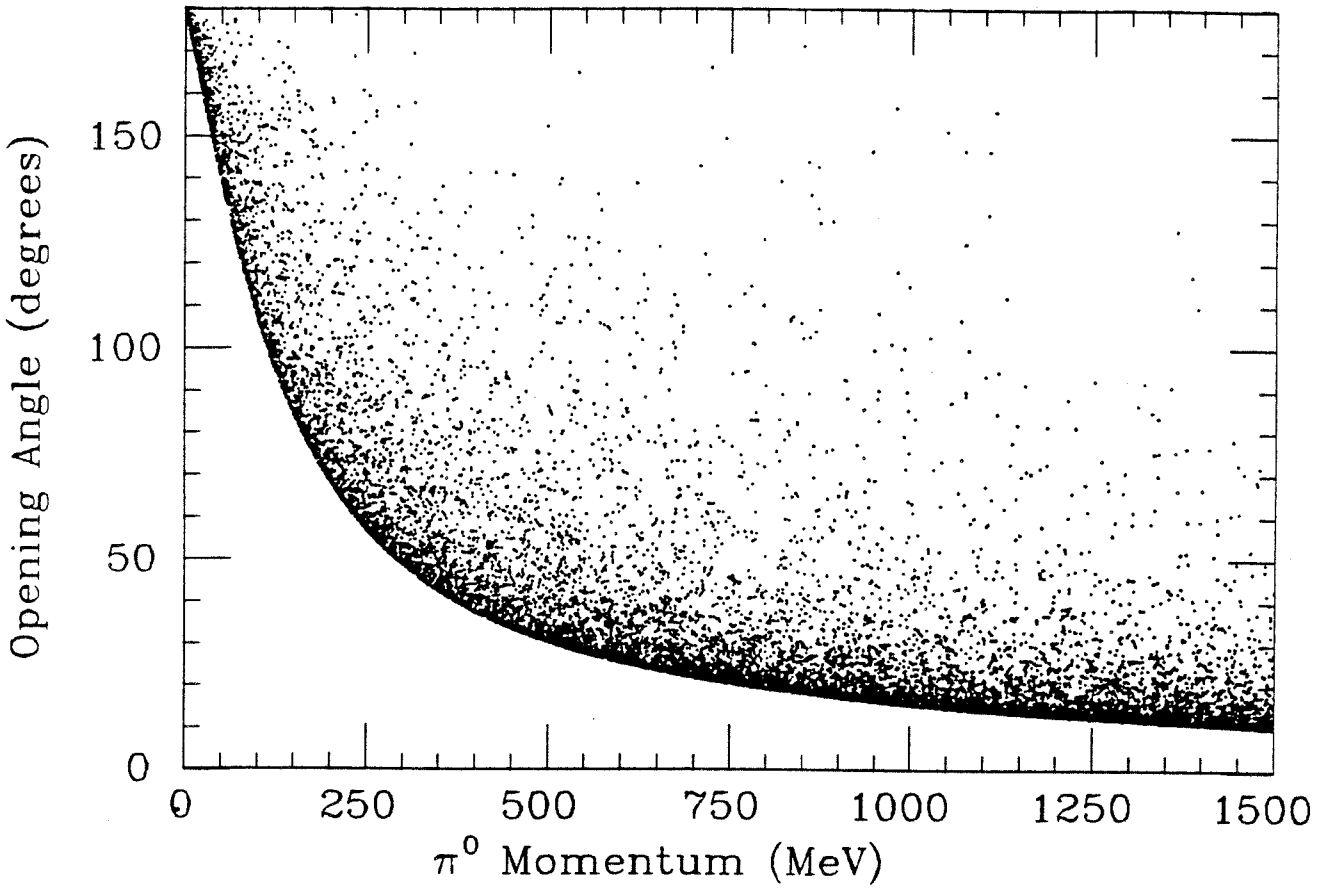

Figure 2.5: $\gamma\gamma$ opening angle vs. π^0 momentum for Monte Carlo π^0 decays.

determination of shower likelihood functions. Consider first a single photon shower. We will attempt to determine the photon direction which best fits the observed pattern of energy deposition. The photon energy will not be fit; rather, we will use the E13 energy. Letting e_i represent the observed crystal energies, E_γ represent the incident photon energy, and $\hat{p}_\gamma$ represent the unit vector in the actual photon direction; then in principle there exists a likelihood function $L_1(e_i,\hat{p}_\gamma,E_\gamma)$ which fully describes the probability that a photon of energy E_γ and direction $\hat{p}_\gamma$ will display the pattern of energy distribution e_i. Determining this likelihood function would involve the study of a thirteen-dimensional space of observables (the energy in a central crystal and its 12 neighbors). To make the problem more tractable, the assumption has been made that we can factorize this likelihood function into a product of individual likelihood functions for each crystal:

$$L_1(e_i,\hat{p}_\gamma;E_\gamma) = \prod_i l_i(e_i,\hat{p}_\gamma;E_\gamma).$$

Here each l_i describes the likelihood that a photon with momentum $\vec{p}_\gamma$ will deposit energy e_i in crystal i. The obvious limitation of this factorization is that correlations among crystals are ignored.

The likelihood functions l_i were determined by studying Monte Carlo photon showers for various incident photon energies and positions within the central crystal. For a given photon energy, the likelihood function for the central crystal was fit to a function of two variables: the distance of the photon from the crystal center and the distance of the photon from the nearest crystal edge. The likelihood functions for the 11 or 12 neighboring crystals were fit to a function of the angle between the photon momentum vector and the center of the crystal in question. The likelihood functions were determined for several

different incident photon energies; the coefficients of these fits were linearly interpolated to determine the likelihood function for arbitrary photon energy.

Equipped with these single photon likelihood functions, we can extend the technique to treat two overlapping showers. Given two nearby photons with momenta $\vec{p}_{\gamma_1}$ and $\vec{p}_{\gamma_2}$, we can form a likelihood function describing the probability of observing energies e_i in the set of crystals $\{i\}$. As for the single photon case, we will not attempt to fit the overall energy $E_{\gamma\gamma}$ of the two showers; however, we will fit the splitting of the total energy between the two photons. With photon directions $\hat{p}_{\gamma_1}$ and $\hat{p}_{\gamma_2}$, and letting x represent the fraction of $E_{\gamma\gamma}$ attributed to γ_1, the likelihood function is simply a convolution of two single photon likelihoods:

$$L_2(e_i, x, \hat{p}_{\gamma_1}, \hat{p}_{\gamma_2}; E_{\gamma\gamma}) = \int\int \cdots \int de'_i L_1(e'_i, \hat{p}_{\gamma_1}, xE_{\gamma\gamma}) L_1(e_i - e'_i, \hat{p}_{\gamma_2}, E_{\gamma\gamma}).$$

This in turn factorizes into a product of convolutions over the single-crystal likelihoods l_i:

$$\prod_i \int de'_i l_i(e'_i, \hat{p}_{\gamma_1}, xE_{\gamma\gamma}) l_i(e_i - e'_i, \hat{p}_{\gamma_2}, (1-x)E_{\gamma\gamma}).$$

The form of the likelihood functions l_i were specifically chosen such that these convolutions could be performed analytically.

The actual process of "PIFIT-ing" a connected region begins by selecting suitable starting values for the parameters $\hat{p}_{\gamma_1}$, $\hat{p}_{\gamma_2}$, and x, based on a preliminary examination of the individual crystal energies within the connected region. The set of crystals $\{i\}$ which will be used in the likelihood formula is defined as the two crystals pointed to by the photon directions $\hat{p}_{\gamma_1}$ and $\hat{p}_{\gamma_2}$, along with all other crystals in the region which share a crystal edge or vertex with either of these first two crystals. Then the likelihood function is maximized with respect

to the parameters $\hat{p}_{\gamma_1}$, $\hat{p}_{\gamma_2}$, and x, yielding as a result the photon directions and energies which best account for the observed energy pattern. This of course also determines a mass for the $\gamma\gamma$ pair, which can be used to identify merged π^0 showers. Figure 2.6 shows the PIFIT $\gamma\gamma$ mass distributions for Monte Carlo photons and π^0's at various energies. Good separation is achieved even beyond the kinematic limit of γ/π^0 momentum allowed in ψ decays. A note of explanation concerning the $\gamma\gamma$ mass distributions for single photon showers: the distribution peaks at a non-zero value due to shower fluctuations and phase space. Shower fluctuations for single photon showers cause PIFIT, in its effort to maximize the fit likelihood, to place the second photon in a slightly different direction than the first, resulting in a non-zero $\gamma\gamma$ mass. In addition, the available phase space for zero $\gamma\gamma$ mass (both photons exactly in the same direction) is vanishingly small.

In addition to the two-photon fit described above, PIFIT performs what is effectively a one-photon fit to determine the relative likelihood that a shower was formed by one or by two photons. This is done by fixing x near 1 so that all of the shower's energy is attributed to the first photon, and by fixing the direction of the second photon in the center of the highest energy crystal within the connected region. L_2 is then maximized subject only to variation of $\hat{p}_{\gamma_1}$. This in effect removes γ_2 from the fit and gives the likelihood that the shower was formed by a single photon. Although the overall normalization of the PIFIT likelihood function is not well understood, taking the quotient of the likelihoods for one- and two-photon hypotheses removes much of this normalization uncertainty and provides a meaningful relative likelihood for the two hypotheses. In practice, we work with the logarithm of the L_2, and so we define a log-likelihood difference (LLD) parameter:

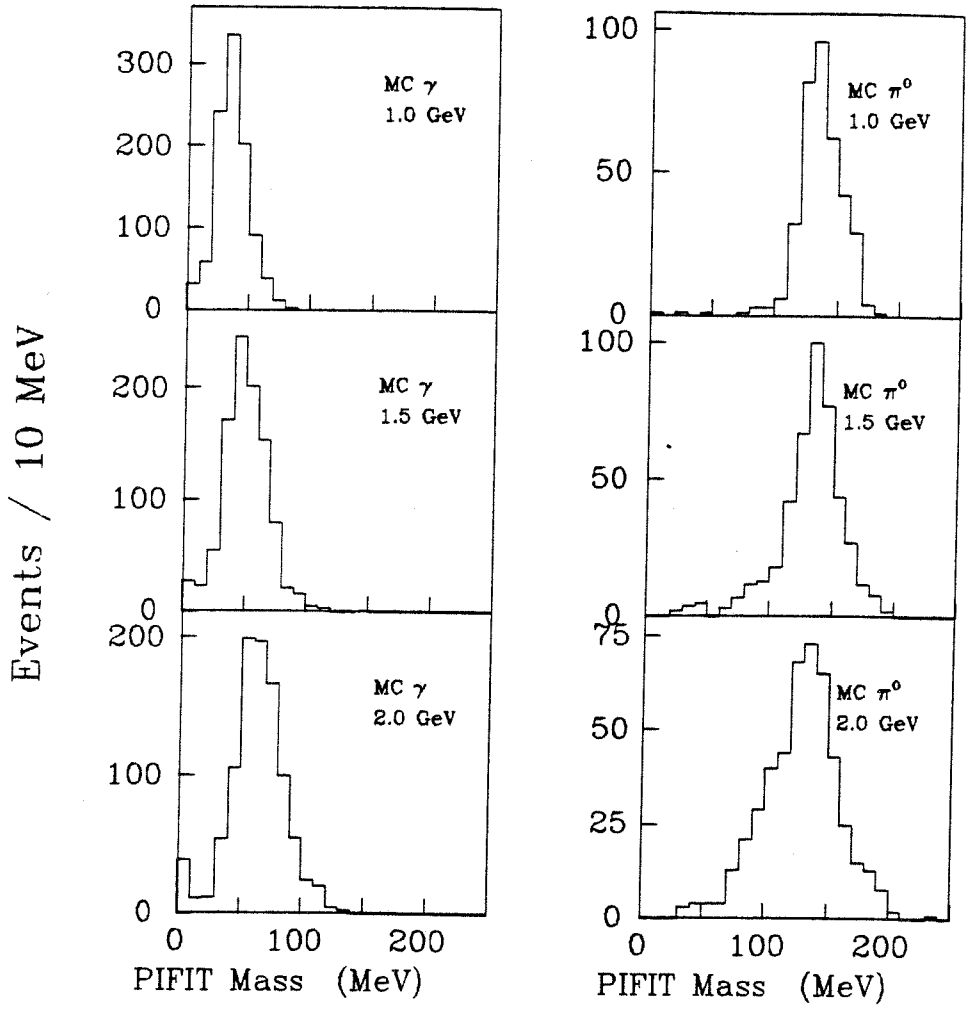

Figure 2.6: PIFIT $\gamma\gamma$ mass distribution for Monte Carlo γ's and π^0's at various energies.

$$\text{LLD} = \log L_2(e_i, x, \hat{p}_{\gamma_1}, \hat{p}_{\gamma_2}; E_{\gamma\gamma}) \; - \; \log L_2(e_i, x \equiv 1, \hat{p}_{\gamma_1}, \hat{p}_{\gamma_2}\, fixed; E_{\gamma\gamma}).$$

While there are correlations between LLD and the PIFIT $\gamma\gamma$ mass, LLD does provide a somewhat independent means of determining if a shower was created by one or two photons. This feature will be instrumental in the search for the decay $\psi \rightarrow \gamma\pi^0$.

The PIFIT algorithm was applied to all of the hadron selected ψ data in an effort to recover merged π^0's and improve the energy and angular resolution for overlapping photons. Only connected regions with over 500 MeV of energy and containing one or two neutral tracks were processed. Since charged tracks generally were due to hadrons, and since the PIFIT likelihood function was developed only for electromagnetic showers, PIFIT was not applied if the connected region contained any charged tracks. Based on the $\gamma\gamma$ mass obtained by PIFIT, the connected region is classified as either a single photon, a π^0, or a $\gamma\gamma$ overlap. For $m_{\gamma\gamma}$<80 MeV, the connected region is considered a single photon, and the original particle tracks are left unchanged. For 80<$m_{\gamma\gamma}$<180 MeV, the connected region is classified as a π^0, the old neutral tracks associated with the connected region are removed from the track bank, and a new π^0 track is entered. Finally, for $m_{\gamma\gamma}$>180 MeV, the connected region is interpreted as a random overlap of two photons, and the old track or tracks are replaced by the two PIFIT photons.

Due to the complexity of the PIFIT likelihood convolution functions, PIFIT is a very CPU-intensive task. A typical connected region required approximately 2.5 seconds of VAX/VMS CPU time for PIFIT processing, while a full month of dedicated VAX CPU time was required to process all of the ψ hadron selected data. Roughly half of all hadronic ψ events contained a connected region which satisfied the PIFIT selection criteria. Of these regions, approximately 55% were

identified as single photons by PIFIT, 35% as merged π^0's, and 10% as $\gamma\gamma$ overlaps.

2.7 Selection of Exclusive Final States

The first step in investigating a given exclusive decay mode is to select candidate events from the entire ψ dataset which satisfy basic multiplicity requirements. While the specific criteria vary according the final state in question, and will be outlined in detail for each final state investigated, some general comments may be made here. First, we note just how important good solid angle coverage is for efficiently detecting complex final states. The probability that N particles will all reside in a given region of solid angle Ω is just $(\Omega/4\pi)^N$, assuming flat angular distributions. As N becomes large, this probability becomes a steep function of Ω. For example, in Chapter V we examine the final state $\gamma\rho^+\rho^-$, which yields a final state of 2 charged particles and 5 photons. By increasing our solid angle coverage from 80% to 90% of 4π sr, we increase the probability of observing all 7 particles from 21% up to 48%, over a factor of two. Thus we will typically make fairly loose solid angle requirements for individual tracks when searching for high multiplicity final states.

In principle, selecting events of the correct multiplicity is simple. For instance, if we were searching for the process $\psi\rightarrow\gamma\pi^+\pi^-$, we would select events with two charged tracks and one neutral track, demanding that the neutral track not be a merged π^0. A number of effects complicate this task, however. First, consider the various ways in which the event multiplicity can be underestimated. Final state particles which travel down the beam pipe will not be observed. Neutral hadrons such as neutrons or K_L's can pass through the crystals with no energy deposition, and thus escape detection. Tracks very close to one another may not be resolved as separate tracks. Very low energy photons

will not detected, as only crystals with at least 10 MeV of deposited energy are used to define connected regions. These effects all allow decays with higher true multiplicities to contaminate the sample of candidate events for the multiplicity of interest.

On the other hand, we can also overestimate the multiplicity of an event. Primarily this occurs when a particle interacts in the crystals, and a portion of the subsequent shower becomes spatially separated from the main shower. When this separation becomes sufficiently large, the standard analysis program will interpret this shower fragment as a separate particle track. These shower fragments, or "splitoffs," provide a serious background source of low energy neutral tracks. Because the mean path length in NaI(Tl) is much larger for a hadronic shower than for an electromagnetic shower, hadronic showers are much more likely to generate a splitoff than are photon or electron showers.

Splitoffs are typically of low energy and close proximity to their parent shower. In addition, hadronic splitoffs have patterns of energy deposition which are inconsistent with electromagnetic showers. Shower patterns are conveniently examined by forming ratios of the energy deposited in various portions of the shower. The energy deposited in the central crystal of a shower is designated E1. Adding the energy in the three crystals which share a face with the central crystal, we obtain E4. Finally, adding the energy in the crystals which share an edge with the central crystal, we obtain E13. Figure 2.7 shows the crystals used to define E1, E4, and E13 for a typical electromagnetic shower. The ratios E1/E4 and E4/E13 can be used to distinguish electromagnetic showers from minimum ionizing or interacting hadronic showers [2.3]. The SPLIT algorithm [2.6] was developed to identify splitoffs by examining the energy, shower pattern, and proximity to other showers of each neutral track in an event. For

several of the final states examined here, SPLIT was used to reduce the contamination of the candidate event sample by events with lower true multiplicities plus splitoffs.

2.8 Kinematic Fitting

The intrinsic resolution of the detector can be improved by adding the constraints of energy and momentum conservation, which state that the sum of the four vectors of the final state particles must add up to give $E=m_\psi$ and $\vec{p}=0$. For photons, electrons, and merged π^0's, both energy and direction are measured. However, only directions are measured for charged hadrons. For final states with zero or two charged particles we have more constraints than unknowns, and may fit the event to a given hypothesis subject to energy and momentum constraints. Additional constraints may be obtained by placing other kinematic requirements on the event, such as demanding that a pair of photons come from the decay of a π^0 or η. The kinematic fitting package SQUAW [2.7] was used to fit events to particular kinematic hypotheses. The resolutions used for various types of tracks are shown in Table 2.3.

Table 2.3 Resolutions Used in SQUAW Fits	
σ_E/E at $E=1$ GeV for e.m. showering tracks:	0.025
Angular resolution for e.m. showering tracks:	0.04
Angular resolution for other tracks with direction cosines based on NaI(Tl) information:	0.06
φ resolution for IR tracks:	0.02
Slope resolution for IR tracks:	0.03

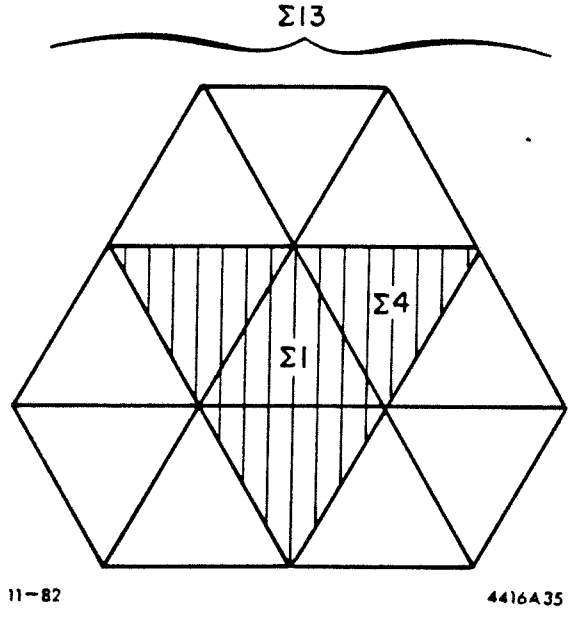

Figure 2.7: Crystals used to define E1/E4 and E4/E13 shower pattern ratios.

As the Crystal Ball has no dE/dx or time-of-flight measurement capabilities, kinematic fitting provides the only means of distinguishing charged pions and kaons. For certain kinematic regimes, good π/K separation is achieved, with an acceptable fit obtained for only one interpretation of the charged tracks. For other classes of events, the separation is poor, with acceptable fits obtained with either a π or K interpretation of a given charged track. In general, the best separation is obtained when the charged particles are moving slowly. In this case, changing the particle hypothesis from π to K results in a larger change in that particle's energy, for a given momentum assignment. When a charged track has momentum much larger than the K mass, however, changing the interpretation from π to K has a negligible effect on the particle's energy, and thus a negligible effect on the fit quality.

Chapter III References

[2.1] M. Oreglia *et al.*, Phys. Rev. D25, 2259 (1982), and references therein.

[2.2] G. Godfrey, in Crystal Ball Summer School, 1980 (unpublished).

[2.3] J. E. Gaiser, Ph.D. thesis, Stanford University, 1983 (unpublished).

[2.4] F. C. Porter, in Proceedings of Summer Institute on Particle Physics, SLAC, July 27 - August 7, 1981, Ed., Anne Mosher, SLAC Report No. 245, pp. 355-380; also SLAC-PUB-2796.

[2.5] R. A. Partridge, Ph.D. thesis, Caltech, 1984 (unpublished).

[2.6] K. Koenigsmann and F. Bulos, Crystal Ball Note No. 154, 1980 (unpublished).

[2.7] O. Dahl, T. Day, F. Solmitz, and N. Gould, Group A Programming Note No. P-126, Berkeley (LBL), July 1968; J. Berge, F. Solmitz, and H. Taft, Rev. Sci. Inst. 32, 538 (1961).; F. C. Porter, Crystal Ball Note No. 20, April 1982 (unpublished).

Chapter III

Observation of the Decay $\psi \to \gamma\pi^0$

3.1 Introduction and History

In 1980 the Crystal Ball reported results of a study of the process $\psi \to 3\gamma$ [3.1], showing evidence for the radiative decays $\psi \to \gamma\eta$ and $\psi \to \gamma\eta'$. Radiative decays to the remaining pseudoscalar, $\psi \to \gamma\pi^0$, were not observed at that time, but a significant limit could not be set because certain cuts used in the analysis to reject QED events would also have removed most $\gamma\pi^0$ events. In this chapter, a new search for the decay $\gamma\pi^0$ is described. Good efficiency for π^0's and good QED rejection are achieved through the use of the pattern recognition algorithm PIFIT. A signal is observed, with a branching fraction $BF(\psi \to \gamma\pi^0) = (3.6 \pm 1.1 \pm 0.7) \times 10^{-5}$, where the first error is statistical and the second is systematic. This agrees with a previous DASP measurement $BF(\psi \to \gamma\pi^0) = (7.3 \pm 4.7) \times 10^{-5}$ [3.2].

3.2 Flavor SU(3) and Vector Dominance

The relative rates for $\psi \to \gamma\eta$, $\gamma\eta'$, and $\gamma\pi^0$ probe the mechanism of radiative ψ decay into ordinary hadrons [3.3]. In leading order QCD one can imagine the radiated photon as coupling to either the charmed quark line or the light quark line, as depicted in Figure 3.1. Flavor SU(3) can be used to relate the relative rates into $\gamma\eta$, $\gamma\eta'$, and $\gamma\pi^0$ for each of these diagrams. The physical η and η' are linear combinations of the flavor singlet η_1 and octet η_8:

$$\eta = \eta_8 \cos\theta + \eta_1 \sin\theta$$

$$\eta' = -\eta_8 \sin\theta + \eta_1 \cos\theta$$

where the mixing angle θ is determined experimentally to be $-11°$. In Figure 3.1a, only η_1 contributes, while in Figure 3.1b, only η_8 contributes. Thus for Figure 3.1a the ratios are:

$$\Gamma_{\gamma\pi^0} : \Gamma_{\gamma\eta} : \Gamma_{\gamma\eta'} = 0 : \sin^2\theta : \cos^2\theta = 0 : .04 : .96$$

and for Figure 3.1b:

$$\Gamma_{\gamma\pi^0} : \Gamma_{\gamma\eta} : \Gamma_{\gamma\eta'} = 3 : \cos^2\theta : \sin^2\theta = 3 : .96 : .04 .$$

The fact that the $\gamma\eta$ and $\gamma\eta'$ rates are observed to be much higher than the $\gamma\pi^0$ rate indicates that the diagram with the radiated photon coupling to the charmed quark has a higher rate, as expected in perturbative QCD, since only two gluons are needed in this case. Also, one observes that any $\gamma\pi^0$ decays can occur only through the three gluon diagram, suppressed by α_S^2 with respect to the two gluon graph.

The absolute rate $\Gamma_{\gamma\pi^0}$ for Figure 3.1b can be calculated within the framework of vector meson dominance (VMD) [3.4]. The basic idea of VMD is that photons couple to hadrons primarily through vector meson resonances (ρ,ω,φ). Formally, one replaces a sum over all states by a sum over only the vector mesons:

$$\langle Hadrons | J_\mu | 0 \rangle = \sum_{V=\rho,\omega,\varphi} \langle Hadrons | V \rangle \frac{\sqrt{4\pi}\, e}{q^2 - M_V^2 + i\Gamma_V M_V} \langle V | J_\mu | 0 \rangle . \quad (3.1)$$

Coupling to a real photon corresponds to taking $q^2=0$ in the vector meson propagator. One can define a vector meson coupling constant g_V:

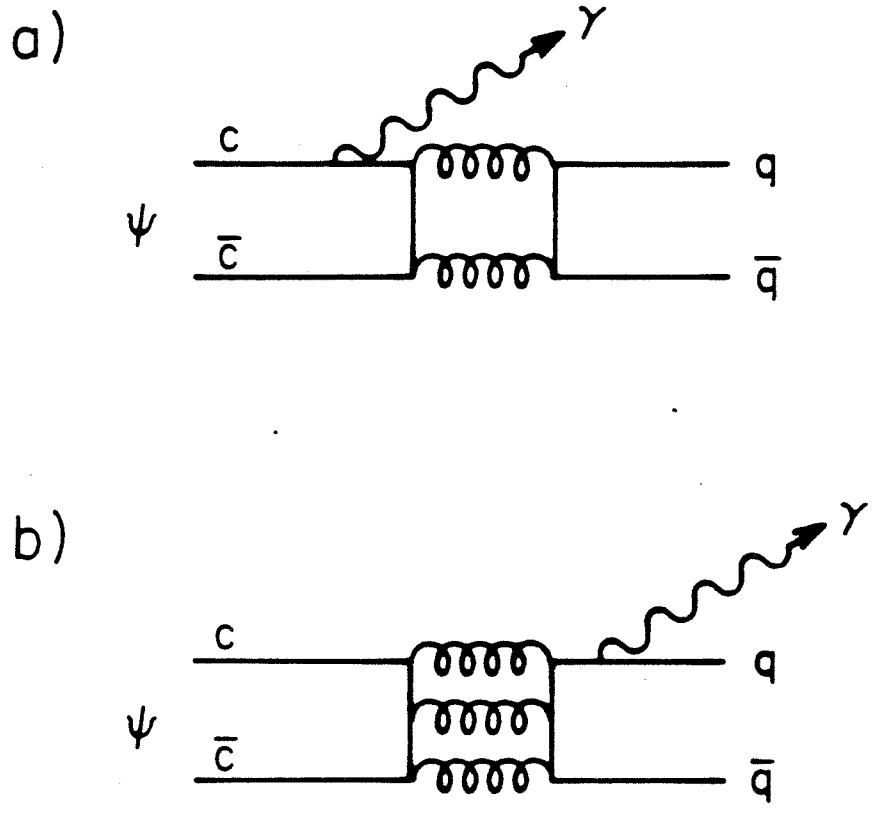

Figure 3.1: Lowest order diagrams for radiative decays of ψ into light quarks. 3.1a has the radiated photon coupling to the charmed quark, while 3.1b has the photon coupling to the light quark. Due to charge conjugation symmetry, the ψ cannot couple directly to two gluons. Thus diagram 3.1b requires three gluons while 3.1a requires only two.

$$\frac{M_V^2}{g_V} = \langle V|J_\mu|0\rangle$$

whose value can be measured experimentally in the leptonic decay $V \to e^+e^-$:

$$\Gamma(V \to e^+e^-) = \frac{\alpha^2}{3}\frac{4\pi}{g_V^2}M_V.$$

For the ρ, the result is $\frac{g_\rho^2}{4\pi} \approx 2$. (Implicit in this model is the assumption that this coupling does not vary significantly as we move q^2 from its on-shell value of M_V^2, where we measure g_V, all the way down to $q^2=0$.) Because the π has isospin I=1, only the isovector component of the photon contributes to $\psi \to \gamma\pi^0$, and hence only the ρ contributes in the sum over V in Eq. 3.1. Thus, VMD predicts

$$\Gamma(\psi \to \gamma\pi^0) = \frac{4\pi\alpha}{g_\rho^2}\Gamma(\psi \to \rho^0\pi^0) \approx 1\ eV$$

or, since $\Gamma_{tot}(\psi) = 63$ KeV, $BF(\psi \to \gamma\pi^0) \approx 2\times10^{-5}$.

3.3 Experimental Analysis

In the decay $\psi \to \gamma\pi^0$, the π^0 has an energy of 1545 MeV, corresponding to a minimum opening angle of 10° for the $\pi^0 \to \gamma\gamma$ decay. Over 90% of π^0 decays at this energy will have $\gamma\gamma$ opening angles of less than 13°. This is to be compared to the size of an individual crystal, which subtends an angle of about 12° on each edge. Since electromagnetic showers spread over several crystals, the two showers from the π^0 decay will nearly always overlap, and will usually appear to the standard Crystal Ball offline track reconstruction program as a single track. These events will therefore have the same signature in the Crystal Ball as QED $e^+e^- \to \gamma\gamma$ events, namely, two back-to-back neutral connected regions with energies consistent with the beam energy. How large is this QED background compared to the expected $\gamma\pi^0$ signal? The entire ψ dataset consists of 2.2×10^6 ψ events and a total integrated luminosity of 780 nb^{-1}. Based on the DASP

measurement, we expect approximately 120 $\gamma\pi^0$ decays inside $|\cos\theta_{\gamma-beam}| < .8$. The total QED $e^+e^- \to \gamma\gamma$ cross section for $|\cos\theta_{\gamma-beam}| < .8$ is 19 nb, so the expected QED background is roughly 14,800 events. This corresponds to a signal-to-background ratio of less than 1:125.

Candidate $\gamma\pi^0$ events were selected using essentially the same criteria one would use to select $\gamma\gamma$ events. Exactly two connected regions were required, each with energy in the range 1300-1700 MeV. This energy window is quite large: the expected Crystal Ball energy resolution for 1550 MeV electromagnetic showers is $\sigma(E_\gamma) = 35$ MeV. Bhabha events were removed by demanding that there be no charged tracks observed in the central tracking chambers. One connected region was required to have a neutral track with energy greater than 1000 MeV, while the most energetic track in the other connected region was required to have an energy of at least 600 MeV. The looser requirement for the second connected region allows for the possibility that the two π^0 decay photons are actually resolved as separate tracks by the offline analysis. Finally, the opening angle θ_{12} between the highest energy track in each connected region was required to satisfy $\cos\theta_{12} < -.9$. This back-to-back requirement is nearly 100% efficient for $\gamma\gamma$ and $\gamma\pi^0$ events, even accounting for the effect of the expected distribution of e^+e^- interaction vertex positions. The number of events satisfying these selection criteria was 13,410.

To reject the large QED $\gamma\gamma$ background, these events were processed with the PIFIT algorithm [3.3]. This program performs a maximum likelihood fit to the pattern of energy deposition within a connected region based on the hypothesis that two photons created the shower. PIFIT calculates the energy and momentum of each photon (and hence the $\gamma\gamma$ mass). In addition to the two-photon shower fit, PIFIT also attempts to fit the observed shower with a single

photon. Let $L_{1\gamma}$ indicate the likelihood of this single-photon fit, and $L_{2\gamma}$ the likelihood of the fit with two photons. A comparison of these two likelihoods gives an indication of whether the shower was actually created by two photons. We define the log-likelihood-difference parameter LLD as the difference of the logarithm of these likelihoods:

$$\text{LLD} \equiv \log L_{2\gamma} - \log L_{1\gamma}.$$

For showers created by a single photon, the LLD distribution is peaked near 0, since adding extra degrees of freedom associated with a second photon will not significantly improve the fit. On the other hand, two-photon showers will have a larger value of LLD reflecting the improvement obtained by adding a second photon to the fit. Chapter II contains more detailed information about PIFIT.

Figure 3.2 shows the PIFIT $\gamma\gamma$ mass spectrum of all connected regions for the $\gamma\pi^0$ candidate events. The peak near 50 MeV is due to single photon showers. (The fact that this peak does not have its maximum at 0 is due to shower fluctuations and detector granularity; these cause PIFIT to place the second photon in a different direction than the first in an effort to maximize the fit likelihood.) The tail of $\gamma\gamma$ masses for this single photon peak extends well past the π^0 region. No evidence is seen for a second peak at the π^0 mass above this tail.

To eliminate the $\gamma\gamma$ events, a cut was placed on the LLD parameter. Figure 3.3 shows the distribution of LLD vs PIFIT $M_{\gamma\gamma}$ for the data and for Monte Carlo 1500 MeV photons and π^0's. Photons are associated with low LLD values, while π^0's have a distribution of LLD values extending well above 10. Based on these distributions, the following criteria were used to define the final $\gamma\pi^0$ sample:

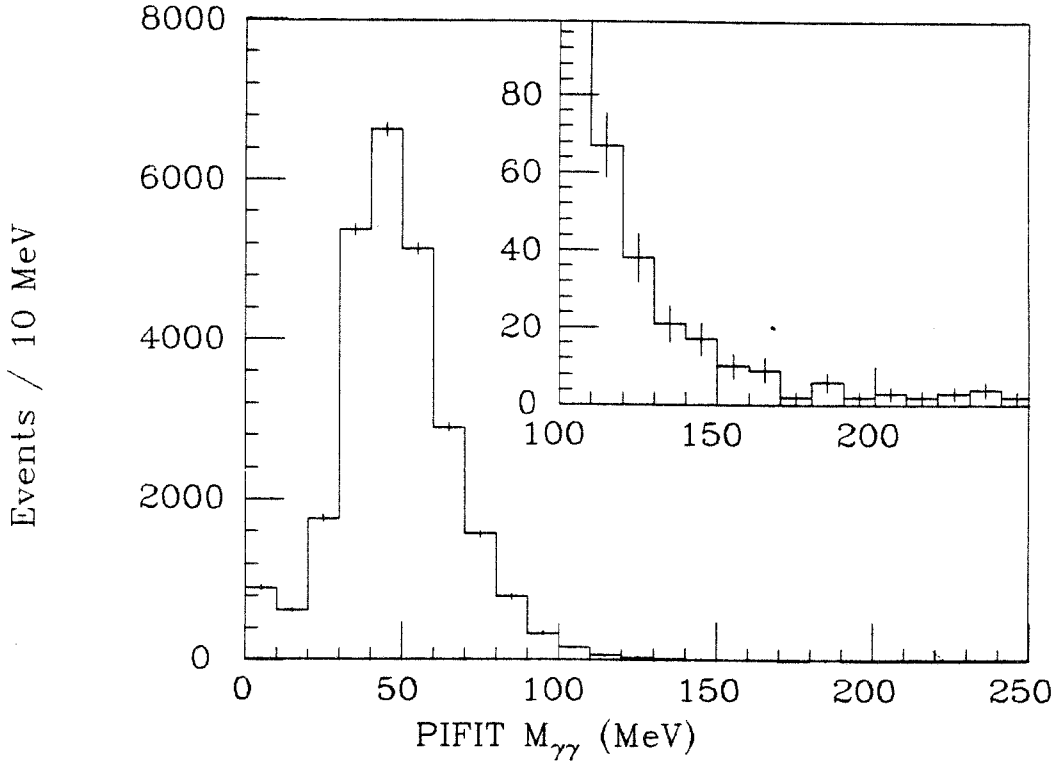

Figure 3.2: Raw PIFIT $\gamma\gamma$ mass spectrum. The insert shows an expanded scale for the tail of the distribution.

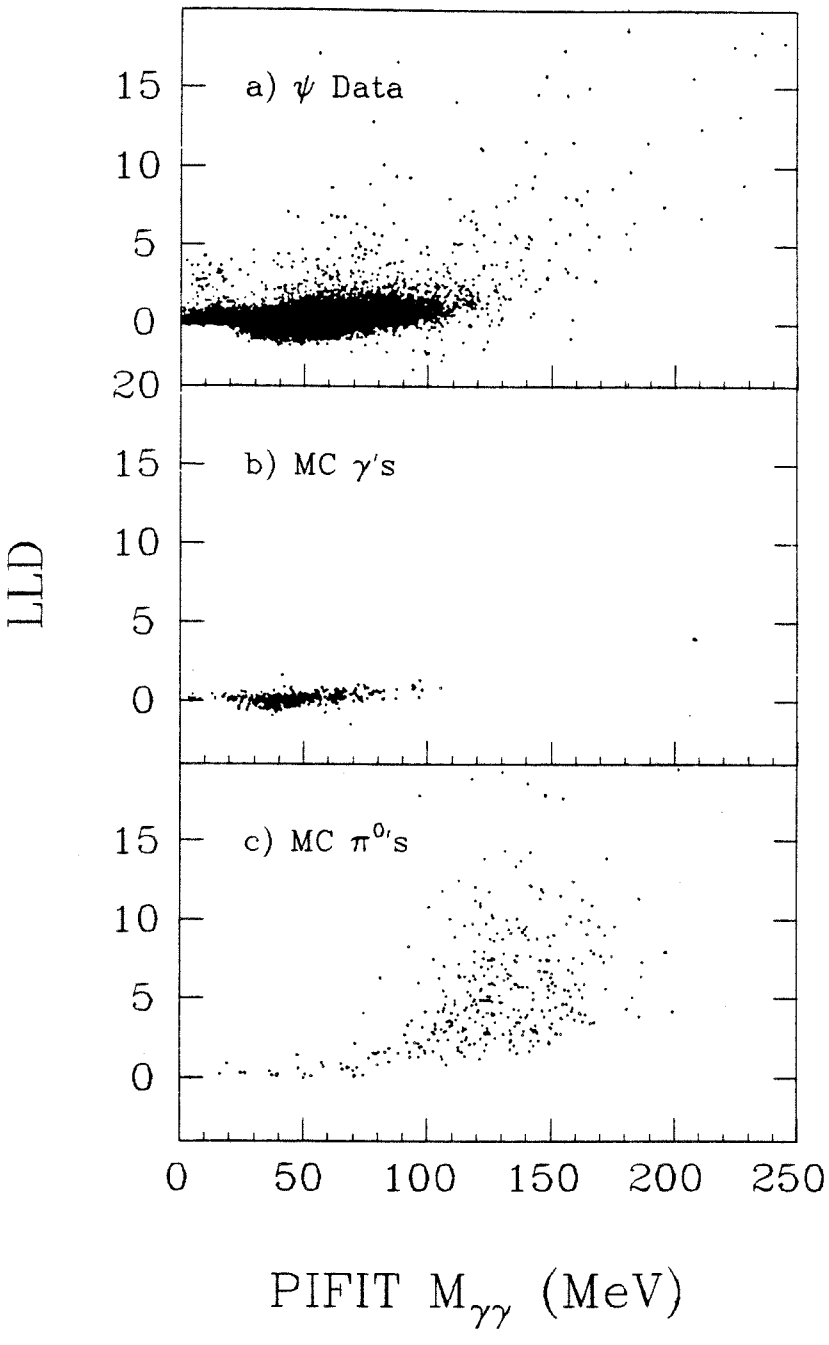

Figure 3.3: PIFIT LLD vs $M_{\gamma\gamma}$ for a) data, b) Monte Carlo photons, and c) Monte Carlo π^0's.

1. For one connected region, $LLD<2$ and $M_{\gamma\gamma}<100$ MeV. This region is the γ candidate.

2. For the other connected region, $LLD>5$. This is the π^0 candidate region.

The requirements for the γ candidate are better than 98% efficient for single photon showers of 1550 MeV, based on Monte Carlo studies. The π^0 requirement, LLD>5, is only 50% efficient for 1550 MeV π^0's, but more importantly provides better than 10^3 rejection of single photon showers. 84 events satisfied this final $\gamma\pi^0$ selection.

Figure 3.4 shows the distribution of $\cos\theta_\gamma$ vs m_{π^0}. for the events satisfying these criteria. The $\gamma\pi^0$ angular distribution is expected to be proportional to $1+\cos^2\theta_\gamma$, while the QED background goes as $\frac{(1+\cos^2\theta)}{(1-\cos^2\theta)}$, and thus is very strongly peaked along the beam axis. The two angular distributions are compared in Figure 3.5. Most of the events in Figure 3.5 appear at large values of $|\cos\theta_\gamma|$, but a band of events at the π^0 mass is visible with a more uniform $\cos\theta_\gamma$ distribution. Selecting events with $|\cos\theta_\gamma| < .8$ and plotting $M_{\gamma\gamma}$ yields Figure 3.6. An excess of events is seen at the π^0 mass. In addition, there is also a smaller accumulation of events around a mass of 70 MeV. These are presumably single photon showers with unusually large LLD values: the LLD distribution for single photons does have a small tail extending beyond the main peak near LLD=0.

This spectrum has been fit to a sum of two Gaussians plus a constant background over the range 30 - 250 MeV. The positions and widths of the Gaussians were allowed to vary. The widths of the peaks are consistent with the widths of PIFIT $M_{\gamma\gamma}$ distributions for samples of 1500 MeV photons and π^0's. The π^0 peak contains 21.1 ± 5.6 events, and is centered at 139.0 ± 4.2 MeV, consistent with the

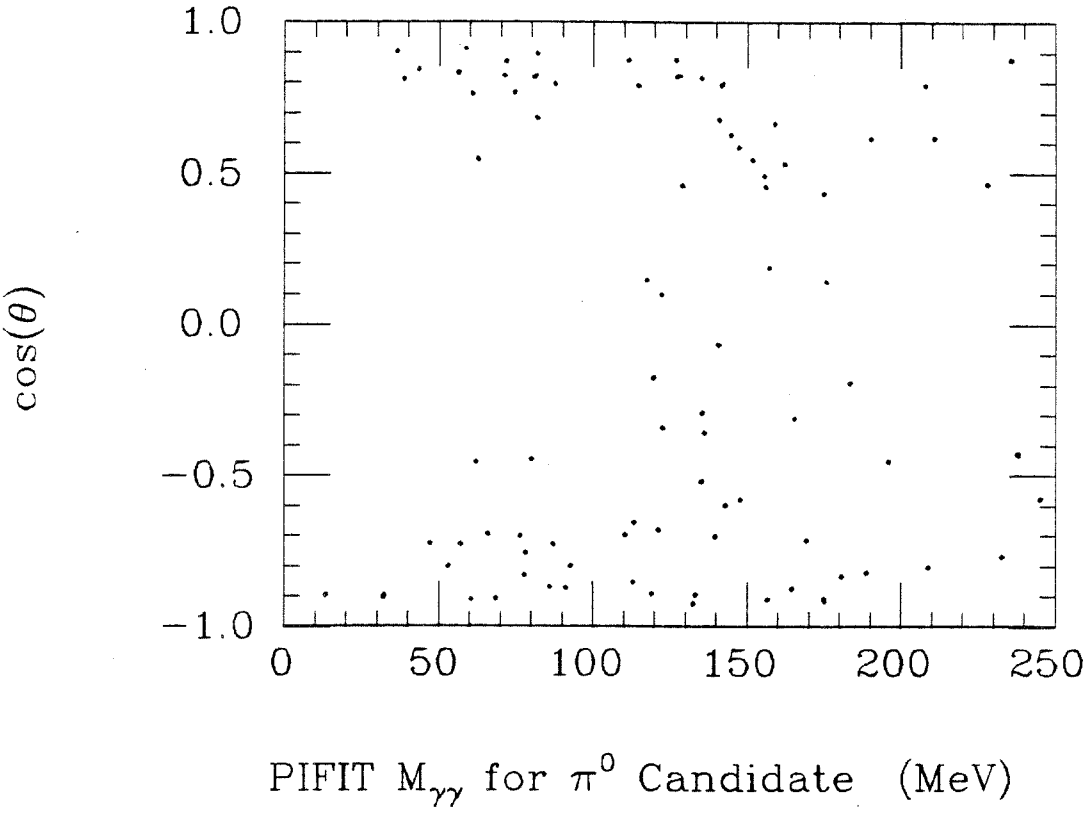

Figure 3.4: $\cos\theta_\gamma$ vs. M_{π^0} for the $\gamma\pi^0$ candidates.

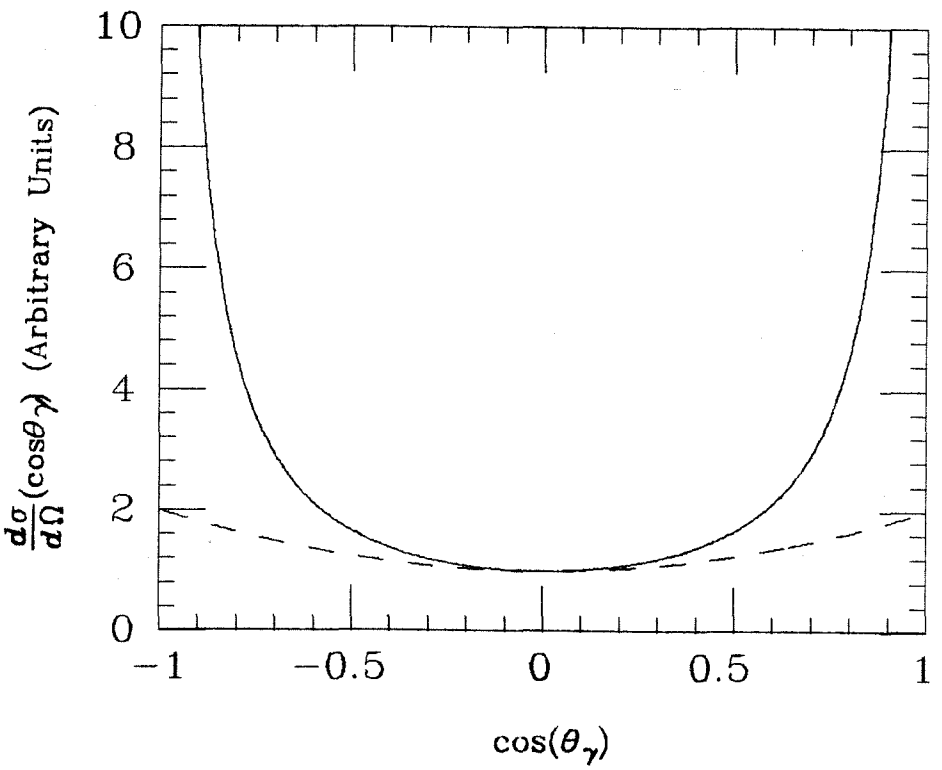

Figure 3.5: Expected angular distributions for $e^+e^- \to \gamma\gamma$ and $\psi \to \gamma\pi^0$. The scale is arbitrary.

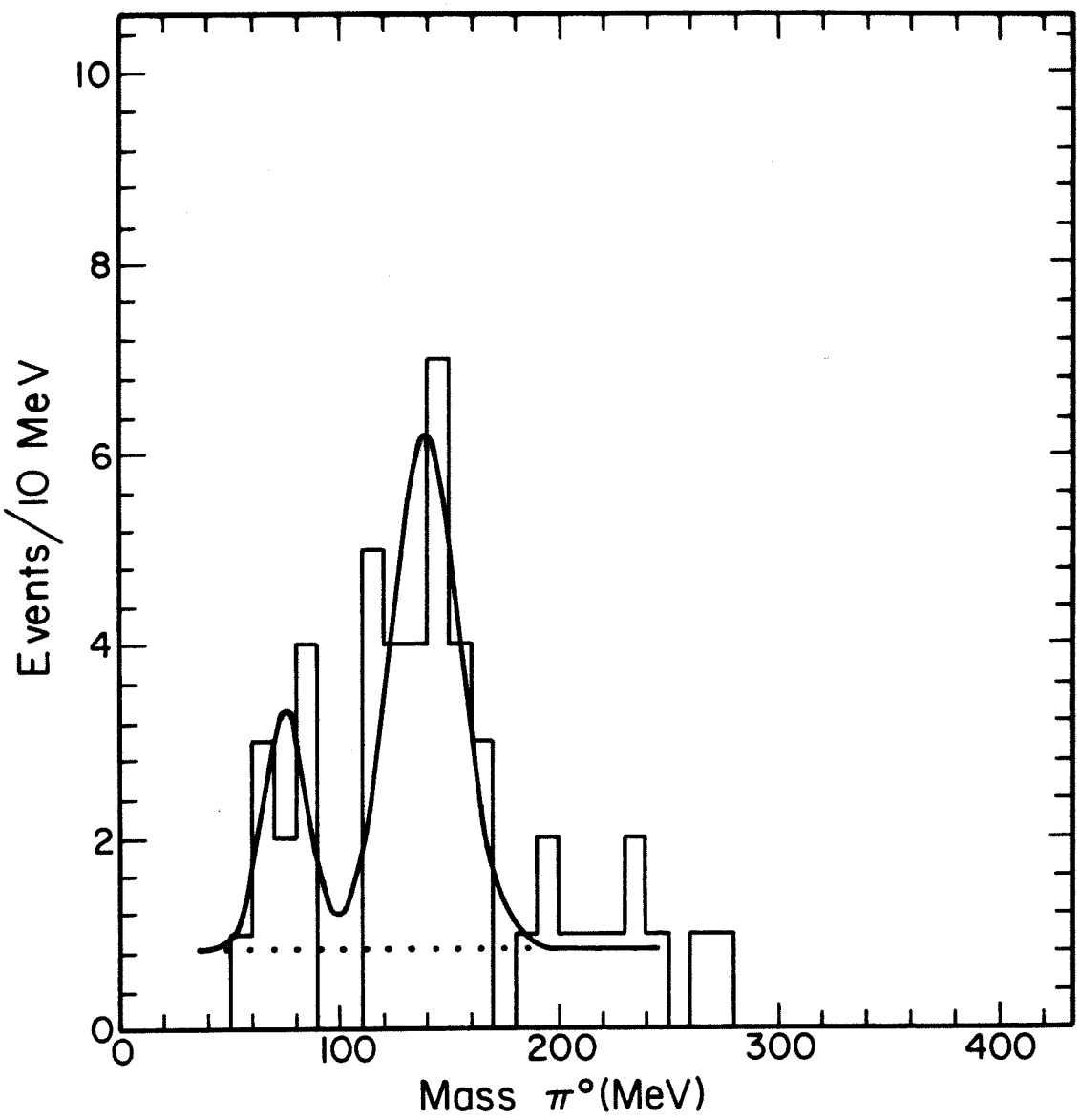

Figure 3.6: Final PIFIT $\gamma\gamma$ mass spectrum for π^0 candidates, with a fit to two Gaussians plus a flat background.

π^0 mass, and with PIFIT Monte Carlo results. The χ^2 is 14 for 15 degrees of freedom.

The efficiency of the analysis has been determined by generating a sample of $\psi \to \gamma\pi^0$ Monte Carlo events, distributed with the expected $1 + \cos^2\theta_\gamma$ angular distribution. The efficiency is thus determined to be 27%, and the resulting branching fraction for the observed signal is $(3.6 \pm 1.1) \times 10^{-5}$, where the error is statistical only.

3.4 Systematic Errors

The greatest contributions to the systematic error are the uncertainty in the LLD distribution for π^0's, and the uncertainty in the shape of the background used when fitting the PIFIT M_{π^0} mass plot. All other cuts used in the analysis are either very efficient or easily understood by studying Monte Carlo events. The uncertainty in the LLD distribution is due to the fact that PIFIT results depend critically on the explicit pattern of energy deposited in a connected region. Effects not included in the Monte Carlo (both physics- and detector-related) could lead to differences in the exact nature of shower fluctuations between data and Monte Carlo events.

What is needed to better understand the LLD distribution is a very clean sample of high energy π^0's. Comparing the LLD distribution for these real π^0's with the same distribution for Monte Carlo π^0's would test the ability of the Monte Carlo to accurately predict the LLD distribution. The level of disagreement between the two distributions would provide a measure of the systematic error for the detection efficiency which is incurred due to uncertainty in the LLD distribution. The decay $\psi' \to \gamma\chi(3415) \to \gamma\pi^0\pi^0$ provides just such a sample. Based on the measured branching fractions of $8.2 \pm 1.4\%$ for $\psi \to \gamma\chi(3415)$ and $0.9 \pm 0.2\%$

for $\chi(3415)\rightarrow\pi^+\pi^-$ [3.5], and assuming isospin invariance for the χ decay, we expect roughly 650 ± 190 $\gamma\pi^0\pi^0$ decays from the ψ' dataset. The π^0's associated with this decay have a uniform energy distribution from 1575 to 1835 MeV. Although slightly higher in energy than the π^0's from $\psi\rightarrow\gamma\pi^0$, they should provide a good test of the ability of the Monte Carlo to correctly simulate the LLD distribution for fast π^0's.

To obtain this sample of χ decays, ψ' events with three neutral connected regions have been fit to the hypothesis $\psi'\rightarrow\gamma\chi(3415)$, $\chi\rightarrow\pi^0\pi^0$. Energy and momentum conservation provide four constraints, while the constraint on the $\pi^0\pi^0$ mass provides another. However, because these events have no charged tracks, one constraint is used up in determining the z-vertex; thus this is a 4-C fit. Candidate events were required to have a fit probability of at least 10%. In addition, both high energy connected regions were required to have PIFIT $\gamma\gamma$ masses above 80 MeV. This eliminates any 3γ QED background as well as $\gamma\gamma$ decays of the $\chi(3415)$. For comparison, 500 Monte Carlo π^0's were generated with E_{π^0}=1750 MeV. Figure 3.7 shows the LLD distribution for both datasets. The agreement is very good, although there is some evidence for the data peaking at slightly lower values. Figure 3.8 shows the efficiency of the cut LLD>*LLDMIN* as a function of *LLDMIN* for both datasets. Based on the agreement between the Monte Carlo and $\chi(3415)$ data, we place a systematic uncertainty of 10% on the final branching fraction due to uncertainty in the LLD distribution and the resulting uncertainty in the efficiency of the LLD cut.

The only other significant source of systematic error is due to the mass fit itself. The fluctuation of the fit result due to changing the background shape leads us to place a 15% systematic error on the branching fraction due to uncertainty in the shape of the background. Combining these two sources of

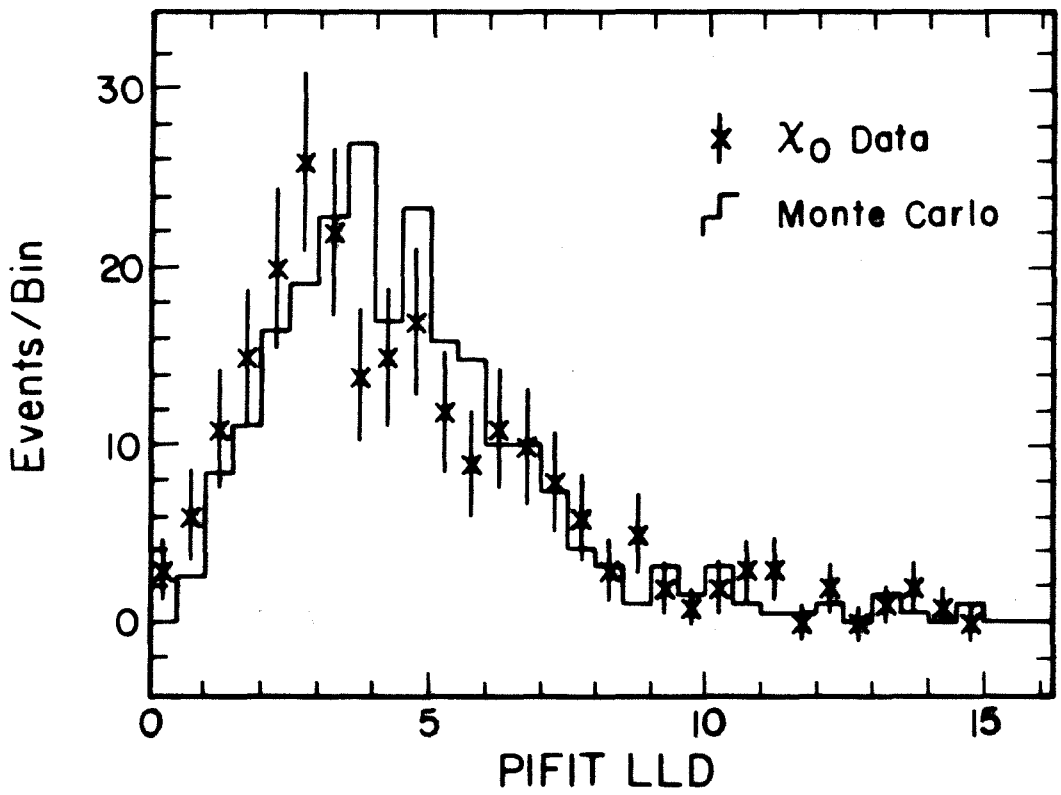

Figure 3.7: LLD distribution for 1750 MeV Monte Carlo π^0's and for π^0's from $\chi(3415)$ decays.

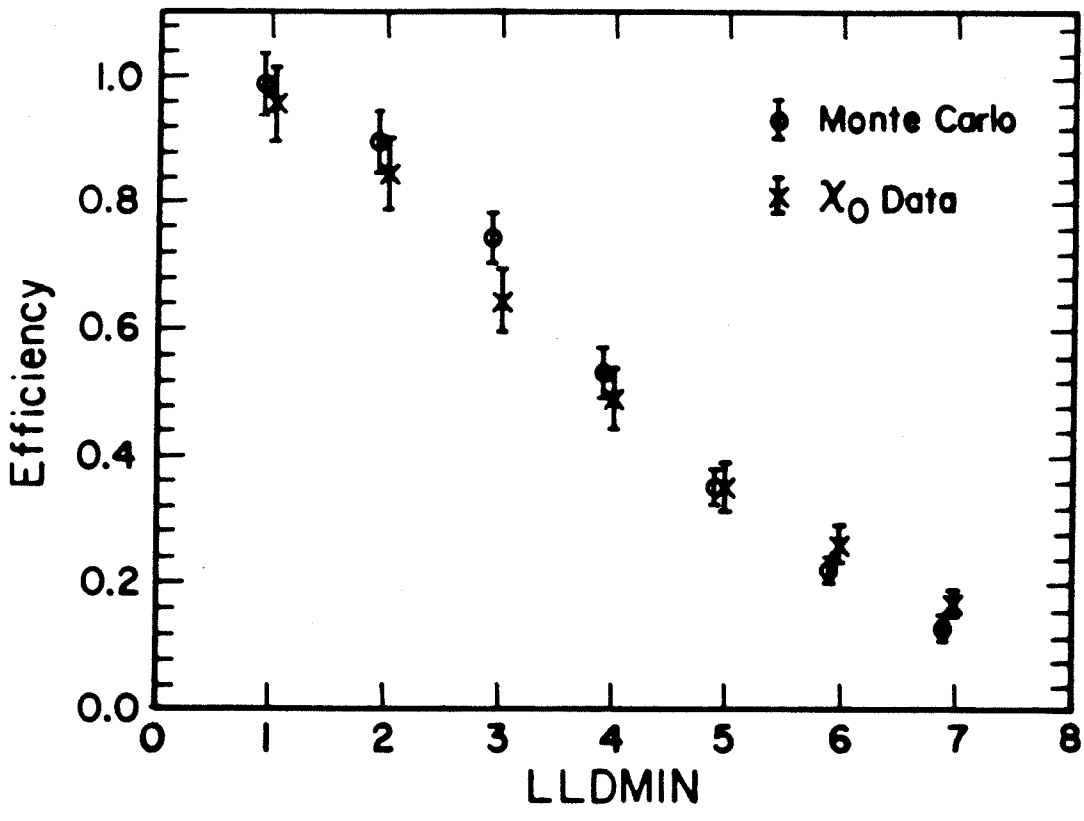

Figure 3.8: Efficiency of the cut LLD>*LLDMIN* as a function of *LLDMIN*.

systematic error results in an overall systematic error of 0.7×10^{-5} for the $\gamma\pi^0$ branching fraction. Thus the final result is $BF(\psi\rightarrow\gamma\pi^0) = (3.6\pm1.1\pm0.7)\times10^{-5}$.

3.5 Background Checks

Several checks have been performed to investigate the validity of the signal. The problem of the enormous QED background can be eliminated by looking at ψ decays originating from hadronic decays of the ψ'. With the Crystal Ball dataset of 1.8×10^6 produced ψ' events, one expects 21 events of the type $\psi'\rightarrow\pi^+\pi^-\psi$, $\psi\rightarrow\gamma\pi^0$, based on the cascade rate $BF(\psi'\rightarrow\pi^+\pi^-\psi) = 33\%$, and the $\gamma\pi^0$ decay rate measured from the ψ dataset. With a 20% detection efficiency, a signal of four events is expected. 27 ψ' events fit the hypothesis $\psi'\rightarrow\pi^+\pi^-\psi$, $\psi\rightarrow\gamma\gamma$ with 10% likelihood or better. These events were then processed with PIFIT to see if one of the neutral connected regions was in fact a π^0. Of these 27 events, two events had one connected region detected as a π^0 by PIFIT. Nearly all the remaining events appeared to be e^+e^- decays of the ψ, where the charged tracks were not tagged due to chamber inefficiencies. While not statistically compelling, observing these two events in a channel free of QED contamination is encouraging.

To further ensure that the signal is indeed associated with ψ decays, and not simply an artifact of the large QED background, the analysis has been repeated for the 562 nb^{-1} of off-resonance data at E_{CM}=3.67 GeV. No structure is seen in the PIFIT $\gamma\gamma$ mass spectrum at the π^0 mass, as shown in Figure 3.9a. The QED background has been further studied by generating 10,000 2γ and 3γ Monte Carlo events using the Berends-Kleiss QED Monte Carlo [3.6]. Once again, the PIFIT $\gamma\gamma$ spectrum of Figure 3.9b shows no significant structure at the π^0 mass. Finally, the decay $\psi\rightarrow\gamma f$, $f\rightarrow\pi^0\pi^0$ has been considered as a possible

background. When the f decays along its direction of motion, it produces a high energy π^0 opposite the primary radiated photon. If the two photons from the soft π^0 are lost, the event can assume the signature of a $\gamma\pi^0$ event. Given the branching fractions $BF(\psi\rightarrow\gamma f) = 1.5\times10^{-3}$, and $BF(f\rightarrow\pi^0\pi^0) = .28$, one expects about 900 $\psi\rightarrow\gamma f\rightarrow\gamma\pi^0\pi^0$ events. From a sample of 1800 Monte Carlo events of this decay, 36 events satisfied the loose pre-PIFIT selection criteria. However, only one event survived the $\gamma\pi^0$ criteria after PIFIT.

3.6 Conclusions

To summarize, the decay $\psi\rightarrow\gamma\pi^0$ has been observed with a branching fraction of $(3.6\pm1.1\pm0.7)\times10^{-5}$. The pattern recognition algorithm PIFIT played an essential role in rejecting the enormous QED $\gamma\gamma$ background. Two events of the type $\psi'\rightarrow\pi^+\pi^-\psi$, $\psi\rightarrow\gamma\pi^0$ have been observed, consistent with the expected rate from the ψ dataset. Possible backgrounds have been ruled out by studies of Monte Carlo and off-resonance data. The accuracy of the Monte Carlo at predicting the LLD distribution for high energy π^0's has been confirmed by studying fast π^0's from $\chi(3415)$ decays.

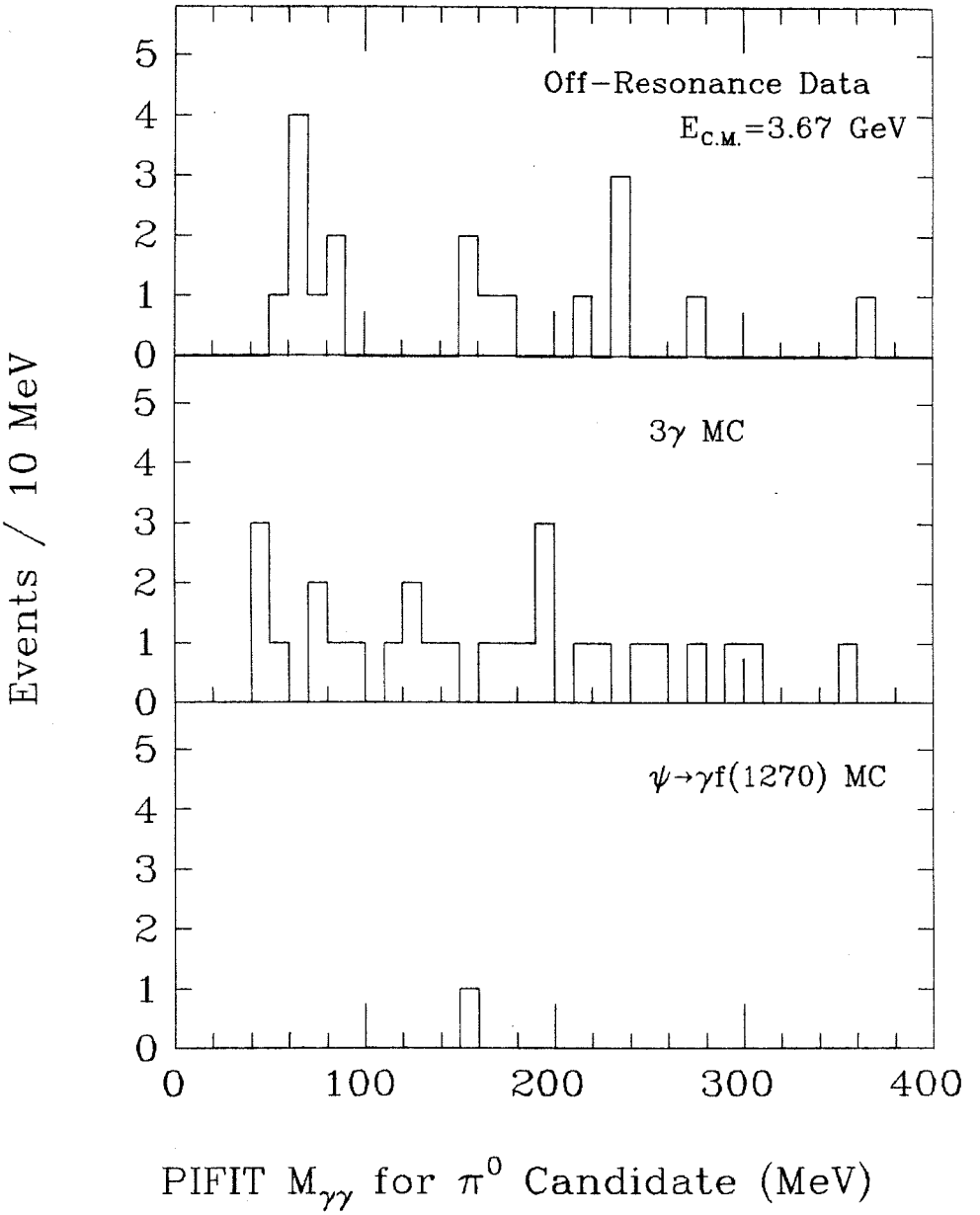

Figure 3.9: PIFIT $\gamma\gamma$ mass spectra for a) off-resonance data at $E_{C.M.}$ = 3.67 GeV; b) QED 3γ Monte Carlo; c) f (1270) Monte Carlo

Chapter III References

[3.1] R. Partridge *et al.*, Phys. Rev. Lett. 44, 712 (1980).

[3.2] W. Braunschweig *et al.*, Phys. Lett. 67B, 243 (1977).

[3.3] D. L. Scharre, SLAC-PUB-2519 (1980).

[3.4] R. P. Feynman, *Photon-Hadron Interactions* (W. A. Benjamin, Inc., Reading, 1972), p82.

[3.5] Review of Particle Properties, Phys. Lett. 111B, (1982).

[3.6] R. Kleiss, thesis, Leiden University, Print RX-988 Leiden, 1982 (unpublished); F. A. Berends and R. Kleiss, Nucl. Phys. B186, 22 (1981).

Chapter IV

A Study of the Cascade Decay

$\psi \to \gamma X,\ X \to \gamma\rho$

4.1 Introduction

The study of radiative ψ decays has not only increased our understanding of the charmonium system; it has also led to the discovery of several new hadronic states. We can in turn search for radiative decays of these new states, yielding information on their spin-parity assignments and their quark-glue structure. In this chapter we present results of a search for the cascade process

$$\psi \to \gamma X \quad \begin{array}{l} \hookrightarrow \gamma\rho^0 \\ \qquad \hookrightarrow \pi^+\pi^- \end{array} . \tag{4.1}$$

In particular, this search was motivated by a desire to find radiative decays of the $\iota(1440)$. After reviewing the experimental status of the ι, we will discuss mixing models for the pseudoscalar mesons and their predictions for radiative ι decay rates, and then present results for the $\gamma\gamma\rho$ final state.

4.2 The $\iota(1440)$ and Pseudoscalar Mixing Models

The $\iota(1440)$ was first observed by the Mark II experiment at the SPEAR e^+e^- storage ring in the radiative decay $\psi \to \gamma K^{\pm} K_s \pi^{\mp}$ [4.1]. Soon thereafter the Crystal Ball observed a similar signal in $\psi \to \gamma K^+ K^- \pi^0$ [4.2]. The resonance events were found to be correlated with a low $K\overline{K}$ mass, interpreted as evidence for the decay sequence $\iota \to \delta(980)\pi$, $\delta \to K\overline{K}$. A partial wave analysis of the $K\overline{K}\pi$ final state by the Crystal Ball determined the ι to be a pseudoscalar, $J^{PC} = 0^{-+}$. In addition, this analysis showed that most of the $K\overline{K}\pi$ decays went through an intermediate

$\delta\pi$ state:

$$\frac{BF(\iota\to\delta\pi)}{BF(\iota\to K^*\bar{K}+c.c.)+BF(\iota\to\delta\pi)} > .75 \ (90\%C.L.).$$

The Mark III experiment, currently at SPEAR, has reported observation of the ι in several $K\bar{K}\pi$ charge modes [4.3], but as of this writing has made no statement regarding the spin and parity of the state. Table 4.1 summarizes the experimental status of the ι.

Table 4.1 Experimental Status of ι

Experiment: [reference]:	Crystal Ball [4.2]	Mark II [4.1]	Mark III [4.3] (Preliminary)
Mode:	$K^+K^-\pi^0$	$K^\pm K_s\pi^\mp$	$K^+K^-\pi^0$
Mass (MeV):	1440^{+20}_{-15}	1440^{+10}_{-15}	1460±10
Γ (MeV):	55^{+20}_{-30}	50^{+30}_{-20}	97±25
$BF(\psi\to\gamma\iota)$ $\times BF(\iota\to KK\pi)$:	(4.0±0.7±1.0) $\times10^{-3}$	(4.3±1.7) $\times10^{-3}$	(5.3±0.6±1.9) $\times10^{-3}$

(The Mark III also observes the ι in $K^\pm K_s\pi^\mp$ and $K_sK_s\pi^0$ decay modes, but does not report ι resonance parameters for these modes.)

Comparing this *product branching fraction* to other ψ radiative decays to pseudoscalars, we find that the ι is quite copiously produced. Table 4.2 compares these different rates. We see that even if the $K\bar{K}\pi$ mode accounts for nearly all of the ι decays, the inclusive rate for $\psi\to\gamma\iota$ is roughly the same as the large $\psi\to\gamma\eta'$ rate; only the OZI-allowed transition to the η_c has a substantially larger rate. If there are other significant ι decay modes, the total rate for ι production could be much larger than the η' rate.

Table 4.2	Comparison of $\psi \to \gamma 0^{-+}$ Decays
Decay	Branching Fraction
$\psi \to \gamma \eta_c$	$1.20^{+0.53}_{-0.35} \times 10^{-2}$ [4.4]
$\psi \to \gamma \eta'$	$(4.1 \pm 0.3 \pm 0.6) \times 10^{-3}$ [4.5]
$\psi \to \gamma \pi^0$	$(3.6 \pm 1.1 \pm 0.7) \times 10^{-5}$ [4.5]
$\psi \to \gamma \eta$	$(8.8 \pm 0.8 \pm 1.1) \times 10^{-4}$ [4.5]
$\psi \to \gamma \iota \to \gamma K\bar{K}\pi$	$(4.0 \pm 0.7 \pm 1.0) \times 10^{-3}$ [4.2]

Given this very large production rate in radiative ψ decays, and the fact that both lattice and bag-model calculations predict a pseudoscalar glueball in the 1-2 GeV mass range, the ι becomes a prime candidate to be a glueball state. However, as noted in Chapter I, mixing is expected between pure glueballs and pure $q\bar{q}$ mesons. The observed deviation from ideal mixing within the pseudoscalar nonet has been cited as evidence for strong quark-glue mixing within the $J^P=0^-$ mesons [4.6].

Because photons couple only to charged particles, electromagnetic interactions provide a useful probe for determining the amount of $q\bar{q}$ and gg in the wave function of a mixed physical state. Thus a search for the radiative decay $\iota \to \gamma\rho$ allows us to investigate the constituent structure of the ι, determine if it is indeed primarily a gluonic state, and measure the amount of $q\bar{q}$ in its wave function due to mixing.

Several theoretical models make predictions for radiative ι decays. The basic premise of each is that radiative ι decays are mediated by the mixing of the ι with the η and η', or in other words that the radiated photon couples to the quark component of the ι. Bag model calculations by Carlson and Hansson [4.7] determine ι-η'-η mixing via an explicit perturbative calculation of the coupling of a pseudoscalar $q\bar{q}$ pair to a pseudoscalar glueball, composed of two gluons, one in the TE mode and one in the TM mode. They find $\langle \eta' | \iota \rangle = .44$ and

$\langle \eta | \iota \rangle = -.27$, yielding a prediction $\Gamma(\iota \to \gamma\rho) = 16$ keV.

Iwao has investigated the radiative ι decays in the context of a "pseudoscalar meson dominance" model [4.8]. Just as the electromagnetic current couples to hadrons via ρ, ω, and φ in vector meson dominance, here the ι current couples dominantly through the pseudoscalar mesons η and η'. Depending on the relative phase of the $\eta'\gamma\rho$ and $\eta\gamma\rho$ couplings, this model predicts $\Gamma(\iota \to \gamma\rho) = 213$ or 413 keV, a factor of ten or twenty greater than the bag model prediction.

Senba and Tanimoto treat ι–η–η' mixing by means of the pseudoscalar anomaly [4.9]. Identifying the pseudoscalar glueball with the current $G^a_{\mu\nu}\tilde{G}^{\mu\nu}_a$, where $G^a_{\mu\nu}$ is the QCD gluon field-strength tensor with space time indices μ and ν and color index a, they arrive at a model in which ι decays are mediated by first coupling the ι to the pseudoscalars η and η' through anomalous couplings $\langle G^{\mu\nu}_a \tilde{G}^a_{\mu\nu} | \eta, \eta' \rangle$. Adding constraints on various couplings from SU(3) flavor symmetry, they obtain $\Gamma(\iota \to \gamma\rho) = 4.2$ MeV, over two orders of magnitude larger than the bag model prediction.

Finally, Pinsky and Palmer use a pole mixing model in which $\gamma\rho$ decays occur through an intermediate η' [4.10]. Radiative ψ decays are used to fix the size of the various couplings, and an $\iota \to \gamma\rho$ decay width of 3.5 MeV is obtained. Table 4.3 reviews the various theoretical predictions.

Experimentally, we measure the product branching fraction

$$BF(\psi \to \gamma\iota) \times BF(\iota \to \gamma\rho) = BF(\psi \to \gamma\iota) \frac{\Gamma(\iota \to \gamma\rho)}{\Gamma_{tot}(\iota)}.$$

Taking the mean of the results in Table 4.1, we have $\Gamma_{tot}(\iota) = 67 \pm 15$ MeV. Unfortunately, the inclusive branching fraction $BF(\psi \to \gamma\iota)$ is not known. Only the product branching fraction into the $K\bar{K}\pi$ final state has been measured. Referring to

Table 4.1, we see that the world average for this product branching fraction is $(4.4\pm1.1)\times10^{-3}$. Putting all these factors together, we find that the product branching fraction for $\psi\to\gamma\iota\to\gamma\gamma\rho$ is related to the theoretically predicted $\Gamma(\iota\to\gamma\rho)$ by:

$$BF(\psi\to\gamma\iota)\times BF(\iota\to\gamma\rho) = \frac{4.4\times10^{-3}}{BF(\iota\to K\bar{K}\pi)}\ \frac{\Gamma(\iota\to\gamma\rho)}{(67\ \mathrm{MeV})}.$$

The fact that the ι has been seen only in the $K\bar{K}\pi$ decay mode indicates that $BF(\iota\to K\bar{K}\pi)$ could be near one. In any event, this formula gives us a lower limit on the expected number of $\iota\to\gamma\rho$ events for each of the mixing models mentioned above.

Table 4.3	Theoretical Predictions for $\iota\to\gamma\rho$	
Model	$\Gamma(\iota\to\gamma\rho)$ (MeV)	# Events in ψ Dataset
Bag Model [4.7]	0.016	> 2 events
Pseudoscalar Meson Dominance [4.8]	.213 or .413	> 31 events
Anomalous Mixing [4.9]	4.2	> 600 events
Pole Mixing [4.10]	3.5	> 500events

4.3 Experimental Analysis

Candidate events were required to have exactly two charged and two neutral tracks, with all tracks satisfying $|\cos\theta_{i-beam}|<.9$, and all track pairs satisfying $\cos\theta_{ij}<.95$, where θ_{i-beam} is the angle track i relative to the e^+ beam direction, and θ_{ij} is the angle between tracks i and j. No extra tracks were permitted in the candidate events. Although permitting extra photons would allow us to recover events with spurious splitoff tracks, it would also contaminate the $\gamma\gamma\pi^+\pi^-$ event sample with events from higher multiplicities. For example, events from the process $\psi\to\gamma\iota$, $\iota\to K^+K^-\pi^0$, which yields a final state of two

charged and three neutral tracks, would be accepted if the multiplicity requirements were relaxed. Such events could in principle generate an ι signal in fits to $\psi \to \gamma\gamma\pi^+\pi^-$, in which the lowest energy photon was ignored. Thus it was decided to apply stringent multiplicity requirements at the initial event selection stage, accepting a loss in efficiency in return for a cleaner event sample.

The 16,032 events which passed the initial event selection were kinematically fit to the two-constraint hypothesis $\psi \to \gamma\gamma\pi^+\pi^-$. The fit likelihoods are shown in Figure 4.1; only events with greater than 10% fit likelihood were considered in the remaining analysis. The dominant process populating this final state is the hadronic decay $\psi \to \rho\pi$, which has a 1.22% branching fraction, making it the largest known exclusive hadronic decay mode of the ψ. The spectrum of fit $\gamma\gamma$ masses in Figure 4.2 exhibits a large π^0 signal, primarily due to this $\rho\pi$ decay. To eliminate this background, events were removed if the fit $\gamma\gamma$ mass was in the range 75-200 MeV. A small η signal was also observed in the $\gamma\gamma$ mass spectrum of the candidate events; these were removed by a similar cut, requiring the $\gamma\gamma$ mass to be outside the range 500-600 MeV.

Figure 4.3 shows a scatterplot of $M_{\pi\pi}$ vs. $M_{\gamma\pi\pi}$ after removing events with a π^0 or η, with two entries per event. Several features are clearly visible in this plot. First, the small concentration of events at the very lower left hand corner of the scatterplot is due to the process $\psi \to \gamma\eta$, $\eta \to \gamma\pi^+\pi^-$. Next, a clear enhancement is seen at $M_{\gamma\pi\pi}$ near 950 MeV, due to the decay sequence $\psi \to \gamma\eta'$, $\eta' \to \gamma\rho$. The other $\gamma\pi\pi$ combination for these η' events formsa band of events at high $\gamma\pi\pi$ masses. Events along the diagonal $M_{\gamma\pi\pi} \approx M_{\pi\pi}$ are probably associated with a residual contamination of $\gamma\pi^+\pi^-$ and γK^+K^- events containing an extra splitoff track. Because splitoff tracks are of low energy and are usually close to their parent hadron track, they do not add much to the $\gamma\pi\pi$ invariant mass, and thus

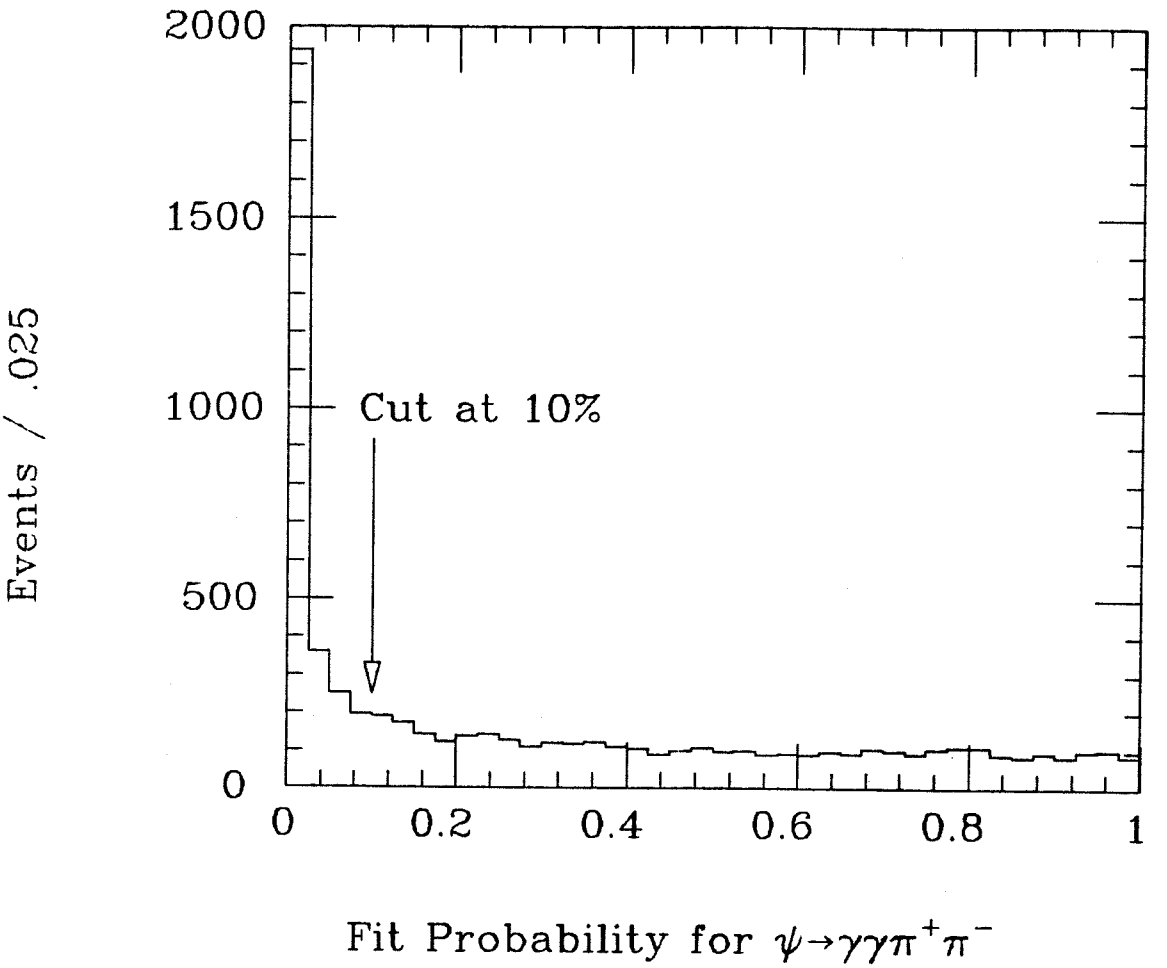

Figure 4.1: Chi-squared fit probability for kinematic fits to the hypothesis $\psi \to \gamma\gamma\pi^+\pi^-$. Only events with fir probabilities of greater than 10%, as indicated in the figure, are accepted for further analysis.

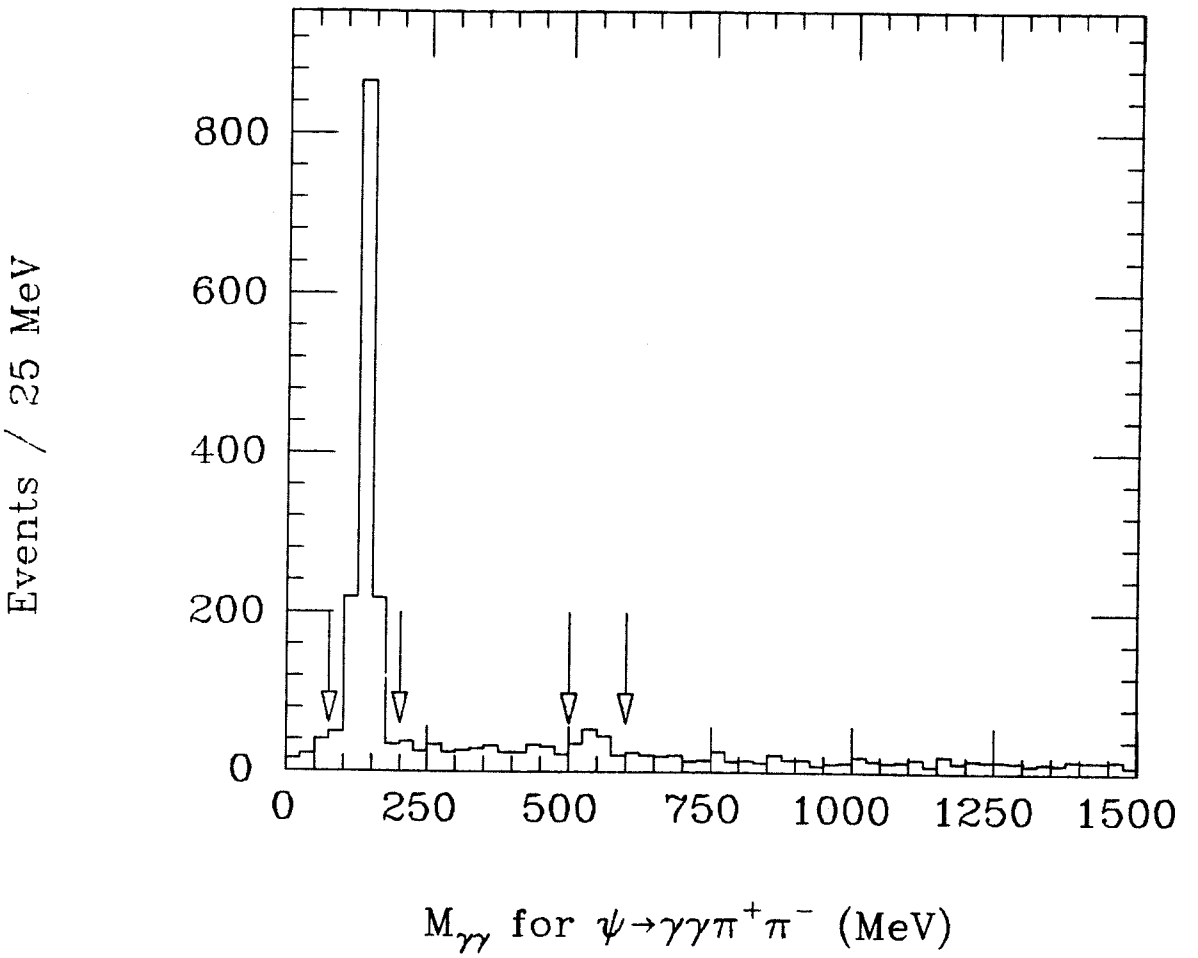

Figure 4.2: Fit $\gamma\gamma$ masses for $\gamma\gamma\pi^+\pi^-$ events. Events with $\gamma\gamma$ masses in the indicated π^0 and η windows are removed from the analysis.

these events are expected to have $M_{\gamma\pi\pi}$ only slightly larger than $M_{\pi\pi}$.

To reduce contamination from these splitoff events, the routine SPLIT has been used to identify neutral showers which are caused by splitoffs from hadronic tracks, based on the energy, shower pattern, and proximity of the neutral shower to a charged track. Of the π^0- and η-subtracted events, 16% had one or both neutral showers identified as splitoffs by the SPLIT routine, and were eliminated from the analysis. The scatterplot of $M_{\pi\pi}$ vs. $M_{\gamma\pi\pi}$ for the remaining events, shown in Figure 4.4, shows a reduced level of background along the diagonal $M_{\pi\pi} \approx M_{\gamma\pi\pi}$.

To further investigate the $\gamma\gamma\rho$ final state, we select those events in which the $\pi^+\pi^-$ mass is in the range 570-920 MeV. The $M_{\gamma\pi\pi}$ mass spectrum for these ρ events is displayed in Figure 4.5, showing a prominent η' signal. (There are still two entries per event.) In addition, there is a hint of a small enhancement around 1400 MeV. This second enhancement can be better seen in a scatterplot of $M^{lo}_{\gamma\pi\pi}$ vs. $M^{hi}_{\gamma\pi\pi}$, the low and high $\gamma\pi\pi$ mass combinations, as in Figure 4.6. Here we see two bands associated with peaks in the $M^{lo}_{\gamma\pi\pi}$ spectrum: the most prominent one due to the η', and a second one near 1400 MeV. Figure 4.7 is the low-mass projection of this plot, with the vertical scale expanded to show the structure at 1400 MeV.

The η' signal provides a good means of checking the overall energy calibration and mass resolution for this final state. Ignoring for a moment the higher mass enhancement, we have fit the mass range 600-1200 MeV with a single Gaussian peak of variable width. The best fit yielded a central value of 956.8±2.5 MeV, in good agreement with the established η' mass of 957.57±0.25 MeV [4.11]. The η' mass resolution for this final state was determined to be 49±3 MeV, in accord with expectations from Monte Carlo studies.

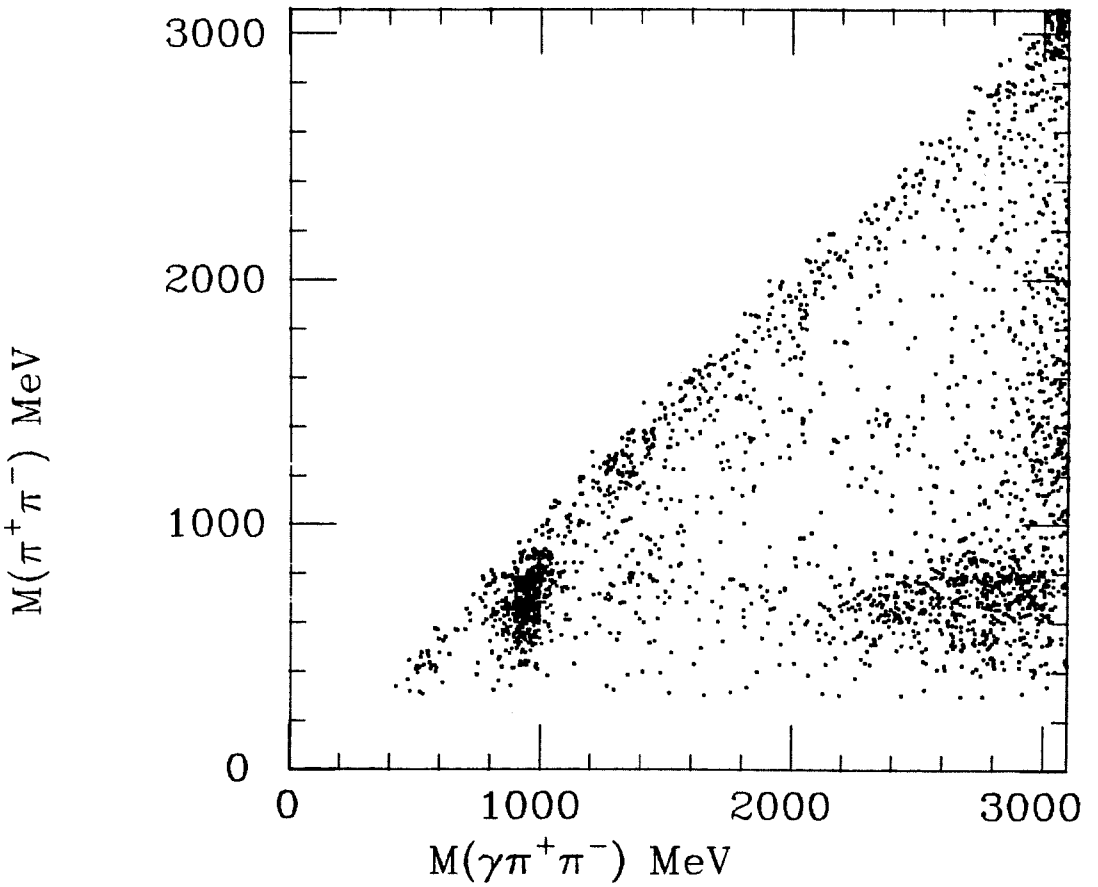

Figure 4.3: $M_{\pi\pi}$ vs. $M_{\gamma\pi\pi}$ for fit $\gamma\gamma\pi^+\pi^-$ events.

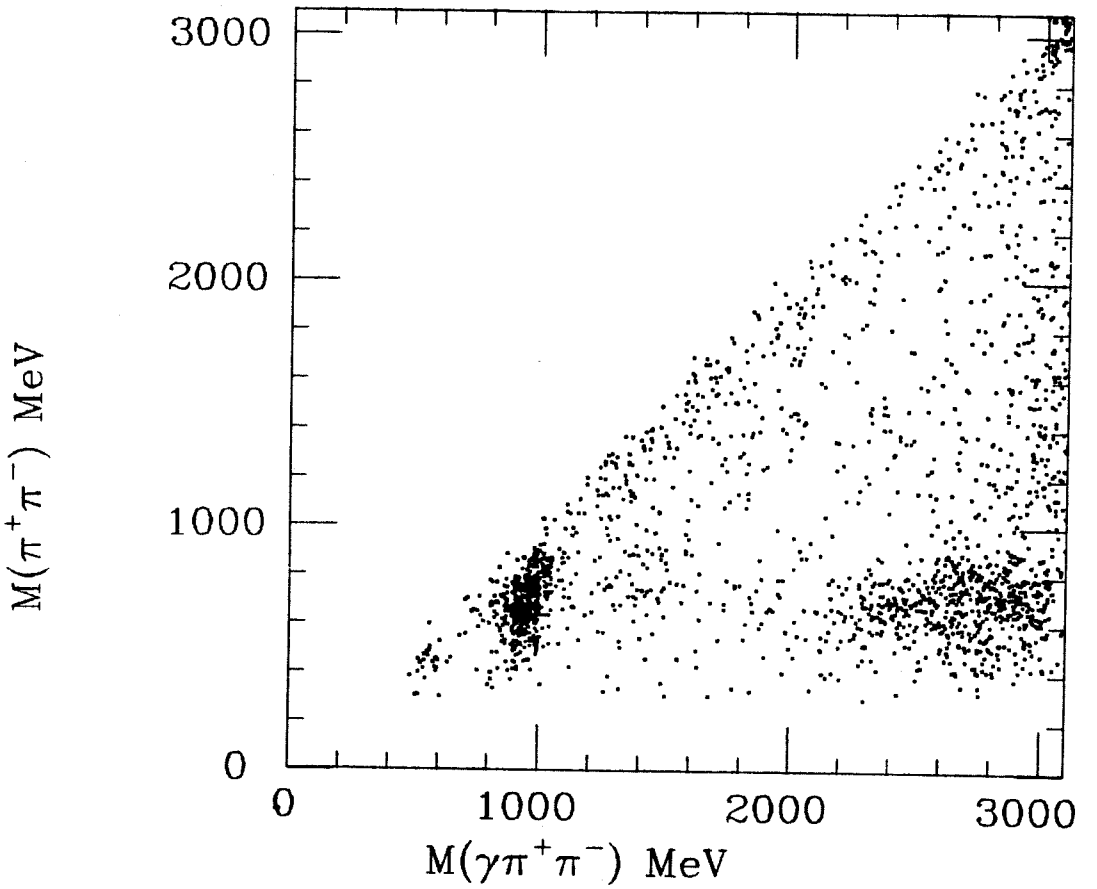

Figure 4.4: $M_{\pi\pi}$ vs. $M_{\gamma\pi\pi}$ after using the SPLIT algorithm to remove events in which one of the neutral showers is identified as a splitoff from one of the charged hadron showers.

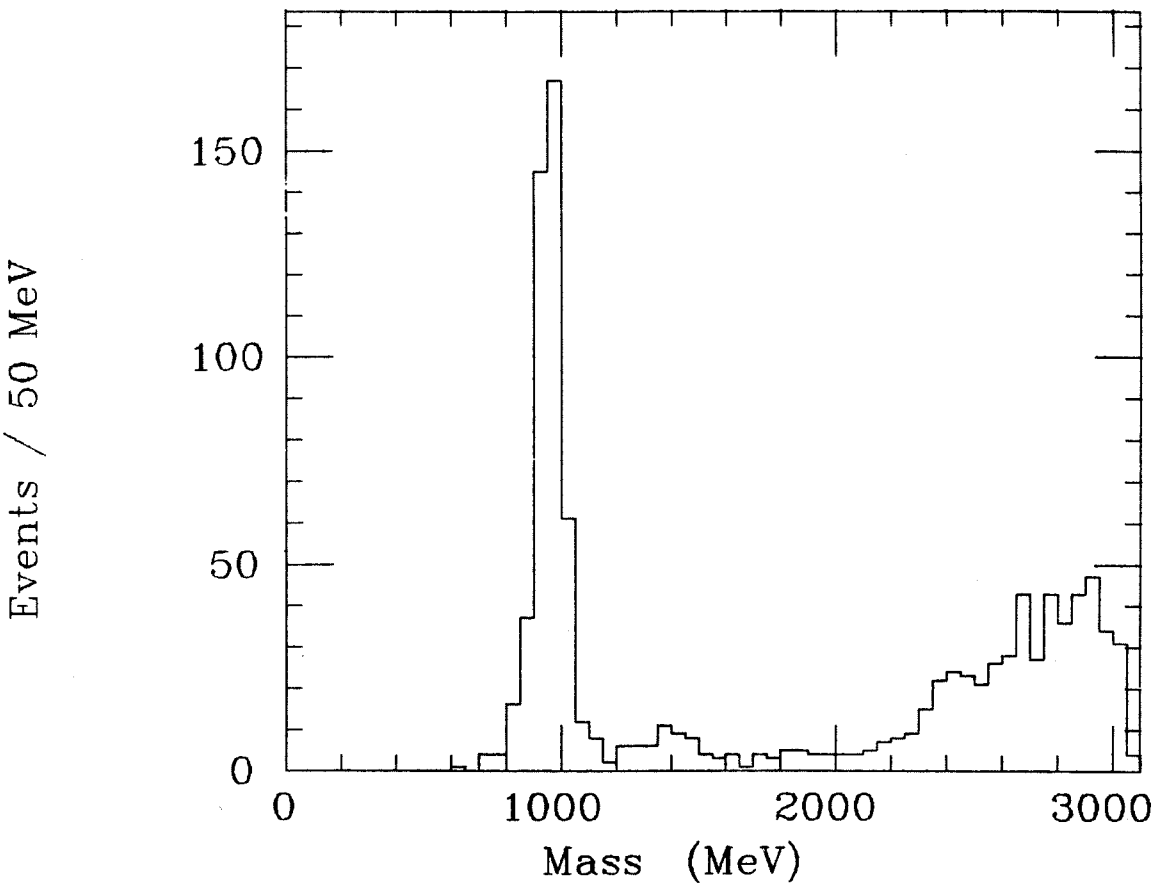

Figure 4.5: $M_{\gamma\pi\pi}$ for events in the ρ band: $570<M_{\pi\pi}<920$ MeV. There are two entries per event.

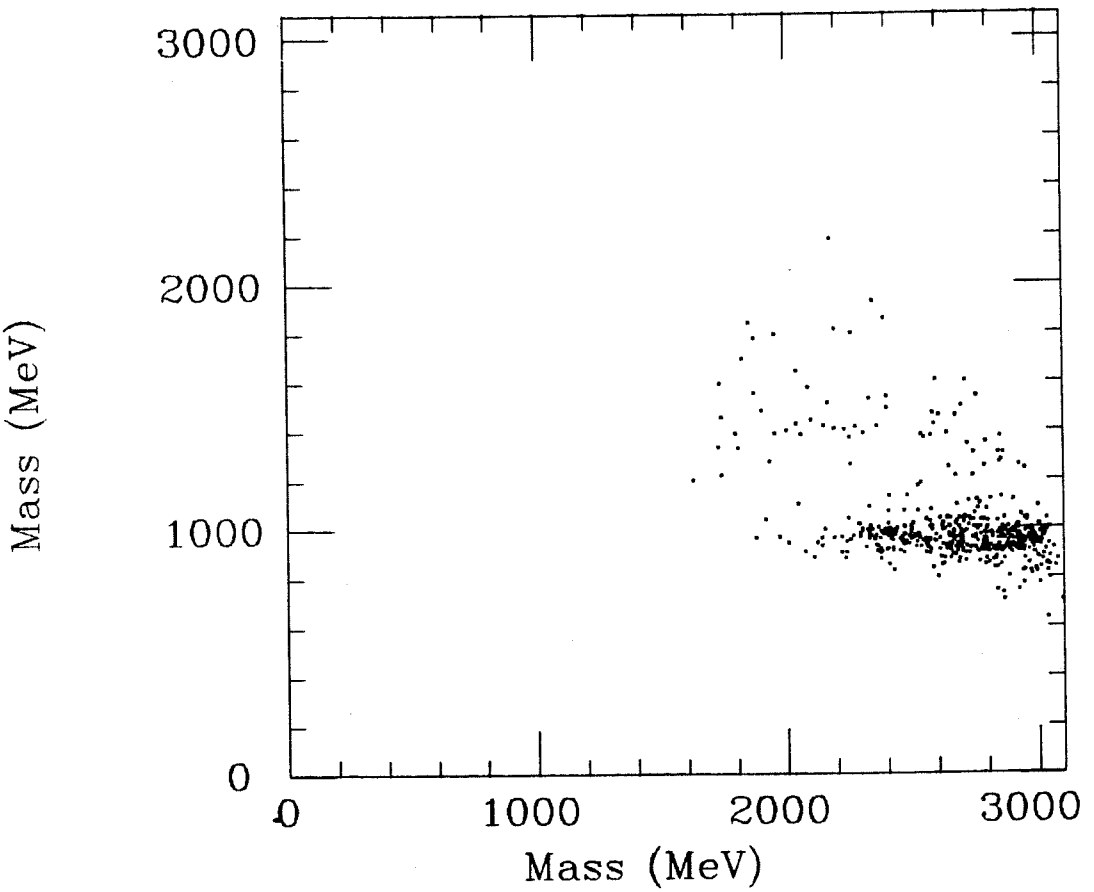

Figure 4.6: $M^{lo}_{\gamma\pi\pi}$ vs $M^{hi}_{\gamma\pi\pi}$ for ρ events.

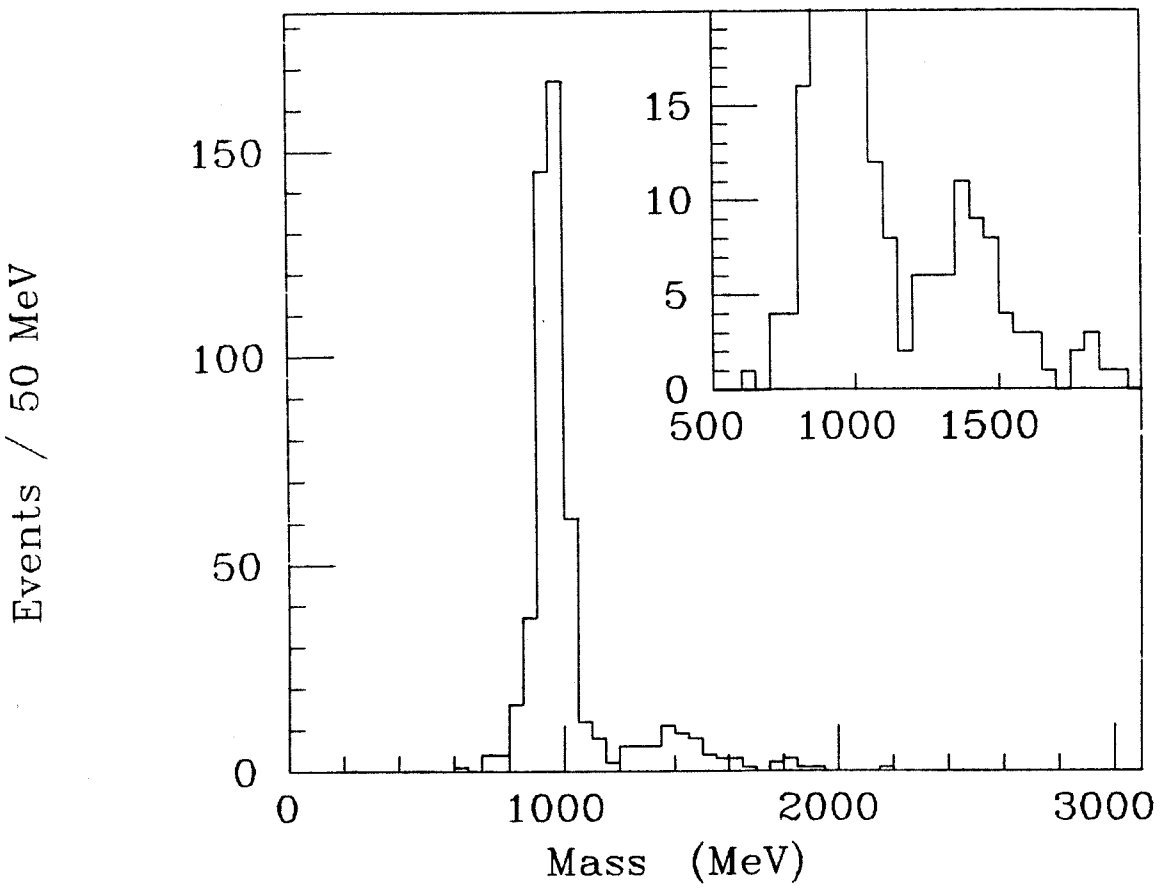

Figure 4.7: $M^{lo}_{\gamma\pi\pi}$ for ρ events.

Based on the theoretical ideas mentioned in the previous section, it is natural to ask whether the higher mass $\gamma\rho$ resonance can be identified with the $\iota(1440)$. Treating the $\gamma\rho$ enhancement as a single peak seems to give results which do not agree well with an ι interpretation. We have fit the entire mass range to a sum of a flat background plus two peaks; the first peak is a Gaussian whose position and width are fixed at 956.8 and 49 MeV, respectively, while the second peak is a relativistic Breit Wigner lineshape folded with the expected resolution for the higher mass signal. Based on a study of Monte Carlo $\iota(1440)\rightarrow\gamma\rho$ decays, the $\gamma\rho$ mass resolution was determined to be 47±11 MeV. (The uncertainty in this resolution will be reflected in the final systematic error.) If we fix the resonance parameters of the high mass peak to the ι values of M=1440 MeV and Γ=55 MeV, we obtain a poor fit with χ^2=30 for 21 degrees of freedom, due mostly to an excess of events near 1250 MeV, as shown in Figure 4.8a. Relaxing the mass and width of the Breit Wigner, a better fit is obtained. The fit, shown in Figure 4.8b, yields a χ^2 of 23 for 19 degrees of freedom. Letting "X" designate the higher mass signal, we find 60±15 events in the X peak, with M_X=1390±25 MeV and $\Gamma_X=185^{+110}_{-60}$ MeV.

Given the limited statistics, the mass resolution of roughly 50 MeV, and the typical hadronic widths of 50-150 MeV for mesons in this mass range, it is of course possible that the observed enhancement is due to more than one state. In this case, it is easier to accommodate an ι signal in the data. For instance, suppose that the radially excited η, the $\eta(1275)$, has a significant decay rate into $\gamma\rho$. Then we can fit the spectrum with an incoherent sum of *three* peaks: one each for the η', the $\eta(1275)$, and the ι. Fixing the positions and widths of these peaks to their established values (the $\eta(1275)$ has Γ=70 MeV), and varying only the amplitude of each contribution, a good fit is obtained with a χ^2 of 23 for 20

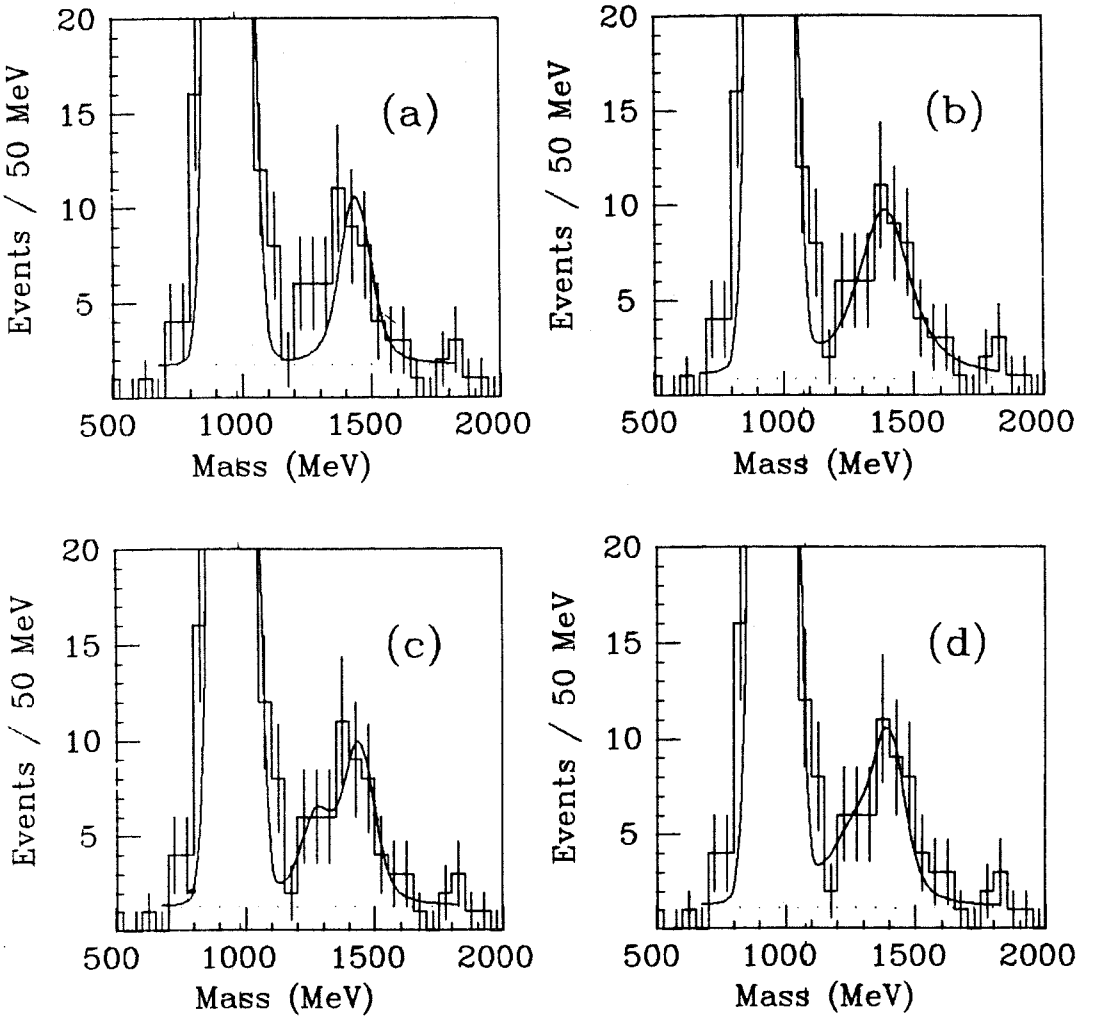

Figure 4.8: Fit results for $M^{lo}_{\gamma\pi\pi}$ spectrum: a) one peak for the high mass enhancement, fixed to ι mass and width; b) resonance parameters released for high mass peak; c) two peaks for the high mass enhancement, with one fixed at the ι and one at the $\eta(1275)$; d) two peaks fixed at ι and $f\,(1270)$.

degrees of freedom, as shown in Figure 4.8c. The ι contributes 29±7 events, while the $\eta(1275)$ contributes 18±7 events. Certainly this should not be construed as evidence for the observation of $\eta(1275)$ decays. The purpose of this last fit is only to show that the interpretation of the $\gamma\rho$ enhancement depends critically on the assumptions one makes regarding the underlying physics in this region. Similar results occur when the $\eta(1275)$ is replaced with the $f(1270)$. Table 4.4 summarizes the results of the various fits. Based on the unconstrained one peak fit, we will refer to the high mass $\gamma\rho$ enhancement as $X(1390)$. However, in light of the previous discussion, this should not be interpreted as a claim that the enhancement is due to one state.

The detection efficiency for this final state was determined by generating Monte Carlo events for the decay sequences $\psi\to\gamma\eta'$, $\eta'\to\gamma\rho$ and $\psi\to\gamma\iota(1440)$, $\iota\to\gamma\rho$. The η' events were generated with the proper angular distribution for a pseudoscalar decay into $\gamma\rho$. Since the spin-parity of the state or states responsible for the high mass $\gamma\rho$ enhancement was not known, several angular distributions were investigated for the ι decays. The efficiency was found to be 12.7±1.1% for the η' and 14.3±1.7% for the ι. These errors represent only the statistical error due to the finite size of the Monte Carlo datasets; systematic uncertainties in the accuracy of the detector simulation (chamber efficiencies, splitoffs) and, for the ι region, in the choice of $\gamma\rho$ spin parity, will be considered later in calculating the final branching fractions. The somewhat lower efficiency for the η' is due to the fact that the low η' mass leads to smaller opening angles among the η' decay products, and thus greater inefficiencies due to the overlap cut $\cos\theta_{ij}<.9$. Based on these efficiencies, we obtain the branching fraction

$$BF(\psi\to\gamma\eta') = (5.0\pm0.5\pm0.6)\times10^{-3}.$$

The η' result agrees within errors with a previous Crystal Ball measurement [4.5], as well as measurements by other groups [4.12]. As this analysis was optimized not for the large η' signal but for the small higher mass signal, more stringent selection criteria were used here than in the previous Crystal Ball η' analysis, leading to larger statistical and systematic errors than in reference [4.5].

For the unconstrained one peak fit to the higher mass signal, we obtain a branching fraction

$$BF(\psi\rightarrow\gamma X(1390))\times BF(X(1390)\rightarrow\gamma\rho) = (1.9\pm0.5\pm0.4)\times10^{-4}.$$

Results for the other fit hypotheses are reported in Table 4.4.

The systematic error for the $X(1390)$ branching fraction includes contributions from several sources. First, there is a 5% uncertainty in the total number of produced ψ events. Variation in the efficiency with different $\gamma\rho$ spin-parity hypotheses contributes a 10% error. Further uncertainty in the detector simulation (chamber efficiencies and splitoff production rates) leads to an additional 10% error. Finally, fluctuation of the number of events in the peak due to details of the fit (fit range, background shape) contributes a 15% systematic error. The various contributions were added in quadrature to obtain the final systematic error.

Table 4.4 Fit Results for $\iota \to \gamma X$, $X \to \gamma\rho$					
FIT MODEL	χ^2/dof	# EVENTS	MASS (MeV)	WIDTH (MeV)	$BF(\psi \to \gamma X) \times BF(X \to \gamma\rho)$
$\iota(1440)$	30/21	32±8	1440 (fixed)	55 (fixed)	$(1.0\pm0.3\pm0.2)\times10^{-4}$
X	23/19	61±15	1390±25	185^{+110}_{-60}	$(1.9\pm0.5\pm0.4)\times10^{-4}$
$\iota(1440)$ + $\eta(1275)$	23/20	29±7 18±6	1440 (fixed) 1275 (fixed)	55 (fixed) 70 (fixed)	$(0.93\pm0.26\pm0.16)\times10^{-4}$ $(0.56\pm0.22\pm0.10)\times10^{-4}$
$\iota(1440)$ + $f(1270)$	23/20	28+−8 26±10	1440 (fixed) 1273 (fixed)	55 (fixed) 179 (fixed)	$(0.88\pm0.28\pm0.15)\times10^{-4}$ $(0.84\pm0.33\pm0.15)\times10^{-4}$

Several cross-checks have been made to test the validity of the $X(1390)$ signal.

1. The signal is not associated with a particular running period. The ψ data for 1978, 1979, and 1980 running periods have been examined separately, and the $X(1390)$ signal appears in each subset. In addition, the strength of the $X(1390)$ signal compared to the η' signal is the same for the three subsets.

2. The signal events are not associated with a particular region of the detector. The high energy photon, the low energy photon, and the charged particles are each distributed smoothly over the available solid angle.

3. The possibility that the $X(1390)$ signal arises from $\psi \to \gamma\eta'$ events in which the primary photon is systematically mismeasured has been ruled out. Since the η' is the dominant structure in the $\gamma\rho$ spectrum, it is natural to suspect that it might be somehow responsible for the $X(1390)$ signal. The difference in the primary photon energy for radiative decays to η' and to $X(1390)$ is 167 MeV. If for some reason high energy photons were occasionally measured with a systematic downward shift of 167 MeV, then the η' events could induce a second signal corresponding to a $\gamma\rho$ mass of 1390 MeV. One

problem with this model is that to account for the observed size of the $X(1390)$ signal, the measurement error would have to occur at roughly a 10% rate. (This is just the ratio of the X and η' signal strengths.) This can be ruled out by the energy spectrum for Bhabha events. Nevertheless, we have tested this model in another way. An η' dataset was created containing all events with 10% or better fit likelihoods for the $\gamma\gamma\pi^+\pi^-$ final state, $M_{\pi\pi}$ in the range 550-950 MeV, and $M_{\gamma\pi\pi}$<1100 MeV. For each of these 693 events, 160 MeV was subtracted from the primary photon energy, and the kinematic fit was reapplied. Now only 9 events fit the $\gamma\gamma\pi^+\pi^-$ hypothesis, and only two of these satisfied the ρ criterion of $M_{\pi\pi}$ to be in the range 620-920 MeV. Thus this mechanism fails to account for the observed $X(1390)$ signal by more than an order of magnitude.

4. Events in the signal region are associated with a clear ρ peak in the $\pi^+\pi^-$ mass. Figure 4.9 shows the $\pi^+\pi^-$ mass spectrum of events with $M_{\gamma\pi\pi}$ between 1200 and 1550 MeV. The peak above 1200 is presumably due to $\psi\rightarrow\gamma f\,(1270)$, $f\rightarrow\pi^+\pi^-$ decays, where one of the charged pions creates a low energy splitoff. In addition, a ρ signal is evident. The ρ cuts used in this analysis are shown in the plot. The verification that the $\pi\pi$ system is indeed a ρ allows us to eliminate an important background source. By C parity, the decay $\psi\rightarrow\gamma\gamma\gamma\rho$ is forbidden. Thus by showing that the X is associated with a ρ, we conclude that it cannot be due to $\gamma\gamma\gamma\rho$ events where one γ is lost.

5. The secondary photon (from the $X(1390)\rightarrow\gamma\rho$ decay) shows a broad distribution of energy. Figure 4.10 shows the fit photon energies E_γ^{lo} vs. E_γ^{hi}. Bands are visible for η' and $X(1390)$ events. The low energy photon for the $X(1390)$ events shows no significant pileup at low energies, as would be expected if

the signal were due to $\gamma\pi\pi$ events with one extra splitoff track.

6. The signal appears even in the raw data. The ρ selection can be made by looking at the recoil mass against the two photons. Selecting events with a recoil mass in the range 550-950 MeV and plotting the photon energies yields the scatterplot of Figure 4.11. The η' and $X(1390)$ bands are still visible. This demonstrates that the signal is not manufactured by the fitting process.

7. The decay $\iota \to K^+K^-\pi^0$, where one of the π^0 decay photons is not observed, has been ruled out as a source for the $X(1390)$ signal. This particular background is worrisome because these events contain a monochromatic photon corresponding to the ι mass. Losing one of the π^0 decay photons would cause the kinematic fit to systematically raise the energies of the other two photons, thereby lowering the observed recoil mass against the primary photon and creating a $\gamma\rho$ peak shifted down from the ι mass, which is exactly what we are observing. 1500 Monte Carlo events were generated for the decay sequence $\psi \to \gamma\iota$, $\iota \to K^+K^-\pi^0$, corresponding to the expected number based on the Crystal Ball measurement of this mode. Of these, 101 events satisfied the selection cuts and were fit to the $\gamma\gamma\pi^+\pi^-$ hypothesis. No events had fits with a fit likelihood greater than 10%.

8. There is no contamination of the signal region by $\gamma\gamma K^+K^-$ events. Because the Crystal Ball has no explicit particle identification, charged K/π separation can only be achieved through kinematically constrained fits. In some kinematic regions, events with two charged particles will be well fit by both the $\pi^+\pi^-$ and the K^+K^- hypothesis. Other kinematic regions discriminate well between the two hypotheses. (Although the exact quantitative nature of this ability to discriminate between $\pi^+\pi^-$ and K^+K^- events is quite

complicated, it is clear that when both charged particles have momentum much larger than the kaon mass, the discrimination will be poor, since changing the mass of the charged particles from m_π to m_K will not have a large effect on their energies. Thus energy-momentum constraints can be satisfied for both hypotheses.) The events with good $\gamma\gamma\pi^+\pi^-$ fits were also fit to the hypothesis $\psi\to\gamma\gamma K^+K^-$. No events with $\pi^+\pi^-$ masses in the ρ band, 570-920 MeV, satisfied the $\gamma\gamma K^+K^-$ hypothesis with a 10% or better fit likelihood. Thus in the kinematic region of interest, where the two pions form a ρ, there appears to be excellent kinematic separation between $\pi^+\pi^-$ and K^+K^- final states.

9. Since this was the first ψ analysis carried out using the VAX 11/780 computer system, as well as the first analysis using the PIFIT ψ data, one final concern was that there might be some error in the long analysis chain which was corrupting the data buffers. The entire sequence from the initial production analysis through conversion to compressed output formats, hadron selection, PIFIT, as well as I/O on both IBM and VAX systems, was checked by comparing the data buffer of each signal event with the buffer for that event after the initial production analysis. No changes had occurred to any information in the data buffers for any of these events.

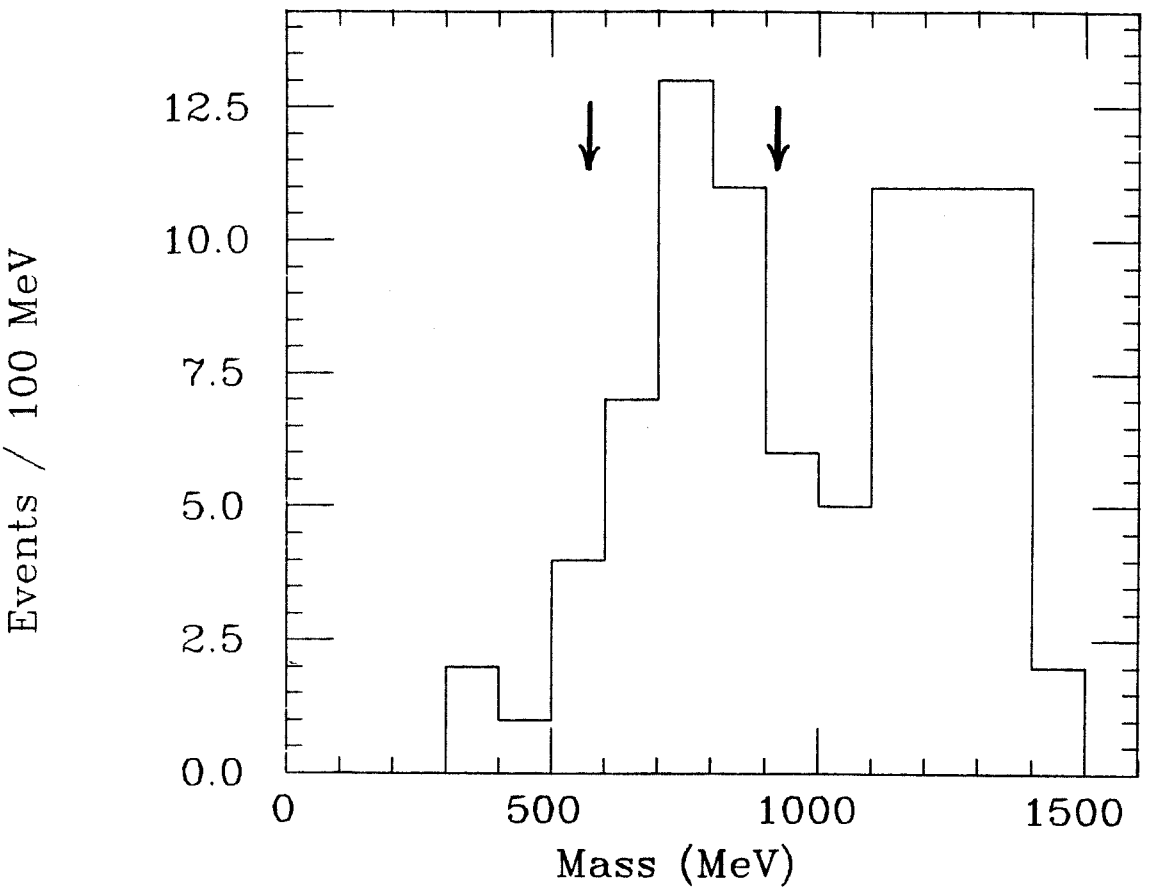

Figure 4.9: The $\pi^+\pi^-$ mass distribution for events with $M_{\gamma\pi\pi}$ in the range 1200-1550 MeV. In addition to the high mass peak, which is presumably due to splitoff events, there is a clear ρ signal. The mass range used to define ρ events in this analysis is indicated.

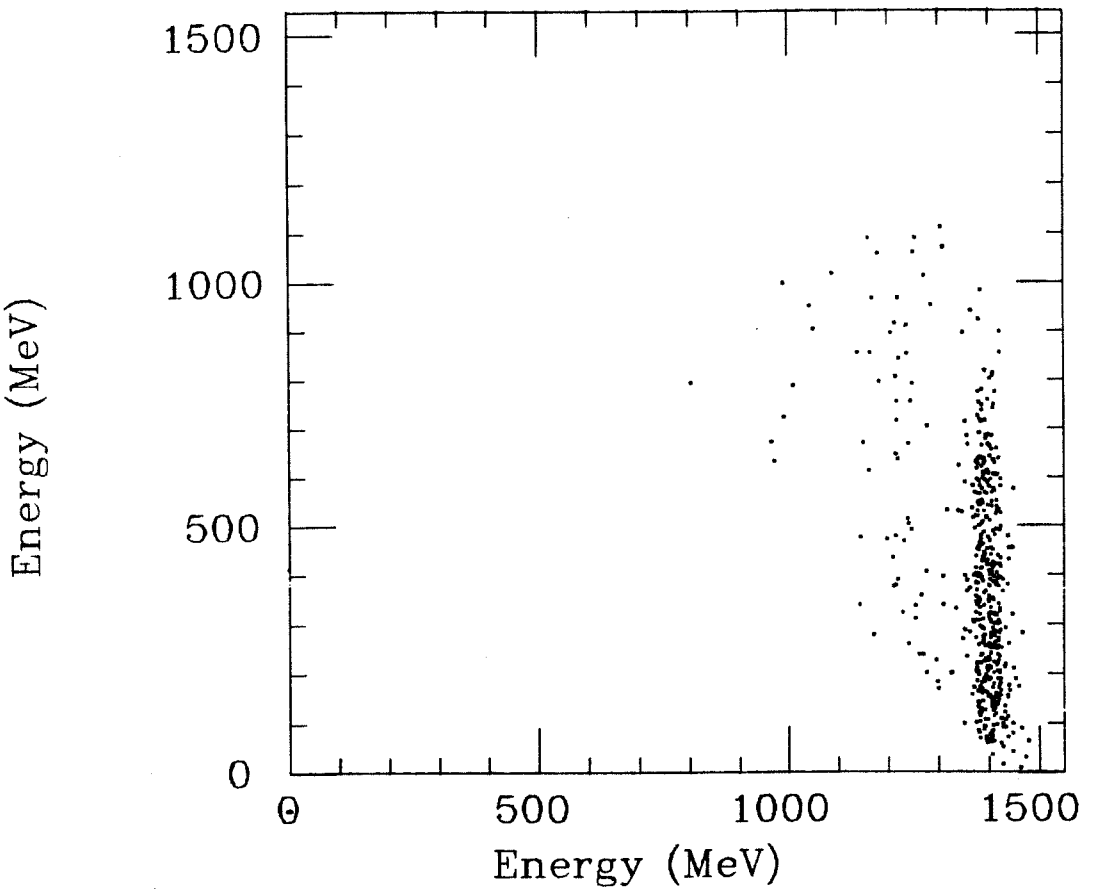

Figure 4.10: E_γ^{lo} vs. E_γ^{hi} for kinematically fit photon energies. Two vertical bands are visible, corresponding to the monochromatic high energy photons in the decays $\psi \to \gamma\eta'$ and $\psi \to \gamma X$. The X events show a broad distribution of secondary photon energies.

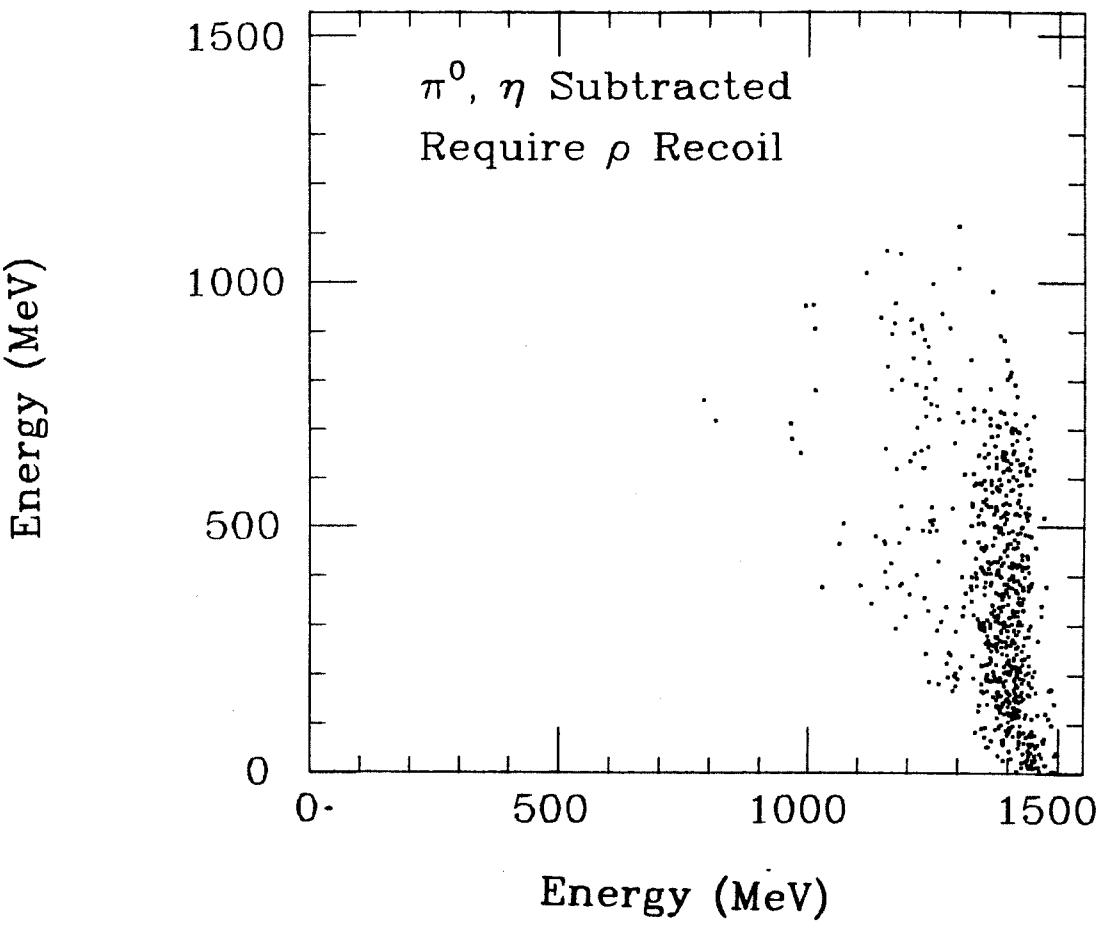

Figure 4.11: E_γ^{lo} vs. E_γ^{hi} for unfit photons. π^0 and η events have been subtracted based on the raw $\gamma\gamma$ mass, and ρ events have been selected based on the recoil mass opposite the two photons, calculated using the raw photon four-momenta. Both the η' and X signals are visible.

4.4 Angular Distributions

While the validity of the $\gamma\rho$ enhancement seems secure, its interpretation as evidence for radiative ι decays seems much less certain. The signal appears to be broader and peaked at somewhat lower masses than the ι, with both of these parameters over 1σ from the Crystal Ball ι values. On the other hand, we have seen how a combination of two states, such as the ι and $\eta(1275)$, can fit the data well. Further information as to the nature of the enhancement is clearly needed. A study of the angular distributions of the particles involved in the decay can provide information concerning the spin and parity of the state or states responsible for the enhancement. Unfortunately, given the limited number of events in the high mass $\gamma\rho$ enhancement, we will not be able to make a clear J^P assignment; however, examination of the relevant decay angular distributions will allow us to make some qualitative observations on the enhancement, and perhaps point the way for future experiments with greater statistics.

Figure 4.12 labels the relevant decay angles for the decay sequence

$$\psi \to \gamma X \hookrightarrow \gamma\rho^0 \hookrightarrow \pi^+\pi^- \ .$$

The angles are measured in the center of mass of each two-body decay. For J_X=1 or 2, there are respectively 4 or 6 independent helicity amplitudes which must be summed over, allowing a great deal of variation in the angular distribution of the final state particles. For scalar or pseudoscalar X, however, the angular distribution is completely determined and takes the form

$$\frac{d\sigma(\theta_{\gamma_1},\theta_{\gamma_2},\theta_\pi)}{d\cos\theta_{\gamma_1}\, d\cos\theta_{\gamma_2}\, d\cos\theta_\pi} = (1+\cos^2\theta_{\gamma_1})\sin^2\theta_\pi .$$

There is no dependence on the azimuthal angles for the spin zero case. The $\sin^2\theta_\pi$ dependence is a manifestation of the ρ polarization: in the decay of a spin

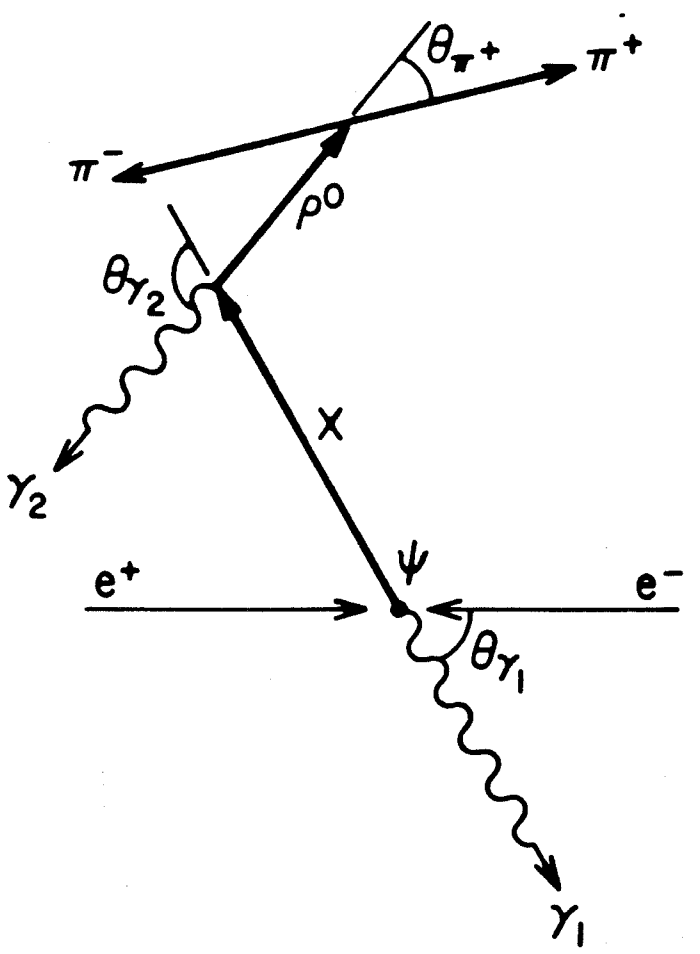

Figure 4.12: Definition of the decay angles θ_{γ_1}, θ_{γ_2}, and θ_{π}, for the decay $\psi \to \gamma X$, $X \to \gamma\rho$.

0 particle into $\gamma\rho$, the ρ helicity must equal the γ helicity, and thus the ρ will never have helicity 0. If all three ρ helicity states were populated equally, the decay pions would have a flat distribution in $\cos\theta_\pi$.

The distribution of $\cos\theta_{\gamma_1}$, an angle measured in the laboratory frame, is badly distorted due to detector acceptance. As $|\cos\theta_{\gamma_1}|$ approaches 0.9, the probability of one of the particles in the recoiling $\gamma\pi^+\pi^-$ system to fail the fiducial cut $|\cos\theta_i|<.9$ increases. Also, the charged particle tagging efficiency falls off for large values of $|\cos\theta_i|$. The distributions with respect to the other two angles, $\cos\theta_{\gamma_2}$ and $\cos\theta_\pi$, are much less biased by efficiency problems, as these angles are defined in transformed reference frames, where the actual transformation varies from event to event, thus smearing out any effects due to the detector geometry.

We have defined three classes of events for examination of these angular distributions, corresponding to three regions of $M^{lo}_{\gamma\pi\pi}$ in Figure 4.8. The η' sample will be defined by the requirement $900<M^{lo}_{\gamma\pi\pi}<1000$ MeV. This will serve as a clean sample of pseudoscalars to which the higher mass events can be compared. The actual $X(1390)$ enhancement will be split into two regions, X_{lo} and X_{hi}, to provide a further test of whether the signal might be due to two states. Events in the mass range 1200-1350 MeV will be assigned to X_{lo}, while X_{hi} events will be those in the range 1350-1550 MeV.

Figure 4.13a shows the distribution of $\cos\theta_{\gamma_2}$ for the three samples. For a spin zero decay into $\gamma\rho$, this distribution should be flat. This distribution also provides an independent check of the amount of residual background due to events with one real photon and one low energy splitoff shower. Low energy photons in the decay $X\rightarrow\gamma\rho$ correspond to values of $\cos\theta_{\gamma_2}$ near -1, or in other words to decays where the second photon is emitted in the backwards direction with

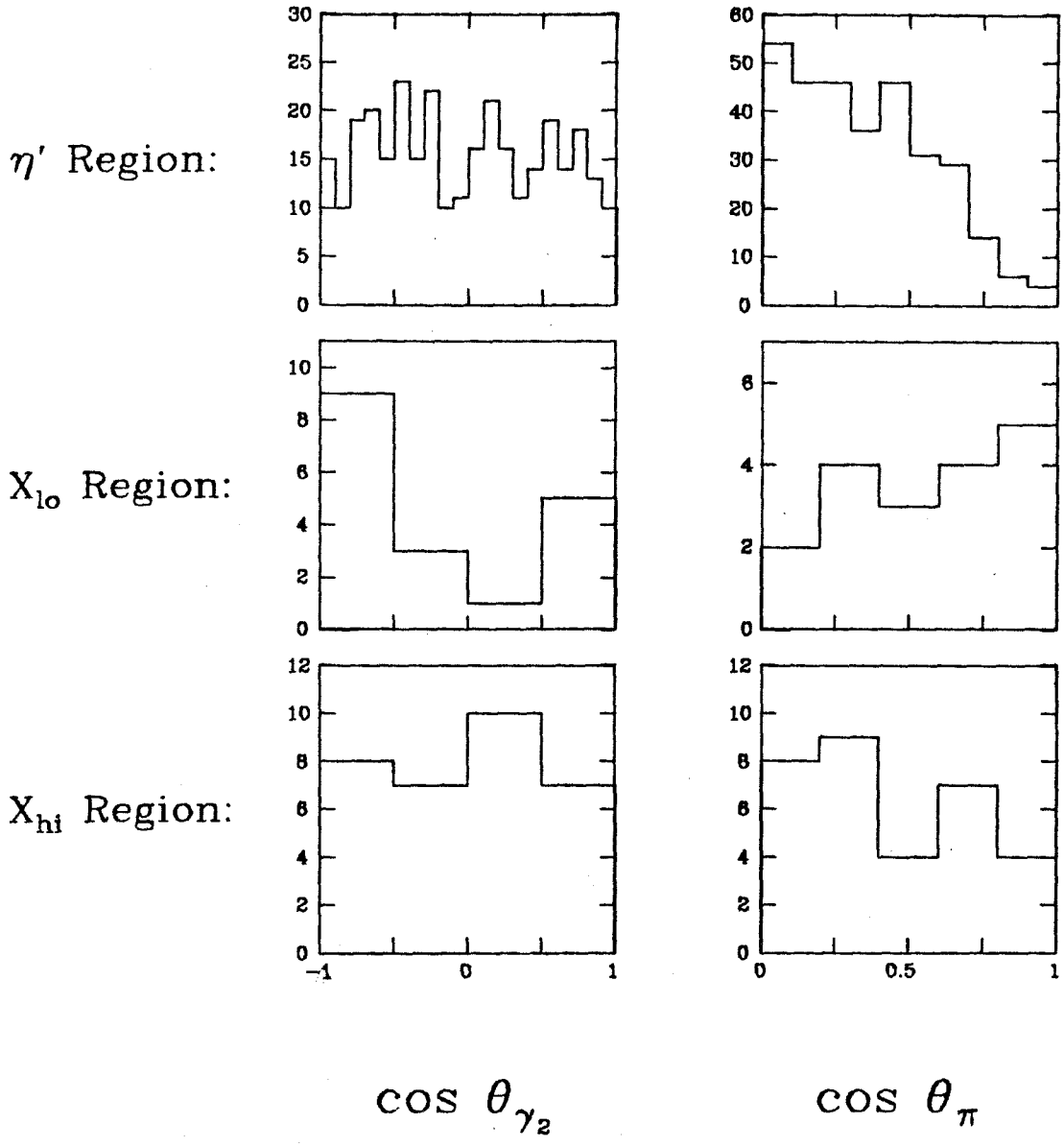

Figure 4.13: Angular distributions for η', X_{lo}, and X_{hi} events: a) $\cos\theta_{\gamma_2}$; b) $\cos\theta_{\pi}$.

respect to the X direction of motion. Parity conservation demands that the distribution of $\cos\theta_{\gamma_2}$ be symmetric about zero for real X decays, so an excess of events at $\cos\theta_{\gamma_2}$ near -1 indicates the presence of background events.

The η' events exhibit a very flat distribution, as expected for a spin zero particle. A flat distribution gives a χ^2 of 22.4 for 19 degrees of freedom. The X_{hi} distribution also appears flat, although the statistics are limited. To test the hypothesis that the distribution is flat for such a limited number of events, we have formed a likelihood function L using Poisson statistics for the bin contents. Let L_0 be the value of the likelihood function for a flat distribution, and L_1 be the value of the likelihood function for the case where the predicted bin contents are defined to be the observed contents. Then it can be shown [4.13] that the test statistic $-2\log(\frac{L_0}{L_1})$ assumes a χ^2 distribution, where the number of degrees of freedom is one less than the number of bins. Thus for the case of X_{hi}, a flat distribution yields an effective χ^2 of .75 for 3 degrees of freedom. In addition, no forward-backward asymmetry is observed, indicating the absence of residual background from splitoff events. The distribution of X_{lo} events, however, does not appear flat. For these events, a flat distribution gives an effective χ^2 of 8.1 for 3 degrees of freedom, corresponding to less than a 5% χ^2 probability.

Given this poor fit, we can consider two alternatives. First, the events in X_{lo} could be associated with decays of a particle with non-zero spin. Fitting the observed distribution to the form $1 + \alpha\cos^2\theta_{\gamma_2}$ yields an effective χ^2 of 2.2 for 2 degrees of freedom, with $\alpha = 8.6$. The one sigma (68% confidence level) limit restricts α to be greater than 2.2. (There is no upper bound; $\alpha = \infty$ corresponds to all the events in the outside two bins, none in the middle two.)

The other alternative explanation for the shape of the X_{lo} distribution is that some residual splitoff events are populating the lowest bin. To examine this

hypothesis, we have fit the X_{lo} distribution to a sum of a flat distribution plus an extra n events in the lowest bin. The best fit gave an effective χ^2 of 2.9 for 2 degrees of freedom, with $n=6.0^{+3.0}_{-2.8}$, where we have indicated the one sigma limits on n.

Thus both alternatives can provide good explanations for the observed non-flat distribution of $\cos\theta_{\gamma_2}$ for the X_{lo} events. Examination of the events in X_{lo} with values of $\cos\theta_{\gamma_2}$ in the range -1.0 to -0.5 finds no obvious problems with the low energy photons, such as peculiar patterns or close proximity to hadrons, which might be indicative of residual splitoff background events. Hence we can only conclude from the $\cos\theta_{\gamma_2}$ distribution that either the entire X region is consistent with a flat distribution, with some residual background contamination in the X_{lo} region, or that only the X_{hi} region is consistent with flatness, and that the X_{lo} events are due to the decay of a state with non-zero spin.

Turning next to the ρ helicity, Figure 4.13b shows the distribution of $\cos\theta_\pi$ for the three classes of events η', X_{hi}, and X_{lo}. Fitting the η' events to the form $1+\alpha\cos^2\theta_\pi$, we obtain the result $\alpha = -1.08\pm0.04$, where only the statistical error of the fit is included. This agrees well with the value of -1 predicted for the decay of a spinless particle to $\gamma\rho$. It also demonstrates that there are no large systematic distortions in this distribution due to dependence of the overall detection efficiency on $\cos\theta_\pi$. For the X_{lo} and X_{hi} events, we have once again formed an effective χ^2 from the statistic $-2\log(\frac{L_0}{L_1})$, where L_0 now corresponds to the likelihood function for a $1-\cos^2\theta_\pi$ distribution, corresponding to the expected form for $J^P(X)=0^-$. The X_{lo} events yield a χ^2 of 11.7 for 4 degrees of freedom, corresponding to only a 2% χ^2 probability, while the X_{hi} events give a reasonable χ^2 of 4.75 for 4 degrees of freedom. Thus, while the X_{hi} events appear compatible with the expected spin zero behavior, the X_{lo} events seem to have a

distribution incompatible with J_X=0.

Combining the information from both distributions, we find that the X_{hi} events are consistent with a pseudoscalar interpretation, with a total χ^2 of 5.5 for 7 degrees of freedom. The X_{lo} events, however, are clearly inconsistent with such an interpretation, yielding a total χ^2 of 19.8 for 7 degrees of freedom, corresponding to less than a 1% probability. However, we are unable to say whether the X_{lo} events are due to residual contamination of events with splitoff tracks, or are due to the decays of a state with non-zero spin.

4.5 Observations by Other Experiments

Two other experiments have reported results on the process $\psi \to \gamma\gamma\rho$ for $\gamma\rho$ masses near the ι. The DM2 detector, located at the DCI storage ring, has collected data for roughly 10^6 ψ decays using a large magnetic spectrometer with shower counters for photon detection. They have searched for the decay sequence $\psi \to \gamma\iota \to \gamma\gamma\rho$ [4.14]. Figure 4.14 shows their distribution of $M_{\pi\pi}$ vs $M^{lo}_{\gamma\pi\pi}$, along with ι and sideband regions which they define in order to make a background subtraction. Their ι region corresponds to $550 < M_{\pi\pi} < 1000$ MeV and $1365 < M^{lo}_{\gamma\pi\pi} < 1515$ MeV. Based on the background subtraction, they report no evidence for $\iota \to \gamma\rho$ decays, and state an upper limit

$$BF(\psi \to \gamma\iota) \times BF(\iota \to \gamma\rho) < 5 \times 10^{-5} \quad (95\% C.L.).$$

This result is incompatible with the Crystal Ball observation. However, it should be noted that the $\gamma\rho$ enhancement observed by the Crystal Ball peaks at a mass near 1400 MeV, and is much broader than the ι observed in $K\bar{K}\pi$ decays. The choice of signal and background regions used by the DM2 collaboration for their background subtraction was based on an ι mass and width of 1440 and 55 MeV

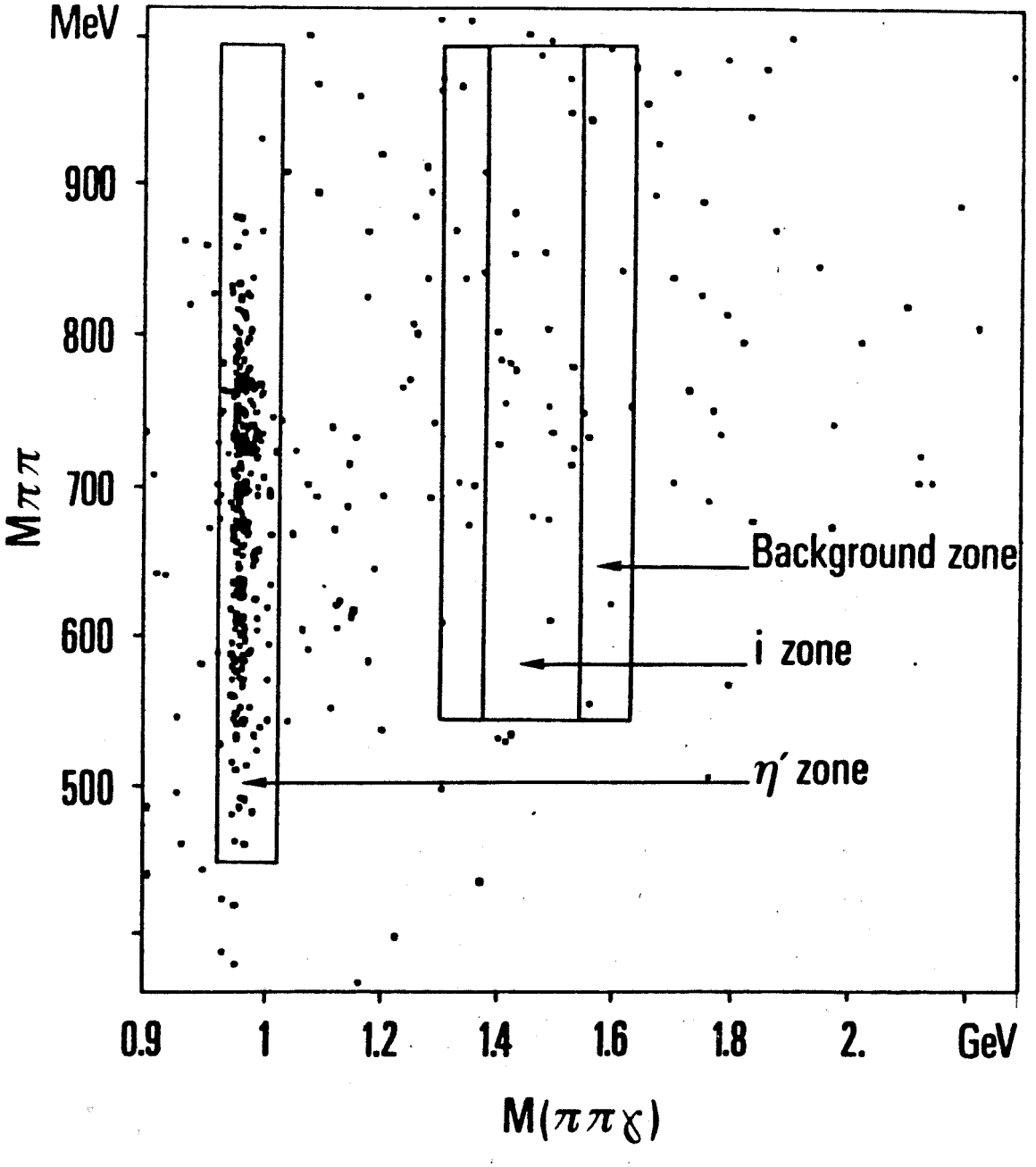

Figure 4.14: DM2 results for the $\gamma\gamma\pi^+\pi^-$ final state, showing $M_{\pi\pi}$ vs. $M^{lo}_{\gamma\pi\pi}$. The regions used to define ι and sideband events are indicated.

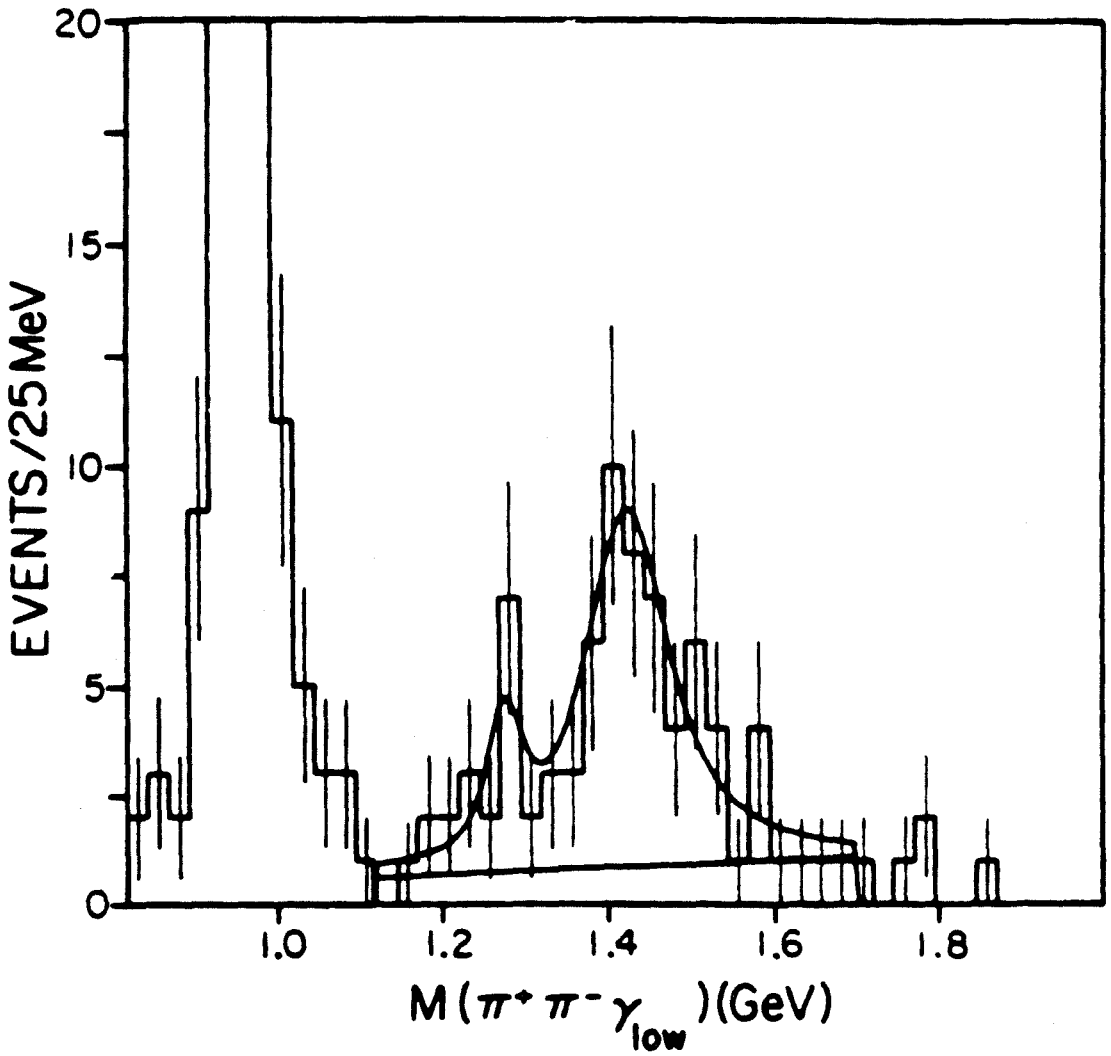

Figure 4.15: The $\gamma\rho$ mass spectrum from the Mark III experiment.

respectively. This could bias their results.

The Mark III collaboration has also reported results for the $\gamma\gamma\rho$ final state, based on an analysis of 2.7×10^6 produced ψ events [4.3]. Figure 4.15 shows their plot of $M^{lo}_{\gamma\pi\pi}$ for $\gamma\gamma\pi^+\pi^-$ events which satisfy a ρ cut on the $\pi\pi$ mass. They observe a structure near 1400 MeV remarkably similar to the Crystal Ball result. Fitting to two Breit-Wigner resonances, one fixed at the $\eta(1275)$ mass and width, they find

$$BF(\psi\to\gamma\eta(1275))\times BF(\eta(1275)\to\gamma\rho) < 1.9\times10^{-5} \quad (90\%\ C.L.).$$

and for the upper peak:

$$M_X = 1425\pm14 \text{ MeV}$$

$$\Gamma_X = 112\pm57 \text{ MeV}$$

$$BF(\psi\to\gamma X)\times BF(X\to\gamma\rho) = (7.4\pm2.2\pm1.3)\times10^{-5}.$$

While the Mark III seems to be seeing fewer events in the $\eta(1275)$ region, the result for the ι region agrees well with the Crystal Ball results for a two peak fit to the observed enhancement. It should be recalled that the Mark III reports an ι mass of 1460±10 MeV and width of 97±25 MeV in $K\bar{K}\pi$ decays.

4.6 Conclusions

An examination of the $\gamma\rho$ mass spectrum in the decay $\psi\to\gamma\gamma\rho$ has shown evidence for new structure in the region of 1400 MeV. The large η' signal in this channel has been used to check the overall mass scale, resolution, and detection efficiency. The new enhancement has been fit to a single relativistic Breit-Wigner shape, with the results

$$M_X = 1390 \pm 25 \text{ MeV}$$

$$\Gamma_X = 185^{+110}_{-80} \text{ MeV}$$

$$BF(\psi \to \gamma X) \times BF(X \to \gamma\rho) = (1.9 \pm 0.5 \pm 0.4) \times 10^{-4}.$$

We have also considered the possibility that more than one state is responsible for the enhancement. A combination of $\iota(1440)$ plus $f(1270)$ or of $\iota(1440)$ plus $\eta(1275)$ fit the observed spectrum well, with roughly 1/2 to 2/3 of the observed enhancement being attributed to the $\iota(1440)$.

A large number of cross-checks have been made to ensure that the signal is genuine, and not an artifact of the analysis. The fact that the signal appears even in the raw data, and that the signal is associated with a clear ρ signal, are two of the more compelling pieces of evidence supporting the validity of the signal.

Finally, we have examined the angular distribution of events in the enhancement, and compared to the angular distribution for η' events. The limited statistics associated with the new enhancement do not allow any definite conclusions to be drawn as to the spin and parity of the $\gamma\rho$ state. However, the upper part of the enhancement appears to fit a pseudoscalar interpretation much better than the lower part. This could indicate a residual background of splitoff events contaminating the lower part of the spectrum, or the presence of two distinct states contributing to the enhancement. In either case, an interpretation of the upper part of the enhancement as an $\iota(1440)$ signal becomes a plausible hypothesis.

Chapter IV References

[4.1] D.L. Scharre *et al.*, Phys. Lett. B97, 329 (1980).

[4.2] C. Edwards *et al.*, Phys. Rev. Lett. 49, 259 (1982).

[4.3] W. Toki *et al.*, "MARK III Results from SPEAR," SLAC PUB 3262, 1983.

[4.4] R. Partridge *et al.*, Phys. Rev. Lett. 45, 1150 (1980).

[4.5] K. Koenigsmann, XVIIth Rencontre de Moriond; Workshop on New Spectroscopy, Les Arcs, France, 1982; also SLAC-PUB-2910 (1980).

[4.6] K. Milton, W. Palmer, and S. Pinsky; XVIIth Rencontre de Moriond; Workshop on New Spectroscopy, Les Arcs, France, 1982.

[4.7] C. Carlson and T. Hansson, Nucl. Phys. B199, 441 (1982).

[4.8] S. Iwao, Lettere al Nuovo Cimento, 35, 209 (1982).

[4.9] K. Senba and M. Tanimoto, Lettere al Nuovo Cimento, 35, 295 (1982).

[4.10] W. Palmer and S. Pinsky, Phys. Rev. D27, 2219 (1983).

[4.11] Particle Data Group, Phys. Lett. 111B, 1982.

[4.12] D.L. Scharre, SLAC-PUB-2321,1979; R. Brandelik *et al.*, Zeit. Phys. C1, 233 (1979); W. Bartel *et al.*, Phys. Lett. 66B, 489 (1976).

[4.13] W.T. Eadie, D. Drijard, F.E. James, M. Roos, and B. Sadoulet, *Statistical Methods in Experimental Physics*, New York, American Elsevier, 1971.

[4.14] J. Augustin *et al.*, International Symposium on Lepton and Photon Interactions at High Energies, Cornell University, August 4-9, 1983.

Chapter V

$\psi \to \gamma\rho^+\rho^-$

5.1 Introduction

The first results on the decay $\psi \to \gamma\rho\rho$ were reported by the Mark II experiment in 1981 [5.1]. Their final $\rho\rho$ mass spectrum exhibits a concentration of events with masses in the range 1.4-2.0 GeV, as shown in Figure 5.1. The observed number of events corresponds to a large radiative ψ decay branching fraction: for events with $M_{\rho\rho} < 2.0$ GeV, they find $BF(\psi \to \gamma\rho^0\rho^0) = (1.25 \pm 0.35 \pm 0.40) \times 10^{-3}$. Fitting the observed enhancement to a Breit-Wigner resonance shape, they obtain a mass of 1650±50 MeV and a width of 200±100 MeV.

These resonance parameters are similar to the values obtained for the θ, a resonance observed by the Crystal Ball in $\gamma\eta\eta$ decays [5.2], and by the Mark II and Mark III experiments in γK^+K^- decays [5.3]. Combining the results of the three experiments, the θ mass and width are found to be 1700±15 MeV and 140±20 MeV respectively. Given this level of agreement, it is interesting to explore the possibility that the $\rho\rho$ enhancement observed by the Mark II experiment might indeed be the θ.

Several facts indicate that the Crystal Ball could hope to improve upon the Mark II result for the $\gamma\rho\rho$ final state, and thereby test whether the $\rho\rho$ enhancement is related to the θ. The Crystal Ball dataset of 2.17×10^6 ψ decays is over three times larger than the Mark II ψ sample of 650,000 events. Also, the Crystal Ball is sensitive to the $\rho^+\rho^-$ decay mode, while the Mark II examined the $\rho^0\rho^0$ mode. If the $\rho\rho$ system is in an isoscalar state, the $\rho^+\rho^-$ mode is enhanced by a

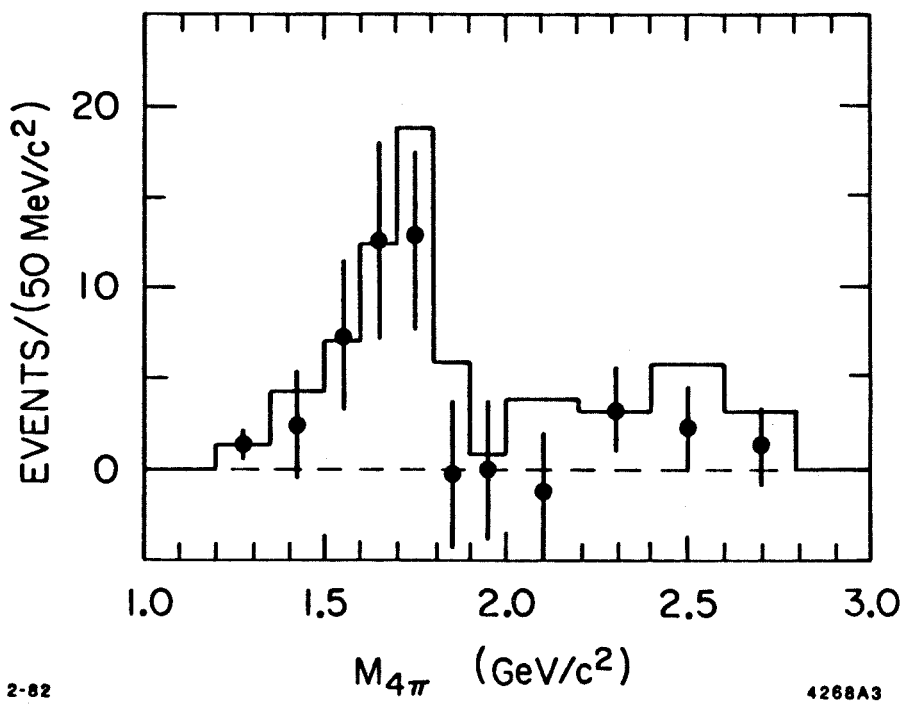

Figure 5.1: The $\rho^0\rho^0$ mass spectrum obtained by the Mark II experiment in a study of $\psi\to\gamma\pi^+\pi^-\pi^+\pi^-$ decays. The histogram and data points represent two different methods of extracting the $\rho\rho$ signal.

factor of two with respect to the $\rho^0\rho^0$ mode. Finally, the poor efficiency of the Mark II detector for low energy photons led to a large background of $\pi^0\pi^+\pi^-\pi^+\pi^-$ events contaminating the $\gamma\pi^+\pi^-\pi^+\pi^-$ event sample. The Crystal Ball's excellent efficiency for low energy photons and nearly complete solid angle coverage should help to alleviate the background from 5π decays. A better measurement of the mass and width of the $\rho\rho$ enhancement is clearly one way in which the θ identification can be tested.

An analysis of the spin and parity of the $\rho\rho$ system is especially important in determining if it should be identified with the θ. The θ is required to have J even and $P=+1$ based on its decay to a pair of identical pseudoscalars, $\theta\rightarrow\eta\eta$. An analysis of the $\gamma\eta\eta$ final state by the Crystal Ball [5.2] found $J^P=2^+$ preferred over 0^+ at the 95% confidence level. However, this analysis did not take into account possible contamination of the $\eta\eta$ spectrum by f' decays. With poorer statistics and higher backgrounds, the Mark II experiment found the 2^+ hypothesis preferred over the 0^+ at a 78% confidence level for their K^+K^- signal. Thus the θ parity is firmly established to be positive, and the spin is required to be even, but the assignment to $J=0$ or $J=2$ is not yet clearly determined. The limited number of events and large 5π background in the Mark II $\rho\rho$ signal prevented them from performing a spin-parity analysis of the $\rho\rho$ system.

In this chapter, we will present the results of an analysis of the $\gamma\pi^+\pi^-\pi^0\pi^0$ final state. After describing the event selection, we will use a simple sideband subtraction to extract the $\rho\rho$ signal and show the presence of a $\rho\rho$ enhancement near 1700 MeV. Finally, we will examine the angular distributions of the final state particles for $\rho\rho$ events with $M_{\rho\rho}$ near 1700 MeV, in an effort to determine the spin and parity of the $\rho\rho$ enhancement.

5.2 Experimental Analysis of the $\gamma\pi^+\pi^-\pi^0\pi^0$ Final State

The first step in the analysis was the selection of events from the hadron-selected ψ dataset with the proper multiplicity. The PIFIT analysis was utilized to recover events in which one or both π^0's were merged. Candidate events were required to have either

a.) Two charged tracks and five photon tracks, or,

b.) Two charged tracks, three photon tracks, and one PIFIT merged π^0 track, or,

c.) Two charged tracks, one photon track, and two PIFIT merged π^0 tracks.

All tracks were required to satisfy $|\cos\theta_{i-beam}|<0.9$, where θ_{i-beam} is the angle of a track with respect to the e^+ beam direction. Events with closely overlapping tracks were removed by demanding that the opening angle between all pairs of tracks i and j satisfy $\cos\theta_{ij}<.95$. All photon tracks were required to have patterns of energy distribution in the crystals consistent with electromagnetic showers. This helped to remove events in which one of the neutral tracks was actually a charged hadronic particle which was not identified as charged by the tracking chambers. Some events with splitoff tracks were also found and removed based on their shower patterns. Finally, the SPLIT algorithm was applied to the remaining events to further eliminate events with splitoff tracks.

Of the 8293 events which passed this initial event selection, 439 contained two merged PIFIT π^0's, 3321 had one merged π^0, and the remaining 4533 had no merged π^0's. The $\gamma\gamma$ mass spectrum for events with one merged π^0, shown in Figure 5.2, displays a prominent π^0 peak. There are three entries per event in this plot. For events with five photon tracks and no merged π^0's, we plot in Figure 5.3 the distribution of $M_{\gamma\gamma}$ vs. $M_{\gamma\gamma}$, with fifteen entries per event. Once again we see strong evidence for events with two π^0's.

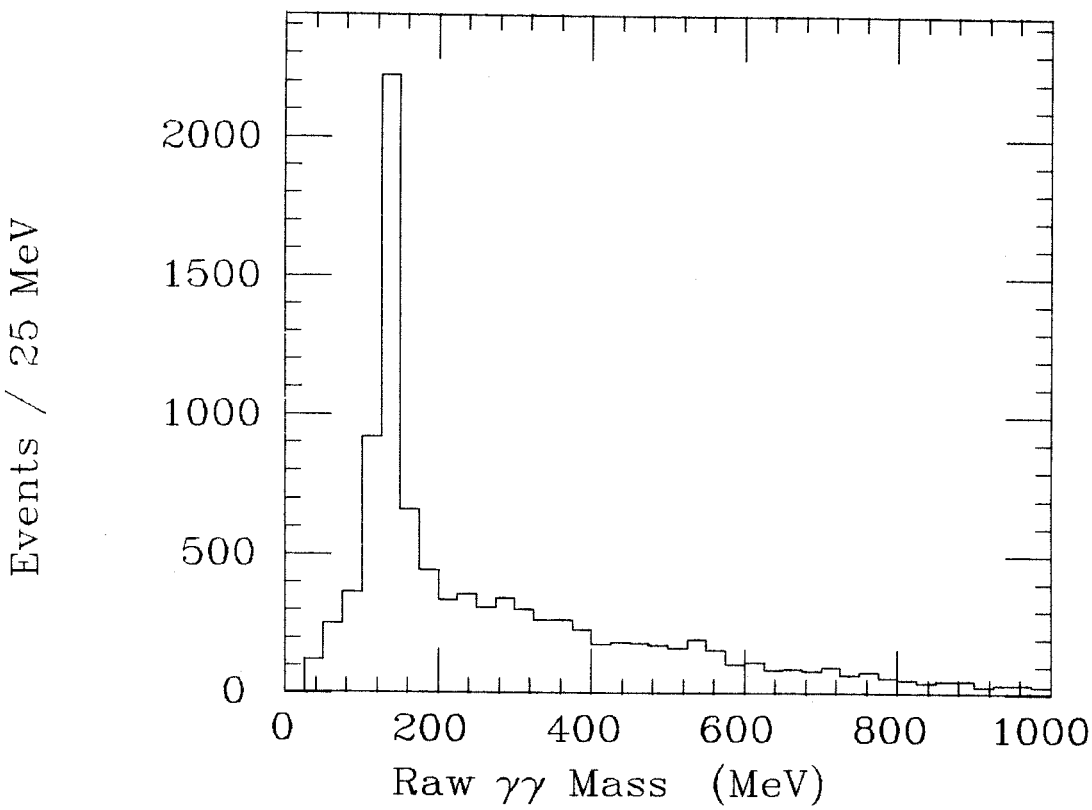

Figure 5.2: $\gamma\gamma$ masses for events with two charged tracks, one merged π^0 track, and three γ's. There are three entries per event.

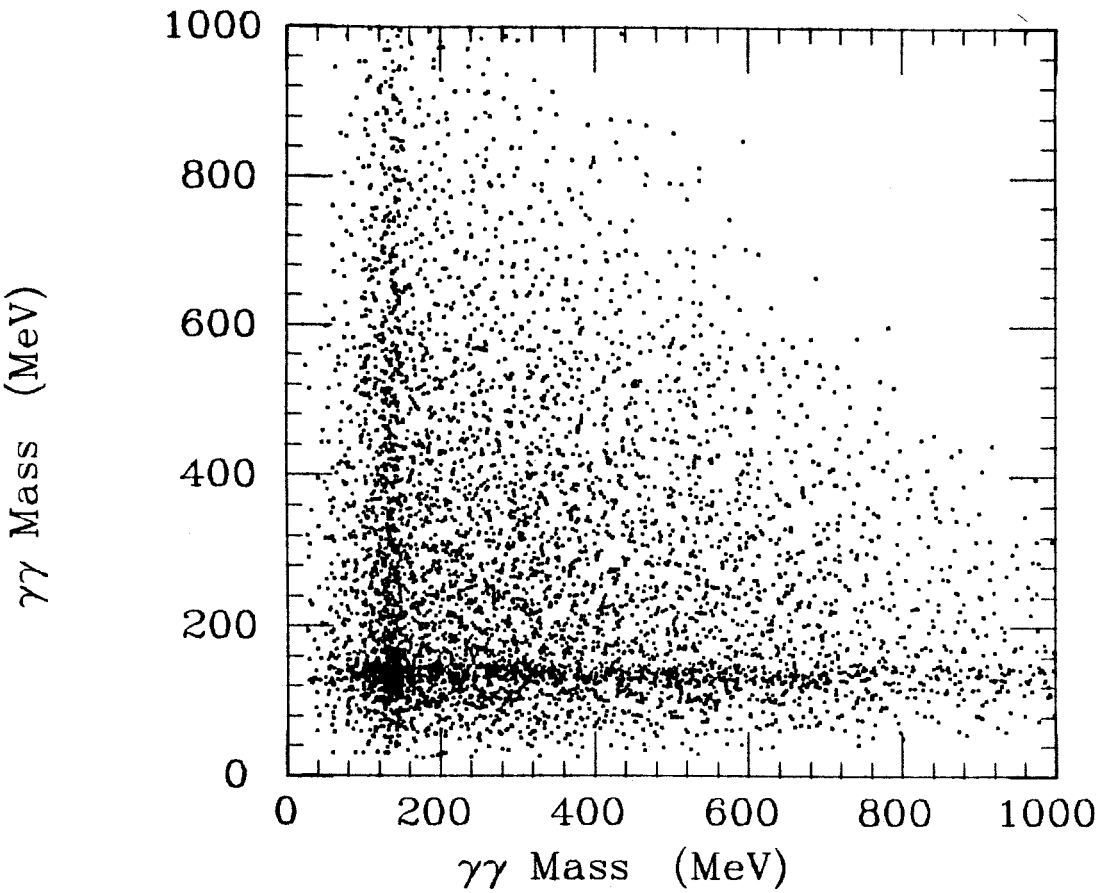

Figure 5.3: $M_{\gamma\gamma}$ vs. $M_{\gamma\gamma}$ for events with two charged tracks and five γ's. There are 15 entries per event.

Based on these observations, we kinematically fit the events which pass the initial selection to the hypothesis $\psi \to \gamma\pi^+\pi^-\pi^0\pi^0$. Starting with the four constraints of energy and momentum conservation, we lose two constraints because we do not know the charged pion energies. The π^0 mass constraint on pairs of photons adds a constraint for each unmerged π^0. Thus these kinematic fits are 4-C, 3-C, or 2-C fits, corresponding to zero, one, or two merged π^0's. Figure 5.4 shows the distribution of χ^2 probability for the fit events. Events with fit probabilities less than 20% are removed from further analysis, leaving 1831 good $\gamma\pi^+\pi^-\pi^0\pi^0$ candidate events.

Because we have no particle identification information for the charged particles, we also fit each event to the hypotheses $\psi \to \gamma K^+K^-\pi^0\pi^0$ and $\psi \to \gamma K^\pm\pi^\mp\pi^0\pi^0$. The $M_{\pi^0\pi^0}$ spectrum for events which fit the $\gamma K^\pm\pi^\mp\pi^0\pi^0$ hypothesis exhibits a peak near 500 MeV, as shown in Figure 5.5. This is interpreted as evidence for the expected process

$$\psi \to \gamma K^\pm K_S \pi^\mp$$
$$\qquad\qquad\quad \hookrightarrow \pi^0\pi^0$$

which has been observed by several experiments [5.4]. These events are removed from the analysis by rejecting any event which has greater than 10% fit likelihood for the $\gamma K^\pm\pi^\mp\pi^0\pi^0$ hypotheses, and has $M_{\pi^0\pi^0}$ in the range 450-550 MeV. Roughly 6% of the events with good $\gamma\pi^+\pi^-\pi^0\pi^0$ fits were removed by this K_S cut.

The 4π mass spectrum for events with good $\gamma\pi^+\pi^-\pi^0\pi^0$ fits, and which survive the K_S cut, is plotted in Figure 5.6. The cross section appears to rise very quickly above 1500 MeV, and there appears to be an excess of events in the range 1500-1900 MeV, above the generally rising trend of the spectrum. To demonstrate that the $\gamma 4\pi$ events are not due to $\gamma K^+K^-\pi^0\pi^0$ events, we plot in Figure 5.7 the χ^2 fit probabilities for the $\gamma K^+K^-\pi^0\pi^0$ fit hypothesis for all events

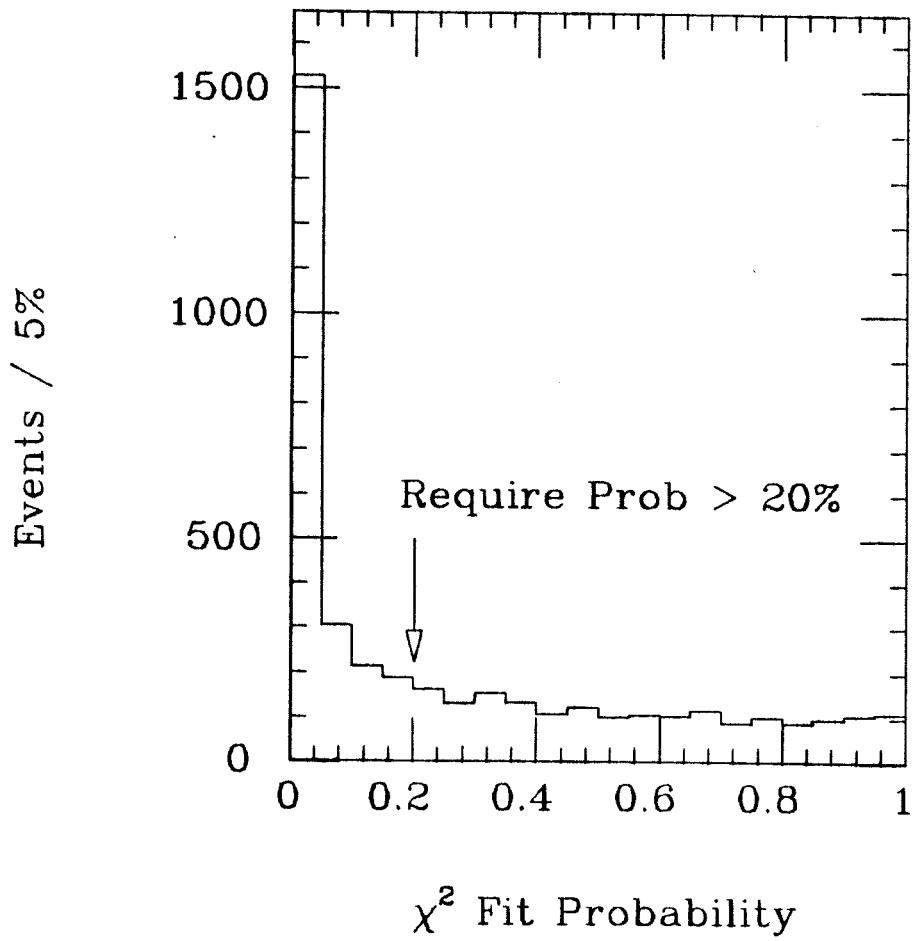

Figure 5.4: χ^2 probability distributions for kinematic fits to the hypothesis $\psi \to \gamma\pi^+\pi^-\pi^0\pi^0$. Only events with greater than 20% fit probability are treated as $\gamma 4\pi$ candidates.

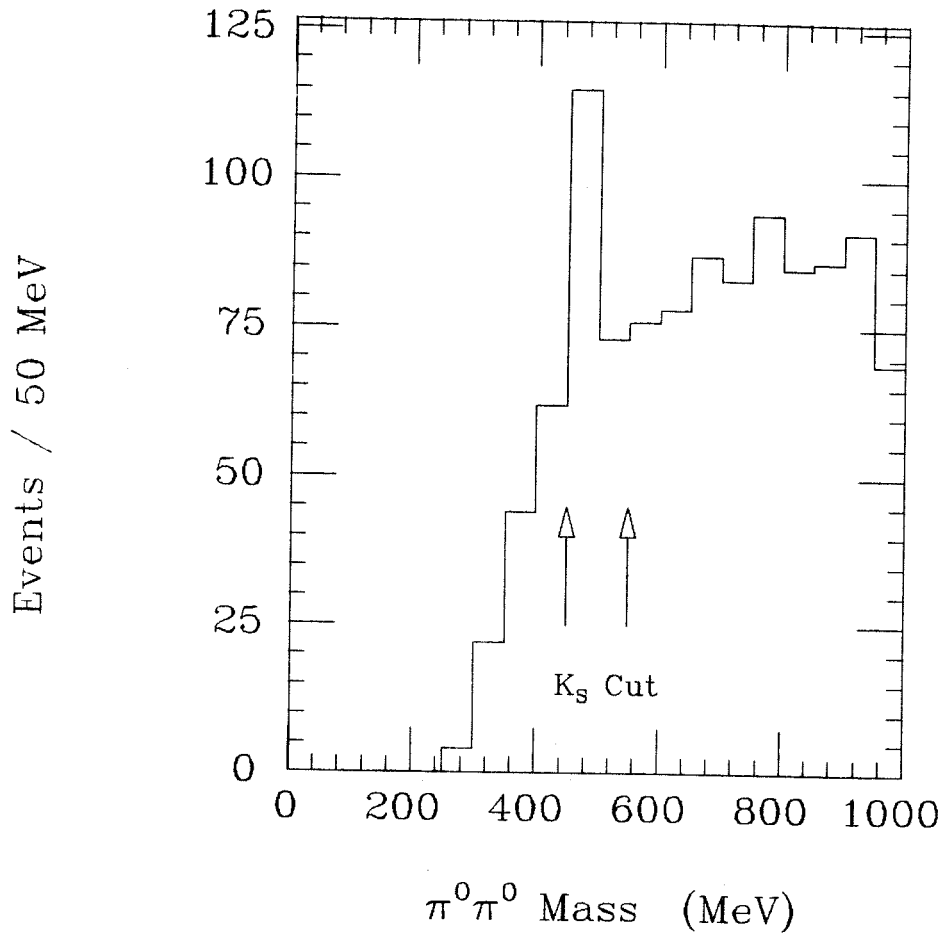

Figure 5.5: The $\pi^0\pi^0$ mass spectrum for events which fit the $\gamma K^{\pm}\pi^{\mp}\pi^0\pi^0$ hypothesis, exhibiting a peak near 500 MeV due to the process $\psi \to \gamma K^{\pm} K_s \pi^{\mp}$. Events with $M_{\pi^0\pi^0}$ in the range 450-550 MeV are removed from the $\gamma 4\pi$ candidate event sample.

with good (>20%) $\gamma 4\pi$ fits. Roughly 90% of the events have a fit probability of less than 10% to the $\gamma K^+K^-\pi^0\pi^0$ hypothesis, indicating that the Crystal Ball attains good kinematic separation between $\gamma 4\pi$ and $\gamma K^+K^-\pi^0\pi^0$ final states. However, to prevent possible biases in the final state angular distribution, we will not reject $\gamma 4\pi$ events based on the probabilities for the $\gamma K^+K^-\pi^0\pi^0$ fits.

5.3 Extraction of the $\rho\rho$ Mass Spectrum

To investigate the $\gamma\rho\rho$ final state, we next examine the invariant masses of combinations of the final state pions. As the Crystal Ball does not distinguish positive and negative charged particles, we will refer to the charged tracks as π_1^c and π_2^c, where the index 1 or 2 is arbitrary. The spectrum of $M_{\pi^c\pi^0}$ is shown in Figure 5.8. With two charged and two neutral pions, there are four such pairings of a charged and a neutral pion per event. We see a peak at the ρ mass above a broad background. More informative is a scatterplot of $M_{\pi_1^c\pi^0}$ vs. $M_{\pi_2^c\pi^0}$. In Figure 5.9, we see this distribution for all the fit $\gamma 4\pi$ events, with two entries per event. Here we see a concentration of events with both $M_{\pi_1^c\pi^0}$ and $M_{\pi_2^c\pi^0}$ near the ρ mass.

The most straightforward way of isolating the $\gamma\rho\rho$ signal is simply to choose events in which one of the entries in Figure 5.9 is inside a window close to the $\rho\rho$ point. Based on Monte Carlo $\gamma\rho\rho$ events, we define this window to be:

$$|M_{\pi_1^c\pi^0} - M_\rho| < 150 \text{ MeV}$$
$$|M_{\pi_2^c\pi^0} - M_\rho| < 150 \text{ MeV}$$

for at least one of the $\pi_1^c\pi^0$, $\pi_2^c\pi^0$ pairings. The optimal size of this window is determined by two competing factors. First, the window must be large enough to contain most of the $\rho\rho$ signal area. The ρ has an intrinsic half-width of 75 MeV, and the ρ mass resolution for this final state is measured to be a Gaussian

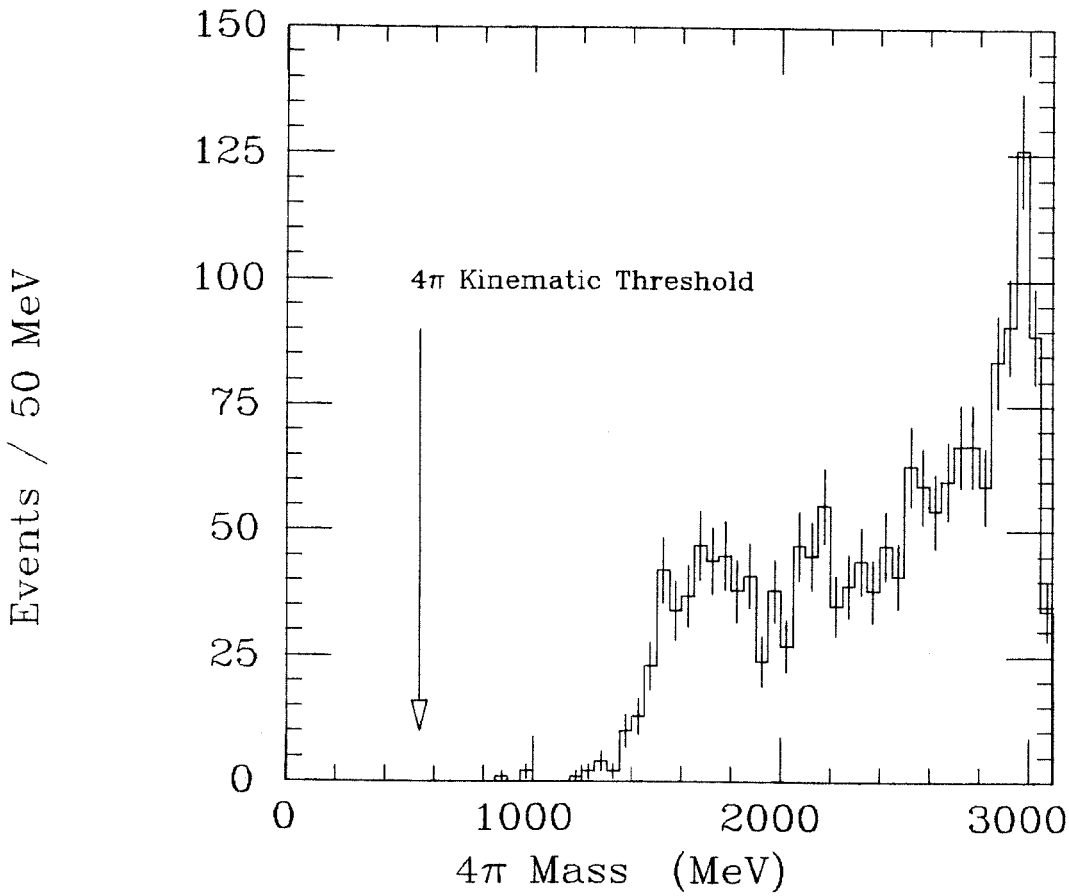

Figure 5.6: The 4π mass spectrum for events with good $\gamma\pi^+\pi^-\pi^0\pi^0$ fits, after removing K_s's.

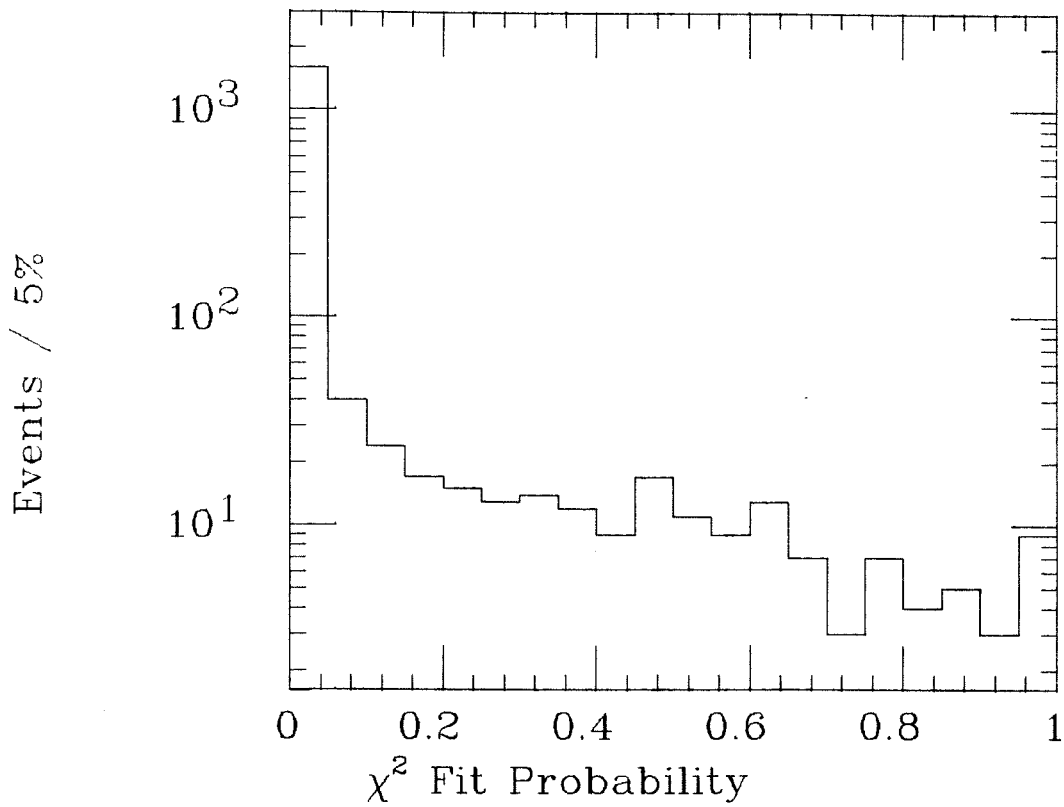

Figure 5.7: χ^2 fit probabilities for the hypothesis $\gamma K^+K^-\pi^0\pi^0$ for the $\gamma 4\pi$ event sample. Roughly 90% of the good $\gamma 4\pi$ events have less than 10% probability to satisfy the $\gamma KK\pi\pi$ hypothesis, indicating good kinematic separation between these two classes of events.

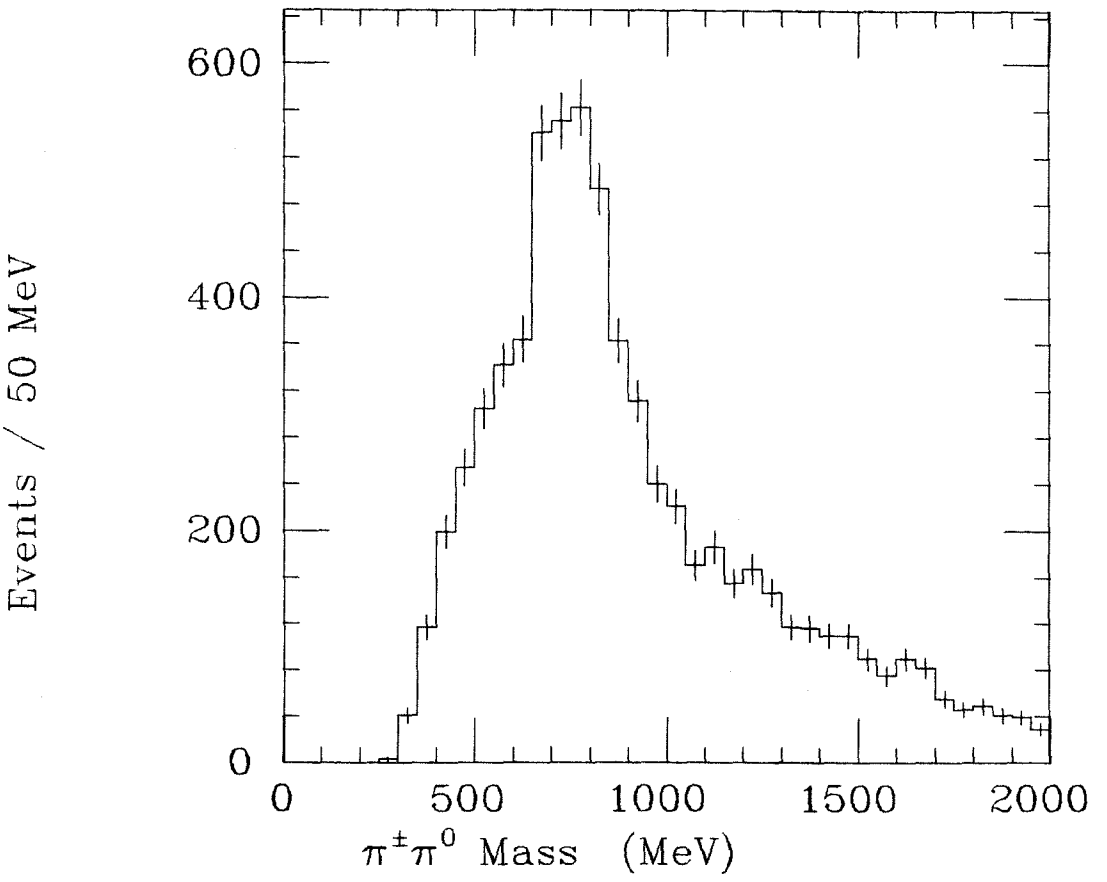

Figure 5.8: $M_{\pi^{\pm}\pi^{0}}$ for $\gamma 4\pi$ events.

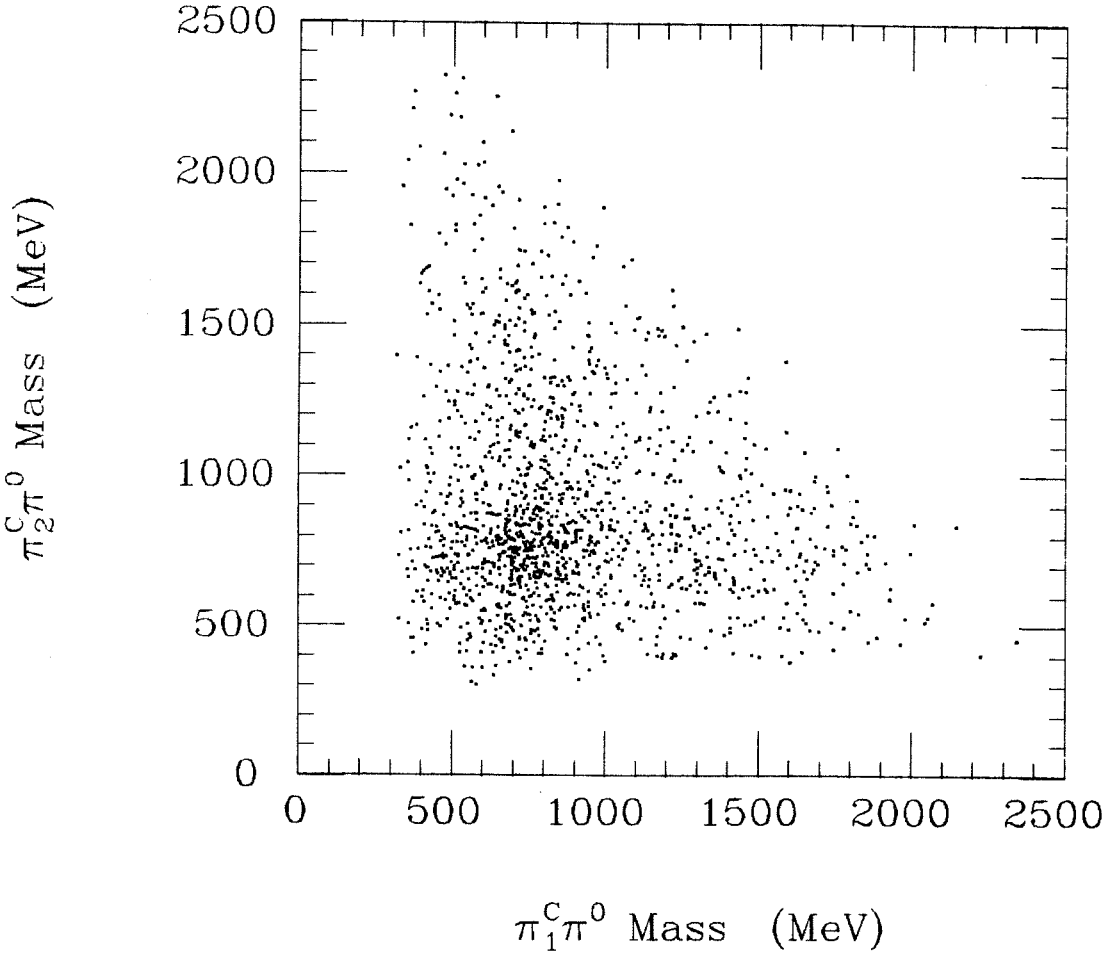

Figure 5.9: Scatterplot of $M_{\pi_1^C\pi^0}$ vs. $M_{\pi_2^C\pi^0}$ for $\gamma 4\pi$ events. There are two entries per event in this plot.

with a width of approximately 50 MeV, based on Monte Carlo events. For Monte Carlo $\gamma\rho\rho$ events which passed the event selection and had good kinematic fits, about 2/3 satisfied the above $\rho\rho$ criterion of having one $\pi_1^c\pi^0$, $\pi_2^c\pi^0$ pairing in the $\rho\rho$ window region. The other factor in setting the $\rho\rho$ window size is the amount of non-resonant background accepted. $\gamma\rho\pi\pi$ events will form bands in Figure 5.9 passing through the $\rho\rho$ window, while $\gamma 4\pi$ events will be distributed throughout the plot. Since the size of the window goes as the square of the $M_{\pi^c\pi^0}-M_\rho$ mass cut, we want to keep the window size as small as possible. The final size of ±150 MeV was chosen as a compromise between these competing demands of good efficiency and low background. For the data events, roughly one third (571 out of 1719) of the $\gamma\pi^+\pi^-\pi^0\pi^0$ events satisfied the $\rho\rho$ criterion. Figure 5.10 shows the spectrum of 4π masses for these $\rho\rho$ candidate events. The structure near 1700 MeV is very prominent now, with a rather flat background at higher masses.

To estimate the background from $\gamma 4\pi$ and $\gamma\rho\pi\pi$ events contaminating the $\rho\rho$ sample, we can look at a "sideband" region on the $M_{\pi^+\pi^0}$ vs. $M_{\pi^-\pi^0}$ scatterplot. We define the sideband events to be those in which neither $\pi^+\pi^0$, $\pi^-\pi^0$ pairing was in the $\rho\rho$ window, but that at least one combination satisfied

$$|M_{\pi_1^c\pi^0}-M_\rho| < 250 \text{ MeV}$$
$$|M_{\pi_2^c\pi^0}-M_\rho| < 250 \text{ MeV}.$$

This forms a rectangular annulus around the original $\rho\rho$ window. The 4π mass spectrum for events in the sideband region is shown in Figure 5.11. The structure at 1700 MeV is noticeably absent in the sideband plot, suggesting that the structure is indeed due to $\rho\rho$ decays.

We have fit the sideband 4π mass spectrum to a cubic polynomial, obtaining a χ^2 of 43 for 32 degrees of freedom. Next we have fit the 4π mass spectrum for $\rho\rho$ events with a Breit-Wigner resonance plus the background shape determined

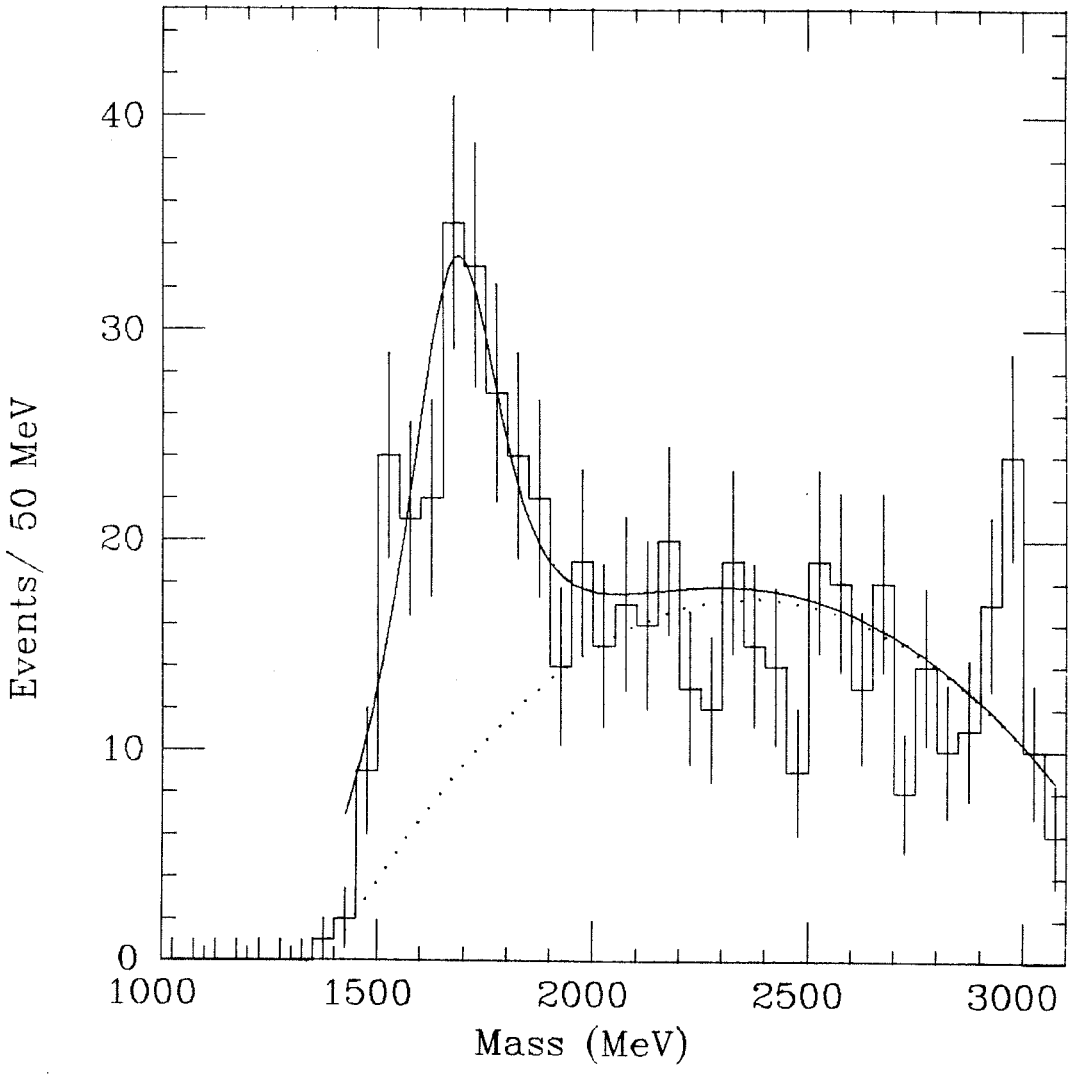

Figure 5.10: The 4π mass spectrum for events populating the $\rho\rho$ window region of Figure 5.9.

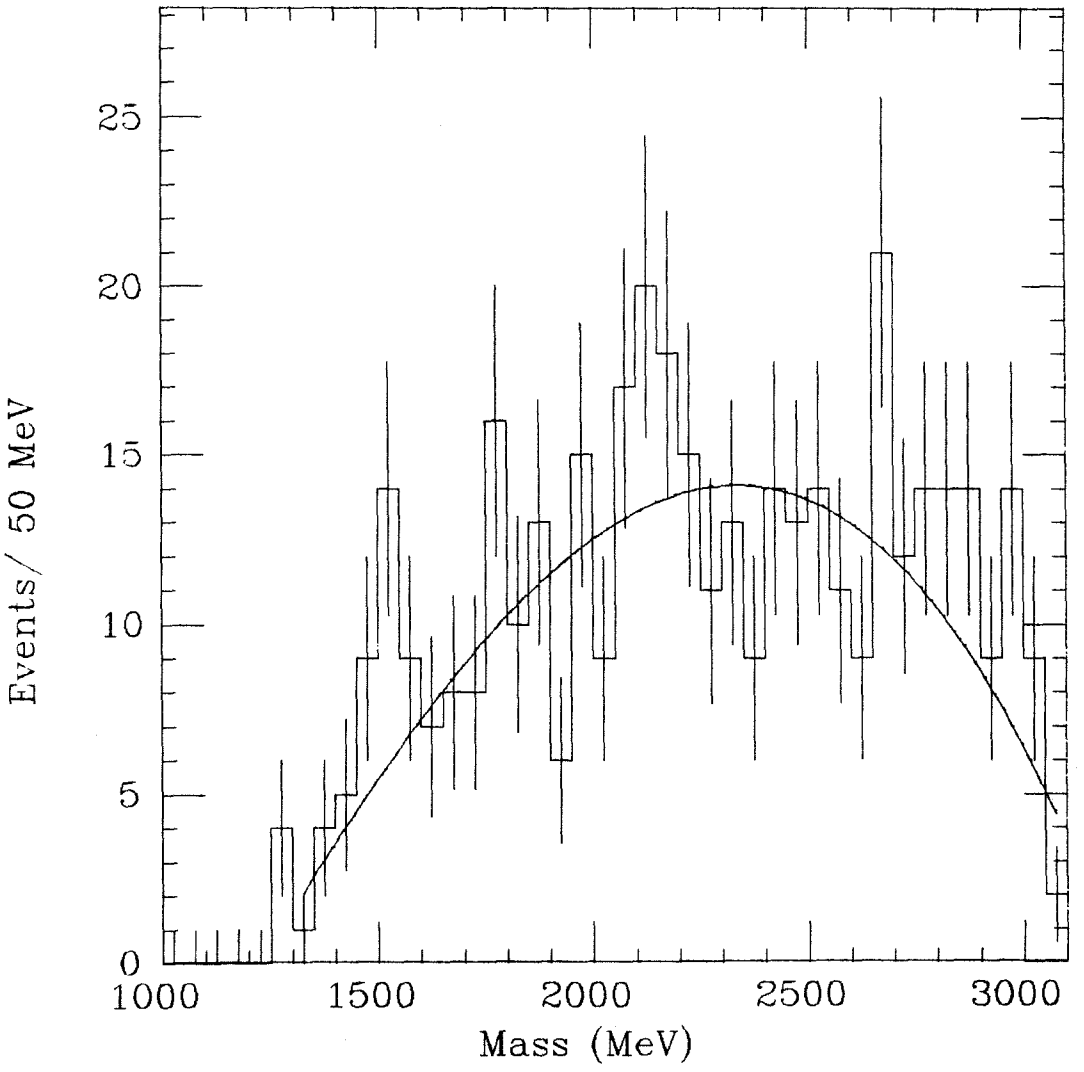

Figure 5.11: The 4π mass spectrum for events populating the sideband regions of Figure 5.9.

by the sideband fit. The Breit-Wigner is folded with the expected mass resolution of 42 MeV for a state near 1700 MeV, as determined by examining the Monte Carlo events. We obtain the following resonance parameters for the $\rho\rho$ enhancement:

$$\text{Mass} = 1700 \pm 20 \pm 30 \text{ MeV}$$

$$\Gamma = 200 \pm 50 \pm 100 \text{ MeV}.$$

The χ^2 for this fit is 47 for 30 degrees of freedom. Much of the excess comes from the low side of the 1700 MeV enhancement, where phase-space effects are expected to modify the resonance shape. Also, an excess of events just below 3000 MeV contributes to the χ^2. This is suggestive of a possible signal for $\eta_c \to \rho\rho$.

To investigate this possibility, we show in Figure 5.12 an expanded view of the 4π mass spectrum of Figure 5.10 for the η_c region. Although there does seem to be an excess of events between 2900 and 3000 MeV, it appears to be somewhat below the η_c mass. To test this quantitatively, we have fit the spectrum to a flat background plus a Breit-Wigner peak folded with a Gaussian resolution function. The mass of the η_c peak is fixed at 2984 MeV, while the width Γ is constrained to 11.5 MeV. These are the η_c mass and width values obtained by the Crystal Ball from the ψ and ψ' inclusive photon spectra [5.5]. The $\rho\rho$ mass resolution in this mass range is dominated by the energy resolution of the primary photon, and so we fix the mass resolution at 5 MeV corresponding to the expected resolution for the 111 MeV primary photon energy. The resulting fit, shown in Figure 5.12, assigns 10 ± 5 events to the η_c peak. We will use this result to place an upper limit on the branching fraction for $\eta_c \to \rho\rho$.

The efficiency for $\gamma\rho\rho$ events to satisfy all the analysis requirements, including the $\rho\rho$ window criterion, has been determined by applying the same analysis

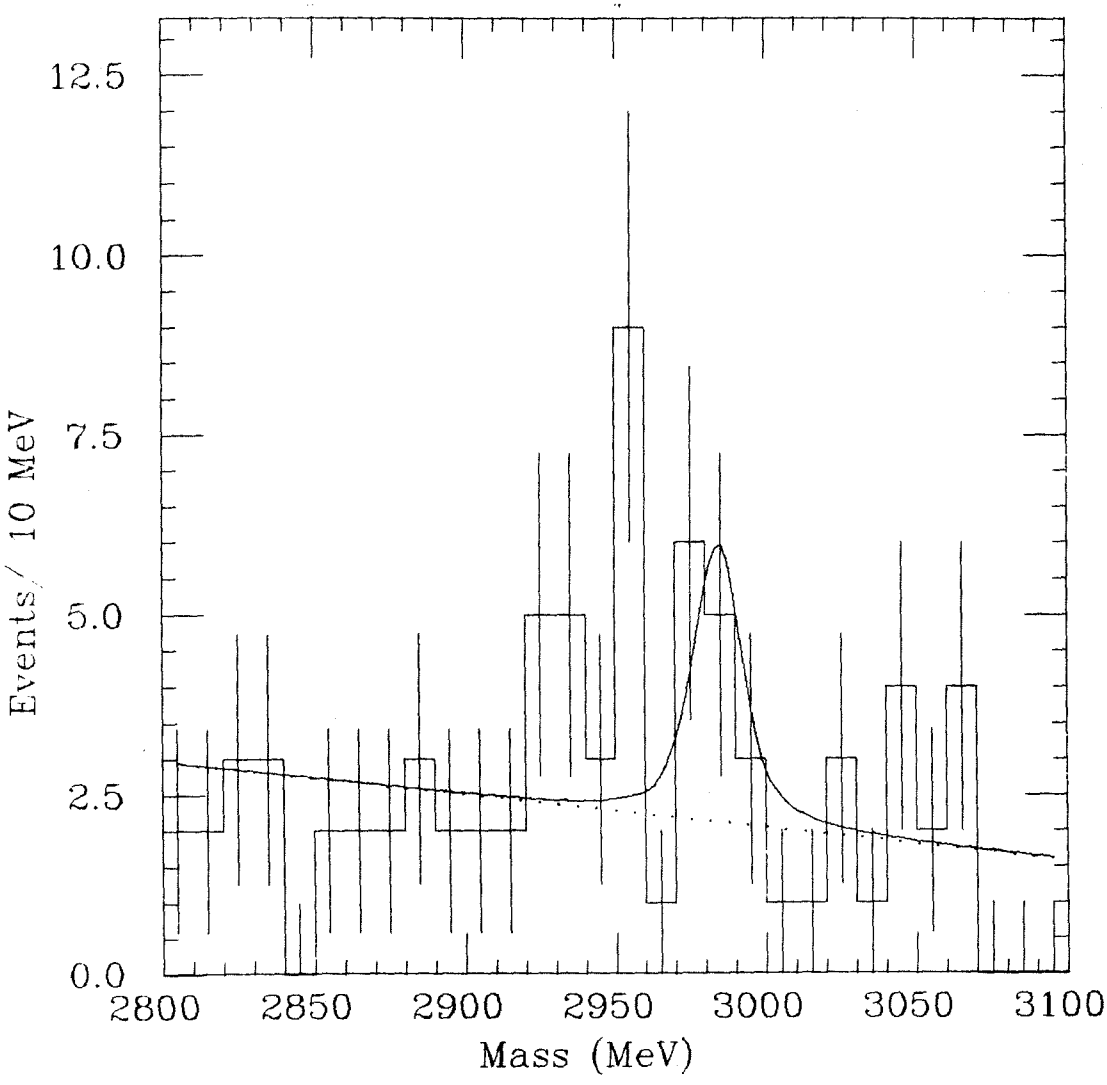

Figure 5.12: An expanded view of Figure 5.10, for $\rho\rho$ masses in the vicinity of the η_c.

to a sample of $\gamma\rho\rho$ Monte Carlo events. The events were generated according to three-particle phase space, and thus the primary photon was isotropically distributed over solid angle. Figure 5.13 shows the efficiency as a function of $\rho\rho$ mass. The large amount of CPU time necessary to simulate electromagnetic showers in the Monte Carlo and the low efficiency for this final state limit the number of events that may be generated and thus the statistical significance of the efficiency determination. The average efficiency over the full $\rho\rho$ mass range is $(3.2 \pm 0.4)\%$. A second sample of Monte Carlo events was generated for the specific decay sequence $\psi \to \gamma X(1700)$, $X(1700) \to \rho^+\rho^-$ in order to obtain a better measurement of the efficiency in the 1700 MeV region. These events were generated with the angular distributions corresponding to a pseudoscalar $X(1700)$. (These angular distributions will be presented in detail later in this chapter.) For these events, the efficiency was determined to be $(2.5 \pm 0.3)\%$, consistent with the value obtained for $\gamma\rho\rho$ phase space in the 1600-2000 MeV mass range. We will use the 2.5% value in determining the branching fraction for the 1700 MeV enhancement. Based on the number of events in the $X(1700)$ peak, the product branching fraction is determined to be

$$BF(\psi \to \gamma X(1700)) \times BF(X(1700) \to \rho\rho) = (4.6 \pm 0.8 \pm 1.5) \times 10^{-3}.$$

We have assumed that the $\rho\rho$ system is in an isoscalar state, and have scaled the number of events we see in $\rho^+\rho^-$ by a factor of 3/2 to correct for isospin. The statistical error has roughly equal contributions from the statistical error in the number of events in the X(1700) peak and the statistical error in the Monte Carlo determined efficiency. The systematic error is dominated by fluctuations in the final result when the $\rho\rho$ and sideband regions are varied. Other contributions to the systematic error include the 5% uncertainty in the number of produced ψ events, and variation in the Monte Carlo efficiency determination for

different spin-parity hypotheses.

Similarly, we can consider the upper limit based on the signal observed at the η_c. While the $\rho\rho$ efficiency shown in Figure 5.13 shows some tendency for lower efficiency at high $\rho\rho$ mass, the statistical significance is poor, and so we will take the average efficiency of $(3.2\pm0.4\pm1.0)\%$ as the efficiency for the $\eta_c\to\rho\rho$ decay, where the large systematic error represents our uncertainty in the exact behavior of the efficiency at high $\rho\rho$ masses. Based on the Crystal Ball result [5.5], $BF(\psi\to\gamma\eta_c) = (1.27\pm0.36)\times10^{-2}$, we obtain the limit

$$BF(\eta_c\to\rho\rho) < 6\%$$

at the 95% confidence limit. We have once again corrected the $\rho^+\rho^-$ result by 3/2 to account for all $\rho\rho$ charge states.

5.4 Determination of J^P for the $\rho\rho$ Enhancement

An analysis of the angular distribution of the $\gamma\pi^+\pi^-\pi^0\pi^0$ system allows us to investigate the spin and parity of the 1700 MeV $\rho\rho$ enhancement. The $\rho\rho$ system in particular allows for a very elegant and direct measurement of the parity. In the $\rho\rho$ center-of-mass, the distribution of the angle between the two $\rho\to\pi\pi$ decay planes provides an unambiguous test for the parity. This is analogous to the measurement of the parity of the π^0, in which the relative orientation of the two e^+e^- decay planes for double-Dalitz decay is sensitive to the pion parity.

Figure 5.14 defines the various angles of interest in the $\psi\to\gamma X\to\gamma\rho^+\rho^-\to\gamma\pi^+\pi^-\pi^0\pi^0$ decay sequence. The polar angle in the laboratory frame of the primary photon is designated θ_γ. Next, the angle θ_ρ describes the polar angle of the ρ^+ with respect to the X helicity axis, in the X center-of-mass. The two angles θ_{π^+} and θ_{π^-} are the polar angles of the charged pions in each of

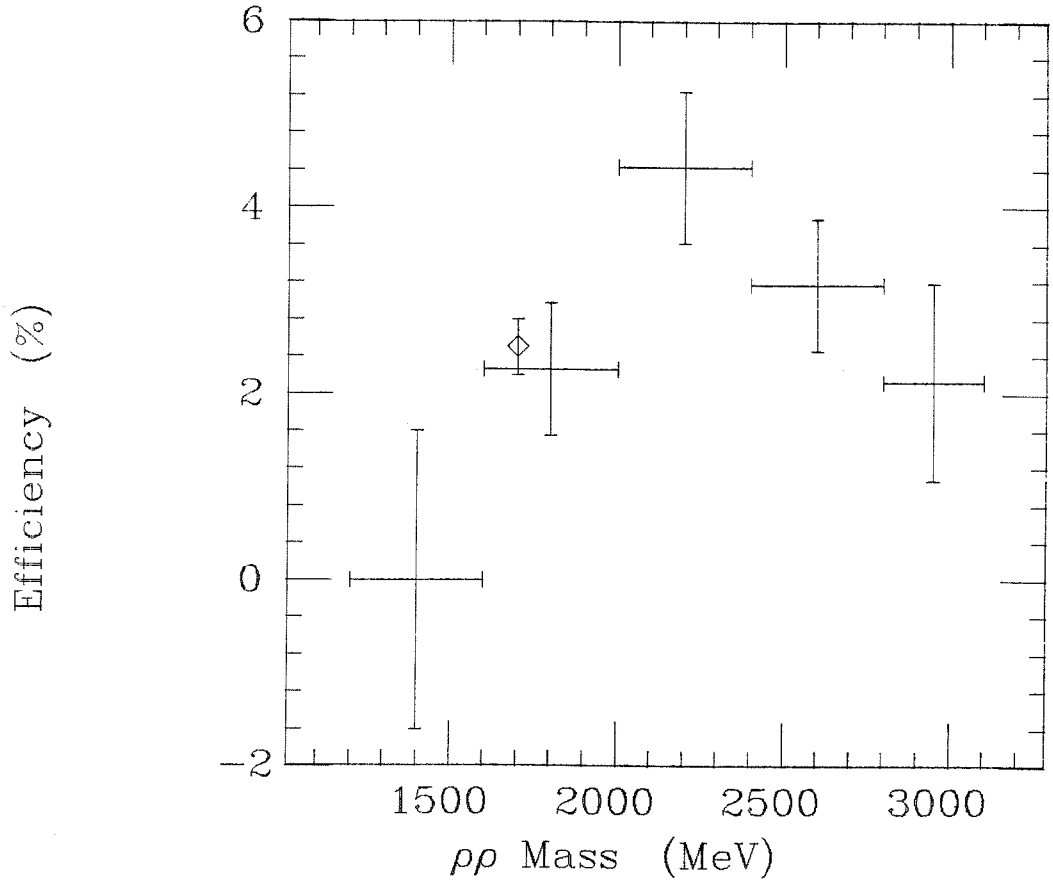

Figure 5.13: Efficiency for the full $\rho\rho$ selection analysis for Monte Carlo $\gamma\rho\rho$ events, as a function of $\rho\rho$ mass. The crosses represent the results for $\gamma\rho\rho$ phase space, and an additional point represents the result for a pseudoscalar $\rho\rho$ state at 1700 MeV.

the ρ decays. Finally, the angle χ is defined to be the angle between the two $\rho\to\pi\pi$ decay planes, in the $\rho\rho$ center of mass. Explicitly, we have

$$\cos\chi = [\hat{n}(\pi^+)\times\hat{n}(\pi^0_A)]\cdot[\hat{n}(\pi^-)\times\hat{n}(\pi^0_B)]$$

where the $\hat{n}$'s are the direction unit vectors for the pions in the $\rho\rho$ center of mass. Clearly the angles θ_ρ, $\theta_{\pi^\pm}$, and χ depend on the particular pairing of pions used to define the ρ's.

T. L. Trueman has shown how the angular distributions of χ and $\theta_{\pi^\pm}$ determine the parity and signature $(-1)^J$ of the $\rho\rho$ system [5.6]. We will briefly review his analysis here. Parity and charge conjugation invariance provide constraints on the allowed helicity amplitudes for $X\to\rho\rho$. Since we are looking at the process $\psi\to\gamma\rho\rho$, and since both ψ and γ have $C=-1$, the C quantum number for the $\rho\rho$ system must be $+1$. In this case, the helicity amplitudes A_{λ_+,λ_-} representing the amplitude for X to decay into a ρ^+ with helicity λ_+, and a ρ^- with helicity λ_-, must satisfy the relations:

$$A_{-\lambda_+,-\lambda_-} = P(-1)^J A_{\lambda_+,\lambda_-}$$

$$A_{\lambda_+,\lambda_-} = (-1)^J A_{\lambda_-\lambda_+}$$

where J and P are the spin and parity quantum numbers for the $\rho\rho$ state. Thus for each spin-parity assignment, there is a separate set of relations among the helicity amplitudes.

Integrating the full angular distribution over all other angles, we obtain predictions for the χ and $\theta_{\pi^\pm}$ distributions. The distribution for χ takes the form

$$F(\chi) = 1 + \alpha\cos\chi + \beta\cos 2\chi.$$

If the $\pi^\pm\pi^0$ pairs are indeed purely from ρ decays, α is identically zero. A non-

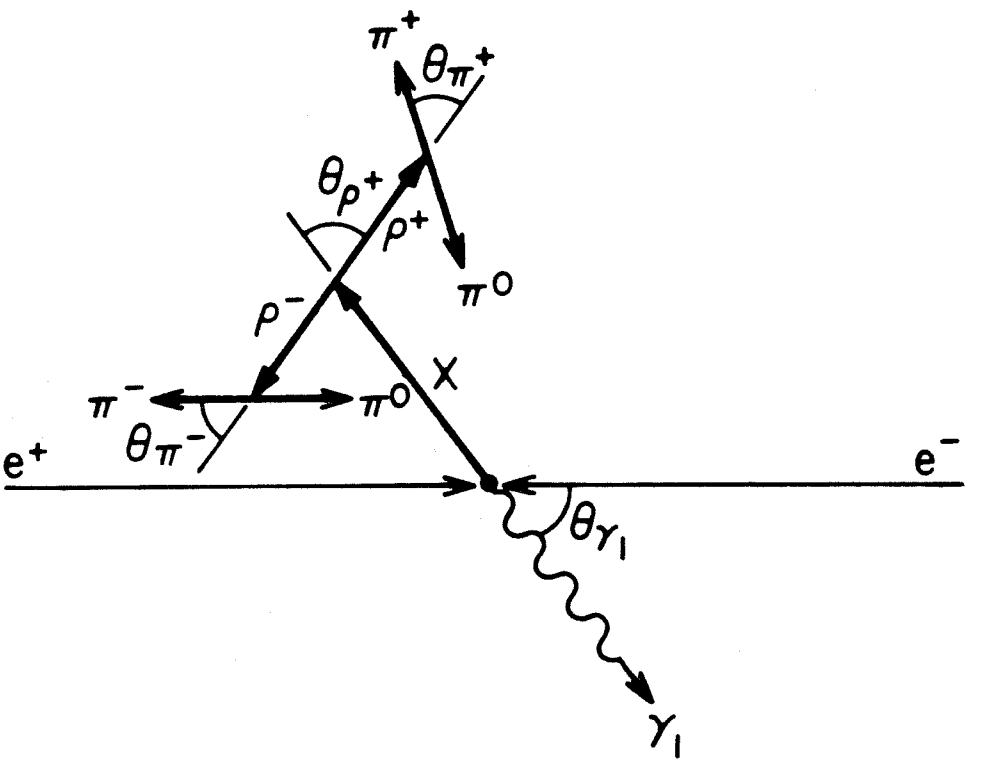

Figure 5.14: The relevant decay angles for the decay sequence $\psi \to \gamma X \to \gamma \rho^+ \rho^- \to \gamma \pi^+ \pi^- \pi^0 \pi^0$.

zero value of α indicates that there is interference between the $\rho\to\pi\pi$ decays and some even angular momentum $\pi\pi$ background, such as $X\to\rho\pi\pi$, with the $\pi\pi$ system in an s-wave. The $\theta_{\pi^\pm}$ distribution can be parametrized

$$G(\cos\theta_{\pi^\pm}) = 1 + \zeta P_2(\cos\theta_{\pi^\pm})$$

where P_2 is the second order Legendre polynomial. β and ζ are simply functions of the helicity amplitudes. Based on the helicity amplitude relations listed above, we obtain the allowed values of β and ζ for each of the possible spin-parity assignments.

$P=-1$, $(-1)^J=+1$: For this case there are only two independent helicity amplitudes, $A_{1,1}$ and $A_{1,0}$, leading to a linear relationship between β and ζ: $\zeta=\frac{1}{2}(1+3\beta)$, where β may range from -1 up to 0. In the particular case of $J^P=0^-$, only $A_{1,1}$ is allowed, and we get a unique prediction $\beta=-1$ and $\zeta=-1$.

$P=-1$, $(-1)^J=-1$: Only one independent amplitude exists for this case, namely $A_{1,0}$. This gives a unique prediction of $\beta=0$ and $\zeta=\frac{1}{2}$.

$P=+1$, $(-1)^J=-1$: With two independent amplitudes $A_{1,-1}$ and $A_{1,0}$, β is identically zero while ζ may range from $+\frac{1}{2}$ to -1. For $J=1$, only $A_{1,0}$ is allowed, constraining ζ to $+\frac{1}{2}$.

$P=+1$, $(-1)^J=+1$: For this case, all amplitudes are allowed, and we obtain the weaker constraints $0<\beta<1$ and $-1<\zeta<2$. For the scalar case $J=0$, only two independent amplitudes are allowed, and we obtain a linear relation $\zeta=2-3\beta$ for $0<\beta<1$.

Figure 5.15 shows the allowed regions of β and ζ for the various J^P assignments.

For the angular analysis, we make slightly more restrictive cuts on the pion pair masses, demanding

$$|M_{\pi_1^c\pi^0} - M_\rho| < 100 \text{ MeV}$$
$$|M_{\pi_2^c\pi^0} - M_\rho| < 100 \text{ MeV}.$$

If just one of the two possible pairings of pions satisfies this cut, then that combination is used to define the $\rho\rho$ decay angles. If both pairings reside in the $\rho\rho$ window, then we use the combination for which the quantity

$$MAX[\, M_{\pi_1^c\pi^0} - M_\rho \,,\, M_{\pi_2^c\pi^0} - M_\rho \,]$$

is smallest to define the decay angles. Using this more stringent $\rho\rho$ requirement reduces the size of the $\rho\rho$ window by over 50%, yielding a cleaner sample of $\rho\rho$ candidates, at the expense of efficiency. Figure 5.16 shows the 4π mass spectrum with this tighter $\rho\rho$ criterion. To examine the angular distributions for particles in the X(1700) enhancement, we select events with 4π masses between 1500 and 1900 MeV. This sample contains 144 events.

The distributions for the angles θ_γ, θ_ρ, θ_{π^+} and θ_{π^-}, and χ are shown in Figure 5.17. Fitting the χ distribution to the form

$$F(\chi) = 1 + \alpha\cos\chi + \beta\cos 2\chi$$

we obtain $\alpha = -0.03 \pm 0.05$ and $\beta = -0.99 \pm 0.06$. The fact that α is consistent with 0 indicates the absence of any significant interference between the ρ decay and any even angular momentum $\pi\pi$ background. The negative value of β clearly indicates a negative parity state. In addition, since β is non-zero, we conclude that the spin is even.

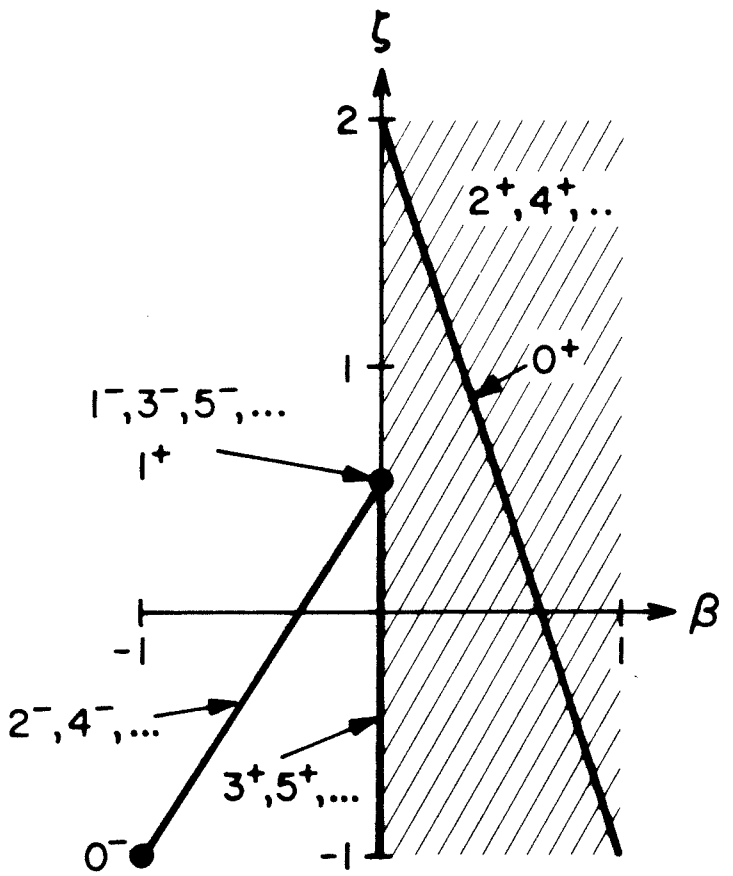

Figure 5.15: Allowed regions of β and ζ for various spin-parity assignments.

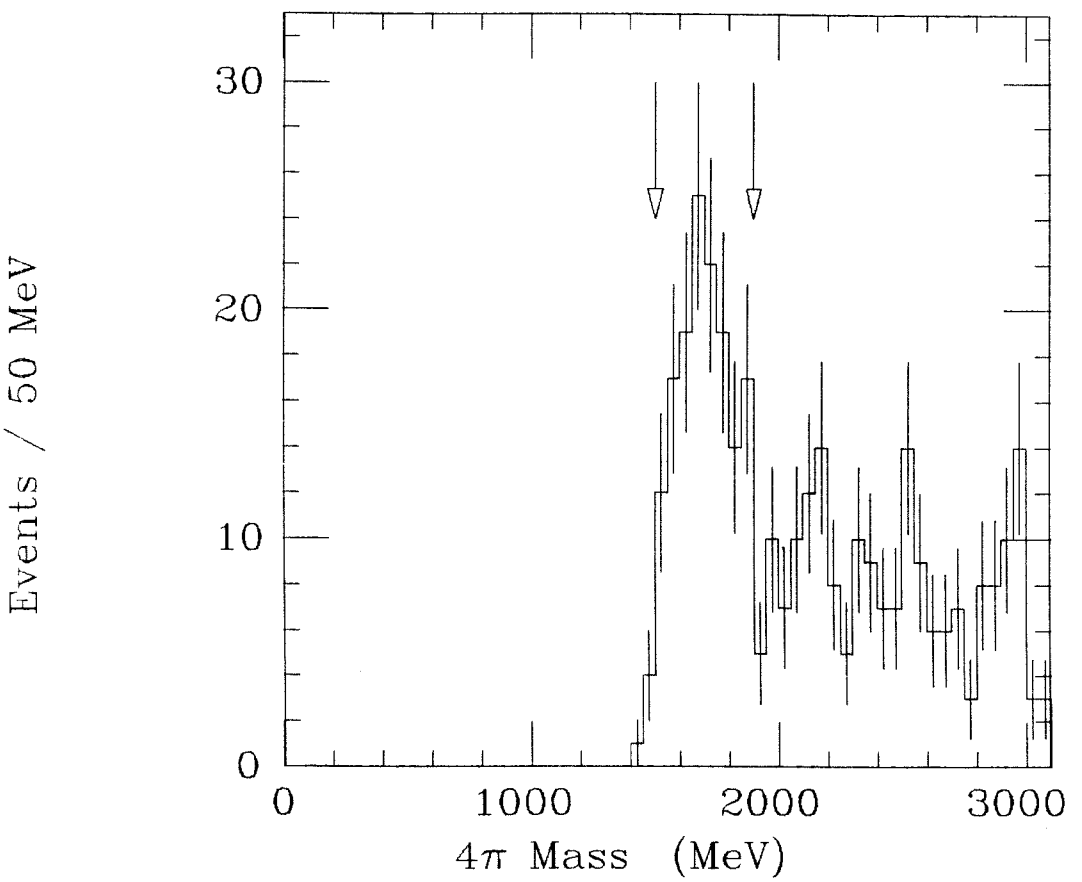

Figure 5.16: The $\pi^+\pi^-\pi^0\pi^0$ mass spectrum for the $\rho\rho$ event candidates using the more restrictive ±100 MeV $\rho\rho$ mass window. Events with masses in the range 1500-1900 MeV are used to determine the spin and parity of the 1700 MeV enhancement.

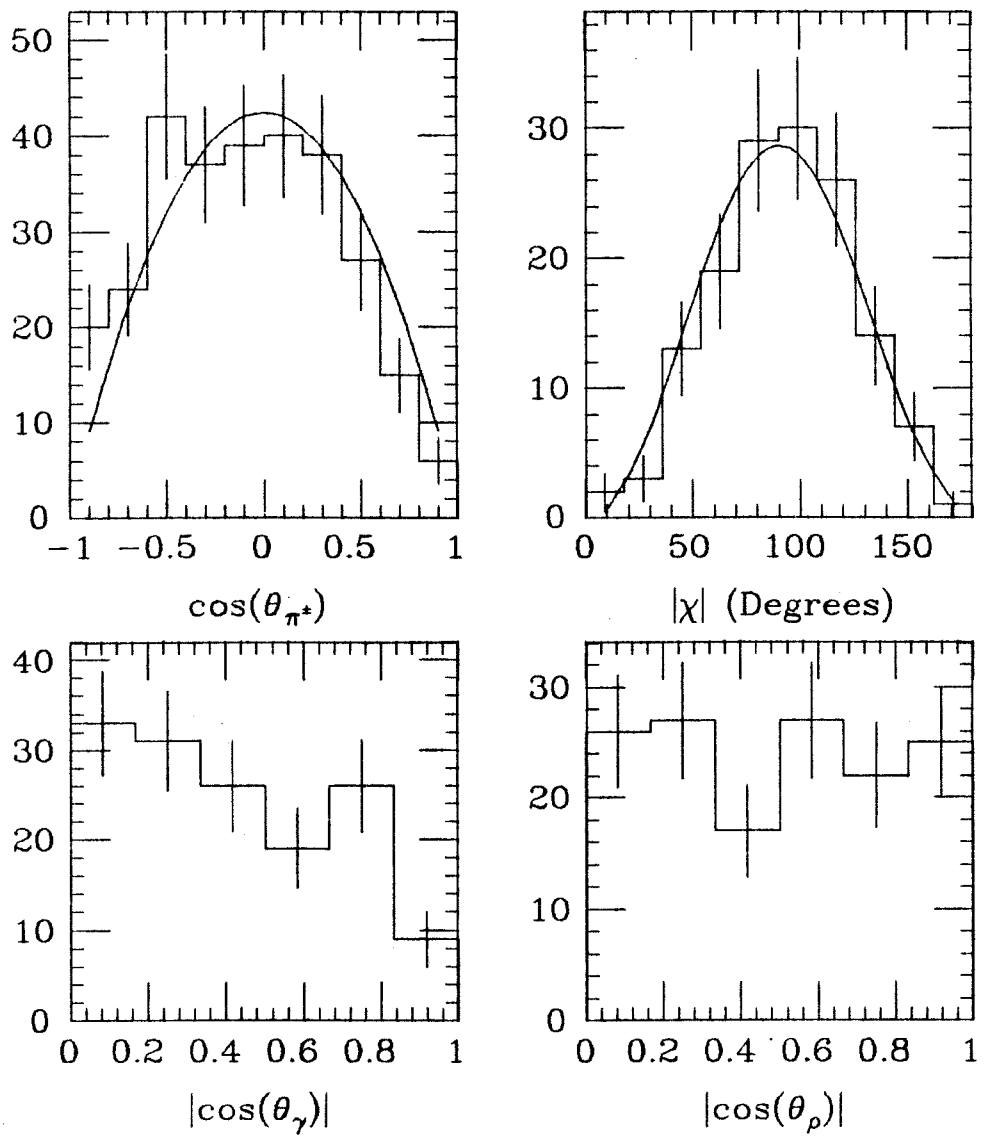

Figure 5.17: The distributions of the various decay angles for events in the 1700 MeV $\rho\rho$ enhancement. Best fits are shown for the χ and $\theta_{\pi^\pm}$ distributions.

The distribution of $\cos\theta_{\pi^\pm}$, the charged pion angles with respect to the ρ helicity axes, has been fit to the form

$$G(\cos\theta_{\pi^\pm})=1+\zeta P_2(\cos\theta_{\pi^\pm})$$

with the result $\zeta=-0.96\pm0.10$. Once again, this result is consistent with a negative parity, even spin state. For $J^P=0^-$, we recall that β and ζ are predicted to both equal -1. For $2^-,4^-,\cdots$, the two allowed helicity amplitudes permit a range of values for β and ζ. However, $\beta=\zeta=-1$ can only occur if the A_{10} amplitude vanishes. Thus, based on our fitted values of β and ζ we see that only J-even and $P=-1$ are allowed. The data agree very well with the unique prediction for 0^-, and are consistent with the range of allowed solutions for higher spin only if one of the two allowed helicity amplitudes vanishes.

To ensure that the efficiency is flat with respect to the angles χ and $\theta_{\pi^\pm}$, we have generated Monte Carlo events for the process

$$\psi\to\gamma X(1700),\quad X(1700)\to\rho^+\rho^-,\quad \rho^-\to\pi^-\pi^0,\quad \rho^+\to\pi^+\pi^0$$

with $J^P(X(1700))=0^-$. Using identical selection criteria, and fitting the χ and $\theta_{\pi^\pm}$ distributions, we obtain $\alpha=0.14\pm0.14$, $\beta=-0.93\pm0.16$, and $\zeta=-1.07\pm0.16$, in good agreement with the expectations for a pseudoscalar.

At this point it is important to note one approximation that has been implicitly made throughout this analysis. For each event, there are two possible combinations of $\pi^+\pi^0$ and $\pi^-\pi^0$. We have chosen the combination that is closest to having both pion pairs at the ρ mass. Our $\rho\rho$ candidates were defined as those events for which this "best" combination was within a window about the $\rho\rho$ point on the $\pi^+\pi^0$ vs. $\pi^-\pi^0$ mass plot. In addition, all the angles used in the spin-parity analysis were defined based on this particular combination. However, because

of the large ρ width, the other combination of pion pairs can have a non-negligible amplitude for $\rho\rho$. In fact, the correct quantum mechanical amplitude must include the interference between the two possible pion pairings. If we label the neutral pions as π^0_A and π^0_B, then the full amplitude must be symmetric under the interchange of π^0_A and π^0_B, and takes the form

$$BW(\pi^+,\pi^0_A)\,BW(\pi^-,\pi^0_B)\,W(\pi^+,\pi^0_A,\pi^-,\pi^0_B) \;+\; BW(\pi^+,\pi^0_B)\,BW(\pi^-,\pi^0_A)\,W(\pi^+,\pi^0_B,\pi^-,\pi^0_A)$$

where the BW's are relativistic Breit-Wigner resonances for the ρ^+ and ρ^-, and W is the full angular distribution. Of course, the angles θ_ρ, $\theta_{\pi^\pm}$ and χ all depend on the particular pairing of pions used to form the ρ's, and thus W is different for the two pairings. The matrix element, which is the square of this amplitude, will contain the squares of each of the two terms along with an interference term. Our analysis so far has neglected the second combination of photons. How large are the terms we are omitting?

To answer this question, four-vectors were generated for the $\rho^+\rho^-$ decay of a particle of mass 1700 MeV, using the correct amplitude including interference effects between the two possible pion pairings. Three different cases were considered for the $\rho\rho$ system. One set of events used the angular distributions for a pseudoscalar, while the other two sets were for the scalar case. These two sets correspond to the two independent helicity amplitudes allowed for $J^P=0^+$. Based on the generated four-vectors (these events were not passed through the detector simulation program), a "best" $\rho\rho$ pairing was chosen based on the pion combination that minimized

$$MAX[\,M_{\pi^+\pi^0}-M_\rho\,,\,M_{\pi^-\pi^0}-M_\rho\,]$$

and the χ and $\theta_{\pi^\pm}$ distributions for this combination were plotted. Figure 5.18

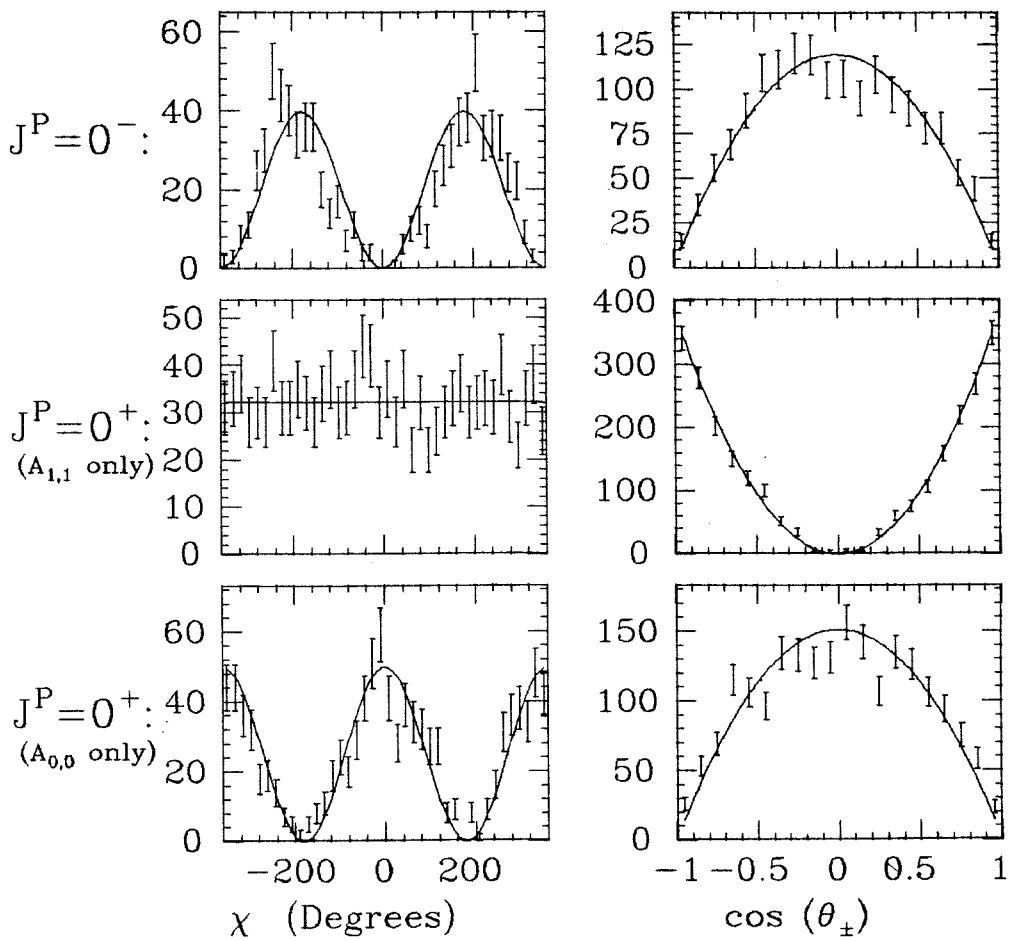

Figure 5.18: For 1700 MeV $\rho\rho$ decays, generated using the full amplitude which includes interference between the two possible pion pairings, we plot the χ and $\theta_{\pi^\pm}$ distributions based on the "best" pairing. Results are shown for pseudoscalar and scalar $\rho\rho$ system. For the scalar case, two different possible helicity amplitudes are shown. The good agreement indicates that the interference effects are small and may be neglected.

shows the χ and $\theta_{\pi^\pm}$ distributions for the "better" combination, along with the predictions based on ignoring the other combination. We see that the the agreement is very good, and that the scalar and pseudoscalar cases are clearly distinguished, From this we conclude that our approximation of ignoring the second pion pairing in forming the $\rho\rho$ amplitude is justified.

5.5 Conclusions

We have examined the $\gamma\pi^+\pi^-\pi^0\pi^0$ final state in an effort to study the $\rho\rho$ structure near 1700 MeV reported by the Mark II experiment. Choosing events in which one of the possible pairings of charged and neutral pions is consistent with a $\rho\rho$ interpretation, we observe significant structure near 1700 MeV. An examination of sideband events for which neither pion pairing satisfies the $\rho\rho$ requirement demonstrates that the 1700 MeV structure is not due to $\gamma 4\pi$ or $\gamma\rho\pi\pi$ processes.

We have examined the decay angles for $\rho\rho$ candidate events with masses between 1500 and 1900 MeV. In particular, the relative angle between the ρ decay planes in the $\rho\rho$ center of mass provides an unambiguous test of the parity of the $\rho\rho$ system. Fitting the observed distributions, we find that the 1700 MeV structure has negative parity and even spin. For spin 0, the angular distributions are completely determined, and agree well with our observations. For higher spin, the two allowed helicity amplitudes permit a range of distributions. However, to fit our observations, one of these two allowed helicity amplitudes would have to be very small. Based on the parity measurement, we conclude that the 1700 MeV structure is not associated with the $\theta(1700)$ particle observed as a resonance in $\eta\eta$ and KK decays.

Chapter V References

[5.1] D. L. Burke *et al.*, Phys. Rev. Lett. 49, 632 (1982).

[5.2] C. Edwards *et al.*, Phys. Rev. Lett. 48, 458 (1982).

[5.3] M. E. B. Franklin, Ph.D thesis, SLAC Report 254, 1982.

[5.4] C. Edwards *et al.*, Phys. Rev. Lett. 49, 259 (1982); D. L. Scharre *et al.*, Phys. Lett. 97B, 329 (1980); W. Toki *et al.*, "MARK III Results from SPEAR," SLAC-PUB-3262, 1983.

[5.5] J. Gaiser, SLAC Report 225 (1982).

[5.6] T. L. Trueman, Phys. Rev. D18, 3423 (1978).

Chapter VI

A Search for the Decay $\psi \to \gamma\eta\eta'$

6.1 Introduction

The $\theta(1700)$ was first observed by the Crystal Ball in the channel $\psi \to \gamma\eta\eta$ [6.1]. Table 6.1 summarizes the present experimental status of the θ. We report here on a search for the related decay $\psi \to \gamma\eta\eta'$. Theoretical predictions based on an effective Lagrangian suggest that the $\theta \to \eta\eta'$ rate could be over twice as large as the $\theta \to \eta\eta$ rate, in spite of the reduced phase space [6.2]. After reviewing the theoretical model, results are presented for the $\eta' \to \gamma\rho$ final state.

Table 6.1 Experimental Status of θ

Experiment: [reference]:	Crystal Ball [6.1]	Mark II [6.3]	Mark III [6.3]
Mode:	$\eta\eta$	K^+K^-	K^+K^-
Mass (MeV):	1670±50	1708±30	1719±6±10
Γ (MeV):	160±80	156±60	117±23±10
$BF(\psi \to \gamma\theta) \times BF(\theta \to X)$:	$(3.8\pm1.1\pm0.8) \times 10^{-4}$	$(6.0\pm0.9\pm2.5) \times 10^{-4}$	$(4.8\pm0.7\pm0.9) \times 10^{-4}$

6.2 Theoretical Predictions

A spin-parity analysis of the θ signal in the $\gamma\eta\eta$ final state [6.1] found that $J^P=2^+$ was preferred over 0^+ at the 95% confidence level. A similar analysis for the γK^+K^- final state by the Mark II [6.3] also found the 2^+ favored at the 78% confidence level. However, possible contamination of the θ region by the nearby $f'(1515)$, with $J^P=2^+$, casts some suspicion on these results. We will keep this

uncertainty in mind throughout the following discussion.

Rosner and Tuan [6.5] have treated θ decays in a mixing model which takes into account $\theta - f - f'$ mixing, and assumes SU(3) flavor symmetry in the tensor decays. Starting with a pure glueball θ_0, and pure quarkonic states $f_0 = \frac{1}{\sqrt{2}}|u\bar{u}+d\bar{d}\rangle$ and $f_0' = |s\bar{s}\rangle$, they seek a mixing solution constrained by the observed masses and decay properties of the physical states. The only way they can accommodate the present experimental observations is to have a mixing scheme in which the f' decouples, remaining essentially a pure $s\bar{s}$ state, while the f and θ mix. Based on their mixing solution, flavor SU(3) symmetry gives roughly equal couplings [6.6]:

$$\langle \eta\eta \,|\, \theta \rangle \approx \langle \eta\eta' \,|\, \theta \rangle.$$

To get a result for the actual decay rates, we must add the phase space factor, which for the decay of a spin 2 object into two pseudoscalars takes the form:

$$P.S. = \frac{p^5}{M(2^+)},$$

where p is the momentum of the decay pseudoscalars in the tensor meson center of mass, and $M(2^+)$ is the mass of the tensor meson. For $\theta(1700)$, p=649 MeV for the $\eta\eta$ decay, and and p=382 MeV for the $\eta\eta'$ decay. Thus the mixing model of Rosner and Tuan predicts

$$\frac{\Gamma(\theta \to \eta\eta')}{\Gamma(\theta \to \eta\eta)} \approx \left[\frac{382}{649}\right]^5 = 0.07,$$

which, given the Crystal Ball measurement for $\eta\eta$, would predict a product branching fraction of

$$BF(\psi \to \gamma\theta) \times BF(\theta \to \eta\eta') \approx 2.7 \times 10^{-5}.$$

Such a small rate would make observation of the $\eta\eta'$ decay mode nearly impossible in the Crystal Ball dataset. For example, for the $\eta\eta'$ final state in which the η decays into two γ's and the η' decays into $\gamma\rho$, we would expect only seven events. Once the detection efficiency is taken into account, we would expect to see less than one event.

It is important to note, however, that the suppression for the $\eta\eta'$ mode is coming entirely from kinematic factors. If the θ were indeed a 0^+ state, the kinematic suppression of the $\eta\eta'$ mode relative to the $\eta\eta$ mode would be 0.59 instead of 0.07, a difference of nearly a full order of magnitude. Of course, if this were the case there would be no mixing between the θ and the f ; any quarkonic content of the θ would come from mixing with scalar $q\bar{q}$ mesons.

Schecter [6.2] has generalized the model of Rosner and Tuan to include an extra term that enhances the coupling of the pure glueball θ_0 to the pure flavor SU(3) singlet η_0'. The motivation for this extra term is based on two assumptions: that the η' could have a large gluonic contribution to its wave function, and that a tensor glueball might have enhanced decays to pairs of lighter pseudoscalar glueballs. In this model, mixing is treated for both the tensor mesons (f, f', θ), and for the pseudoscalar mesons (η, η'). Because of an ambiguity in the relative phases of two amplitudes, Schecter finds two possible solutions, corresponding to the decay ratios

$$\frac{\Gamma(\theta \to \eta\eta')}{\Gamma(\theta \to \eta\eta)} = 2.09 \text{ or } 0.03.$$

The larger solution, corresponding to constructive interference of two of the allowed amplitudes, corresponds to a product branching fraction of

$$BF(\psi \to \gamma\theta) \times BF(\theta \to \eta\eta') = 7.9 \times 10^{-4},$$

which might be observable in the Crystal Ball dataset. With a detection efficiency of 5%, we would expect to see 10 events in the $\eta\to\gamma\gamma$, $\eta'\to\gamma\rho$ decay mode.

6.3 Experimental Analysis

We have searched for $\gamma\eta\eta'$ events in the decay sequence

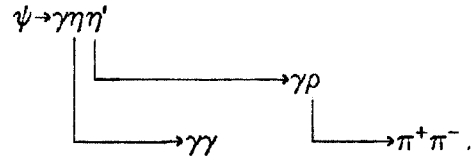

Events were selected to have the proper final state multiplicity based on the following requirements:

1. Two charged tracks,
2. Four photons,
3. $|\cos\theta_{beam}| < .9$ for all tracks,
4. $\cos\theta_{ij} < .95$ for all pairs of tracks.

From the full ψ dataset, 23,781 events satisfied these criteria. To get a feeling for the various final states that populate this topology, we plot in Figure 6.1 $M_{\gamma\gamma}$ vs. $M_{\gamma\gamma}$ for that subset of events for which all four photons have shower patterns consistent with electromagnetic showers. There are three entries per event in this plot. Evidence is seen for $\pi^0\pi^0$, $\eta\pi^0$, and $\gamma\gamma\pi^0$ structure in the 4γ final state. η bands, which would be associated with $\gamma\eta\eta'$ events, are not seen.

All 23,781 events were next fit to the kinematic hypothesis $\psi\to\gamma\gamma\eta\pi^+\pi^-$, $\eta\to\gamma\gamma$. Since we do not measure the charged particle momenta, this is a 3-C fit. The η' and ρ mass constraints are not used in this fit; rather, the $\pi\pi$ and $\gamma\pi\pi$ mass distributions will be used to select η' events and also to determine the

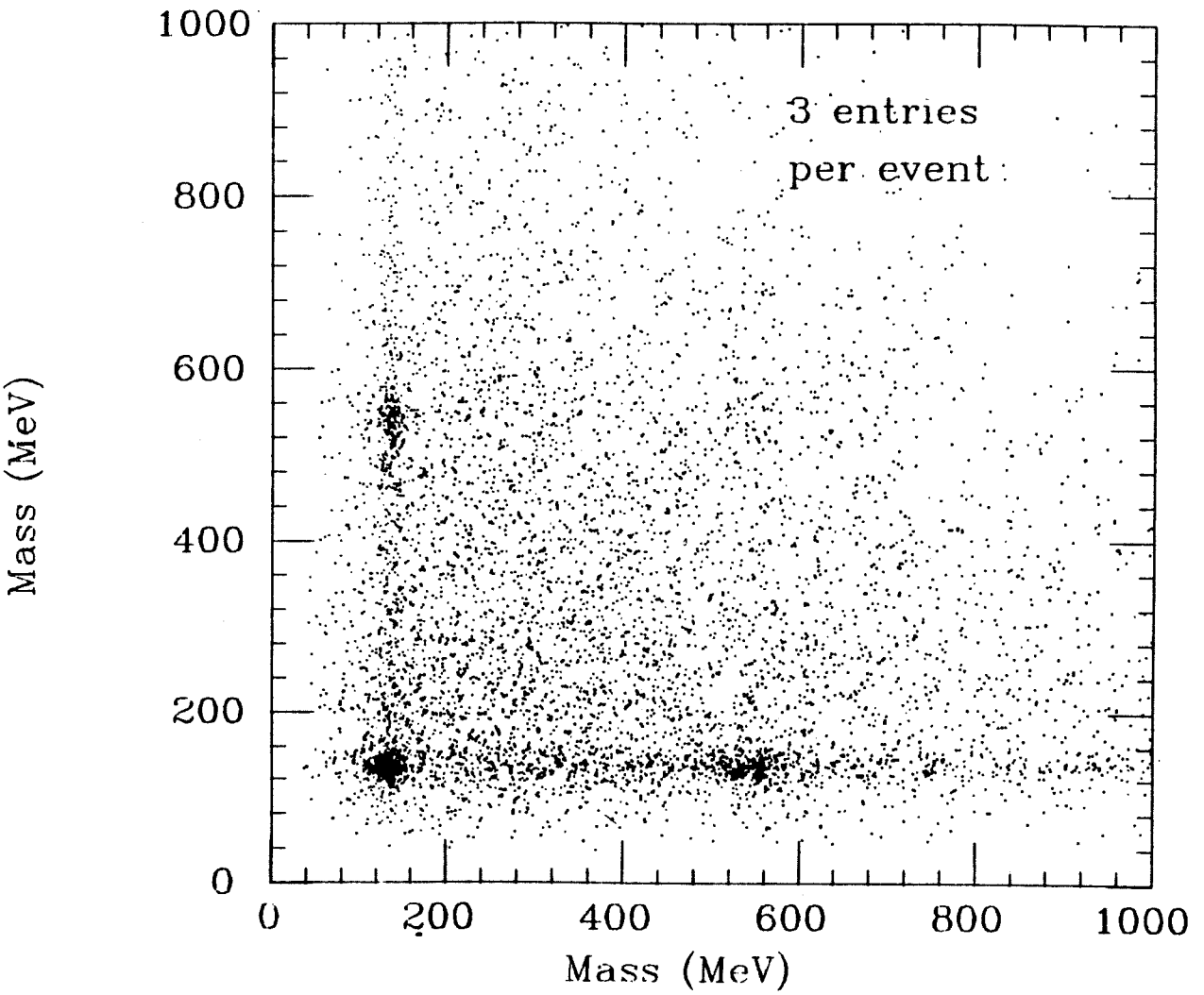

Figure 6.1: $M_{\gamma\gamma}$ vs. $M_{\gamma\gamma}$ before SQUAW fits for 2-charged 4-photon events (three entries per event).

amount of background.

Figure 6.2 shows the SQUAW fit probability for these events. 996 events satisfied a 10% cut on this probability. A prominent π^0 peak is seen in the $\gamma\gamma$ mass distribution for the two photons opposite the η, as shown in Figure 6.3. $\gamma\eta\eta'$ events, on the other hand, should show a fairly flat distribution of $\gamma\gamma$ masses. Thus events are rejected if the mass of the two photons opposite the η is in the range 75-200 MeV. 625 events are removed by this cut, leaving 371 events. Returning for a moment to Figure 6.1, we note once again the large number of $\pi^0\pi^0$ and $\gamma\gamma\pi^0$ events among the 4γ final state. Since there are six ways to choose two photons from among four photons, it is quite possible for some of these events to satisfy the η mass constraint in the kinematic fit by a miscombination of photons. To reject this possibility, the remaining events were also fit to the hypothesis $\psi\rightarrow\gamma\gamma\pi^0\pi^+\pi^-$, $\pi^0\rightarrow\gamma\gamma$. Events were rejected if the $\gamma\gamma\pi^0\pi^+\pi^-$ fit probability was greater than 10%. This cut removed an additional 215 events, leaving 156 events.

One final consideration is contamination of the event sample from $\gamma\eta\pi^+\pi^-$ events in which one of the charged pions generates a splitoff track. Splitoffs can be recognized by several criteria: low energy (usually 20-50 MeV), close proximity to a hadronic shower, and pattern of energy deposition inconsistent with an electromagnetic shower. We have used a combination of cuts to identify splitoffs in the remaining events:

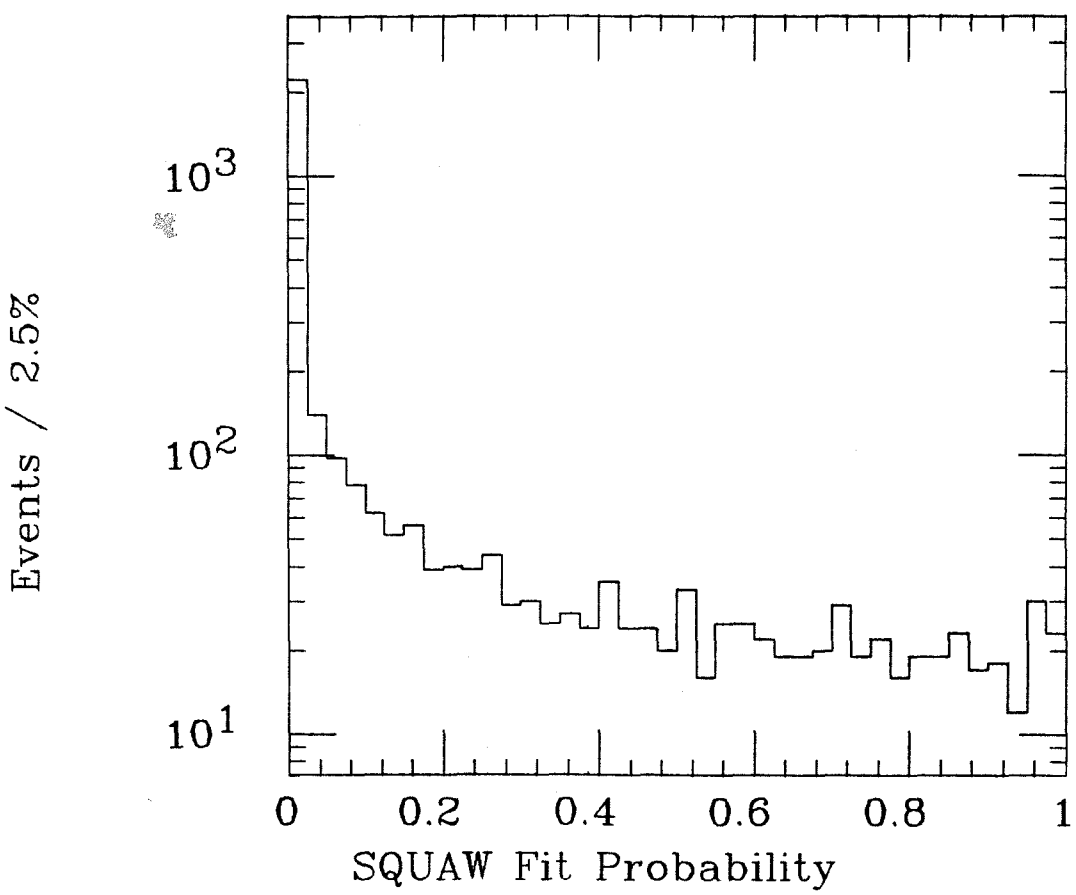

Figure 6.2: SQUAW fit probabilities for $\psi \to \gamma\gamma\eta\pi^+\pi^-$ hypothesis.

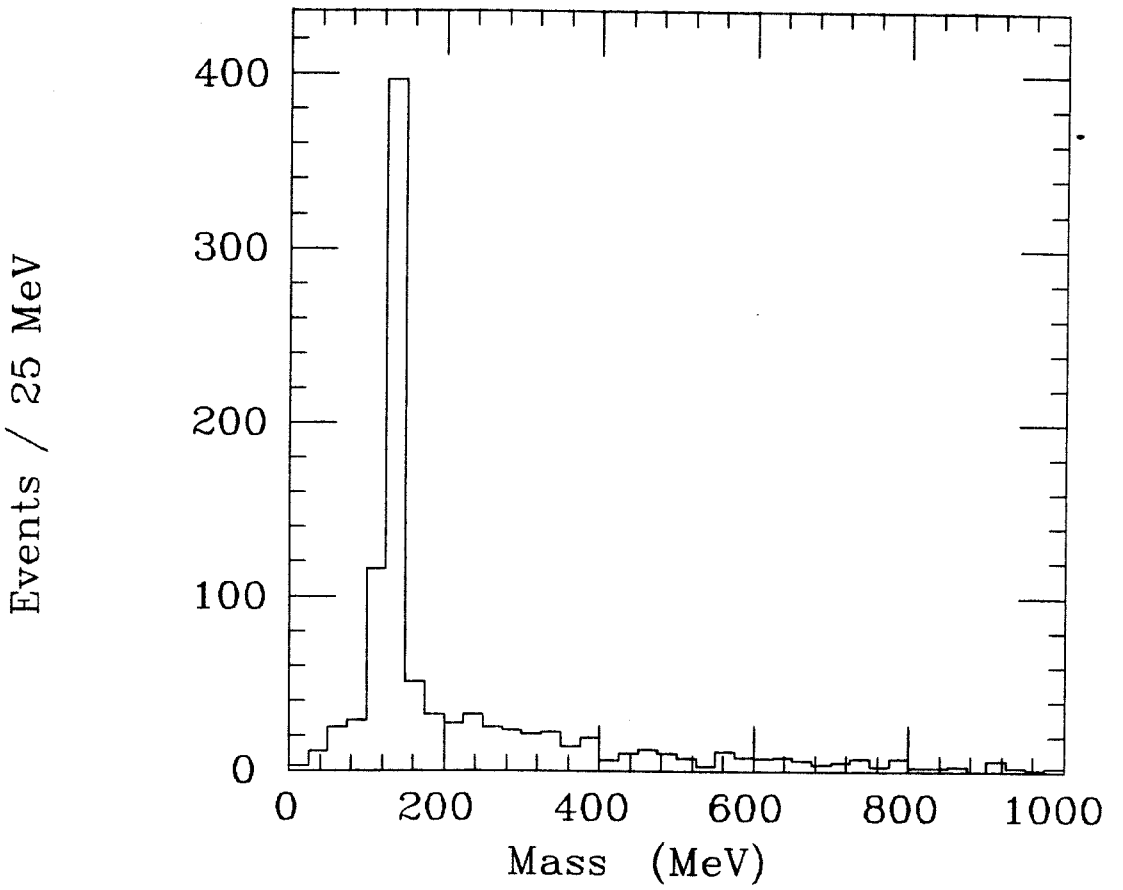

Figure 6.3: $M_{\gamma\gamma}$ opposite the η for $\gamma\gamma\eta\pi^+\pi^-$ events.

1. $E_\gamma < 50$ MeV

2. Pattern cuts: $E1/E4 < .35$ or $E1/E4 > .96$

   $E4/E13 < .75$

3. Splitoff found by SPLIT algorithm.

The SPLIT algorithm [6.7] uses more complicated criteria based on simultaneous consideration of energy, proximity to interacting hadrons, and shower patterns. If any of the three criteria is satisfied, the event is removed from further consideration.

Figure 6.4a shows $M_{\pi\pi}$ vs. $M_{\gamma\pi\pi}$ for the 60 events which remain after removing splitoffs. An η' signal region and two sideband regions have been defined as follows:

η' signal region:	850 MeV $< M_{\gamma\pi\pi} <$ 1050 MeV
	100 MeV $< M_{\gamma\pi\pi} - M_{\pi\pi} <$ 400 MeV
Sideband region:	750 $< M_{\gamma\pi\pi} <$ 850 MeV or 1050 $< M_{\gamma\pi\pi} <$ 1150 MeV
	100 MeV $< M_{\gamma\pi\pi} - M_{\pi\pi} <$ 400 MeV

The choice of these regions was motivated by two facts. First, the two quantities $M_{\pi\pi}$ and $M_{\gamma\pi\pi}$ are not independent. Since in η' decays, most of the η' mass is carried off in the mass of the ρ, an overestimate of the $\pi\pi$ energies (and thus the $\pi\pi$ mass) by the kinematic fit will generally lead to an overestimate of the $\gamma\pi\pi$ mass. Thus, $M_{\gamma\pi\pi}$ and $M_{\pi\pi}$ are quite correlated, particularly as $M_{\pi\pi}$ approaches $M_{\gamma\pi\pi}$. An even more important reason for the way in which these regions are defined is the nature of the background. For splitoff events, the $\gamma\pi\pi$ mass formed using the spurious splitoff photon track will have $M_{\pi\pi} \approx M_{\gamma\pi\pi}$, since the splitoff track typically has low energy and is close to the parent hadron. Although criteria were introduced to remove events with splitoffs, some events

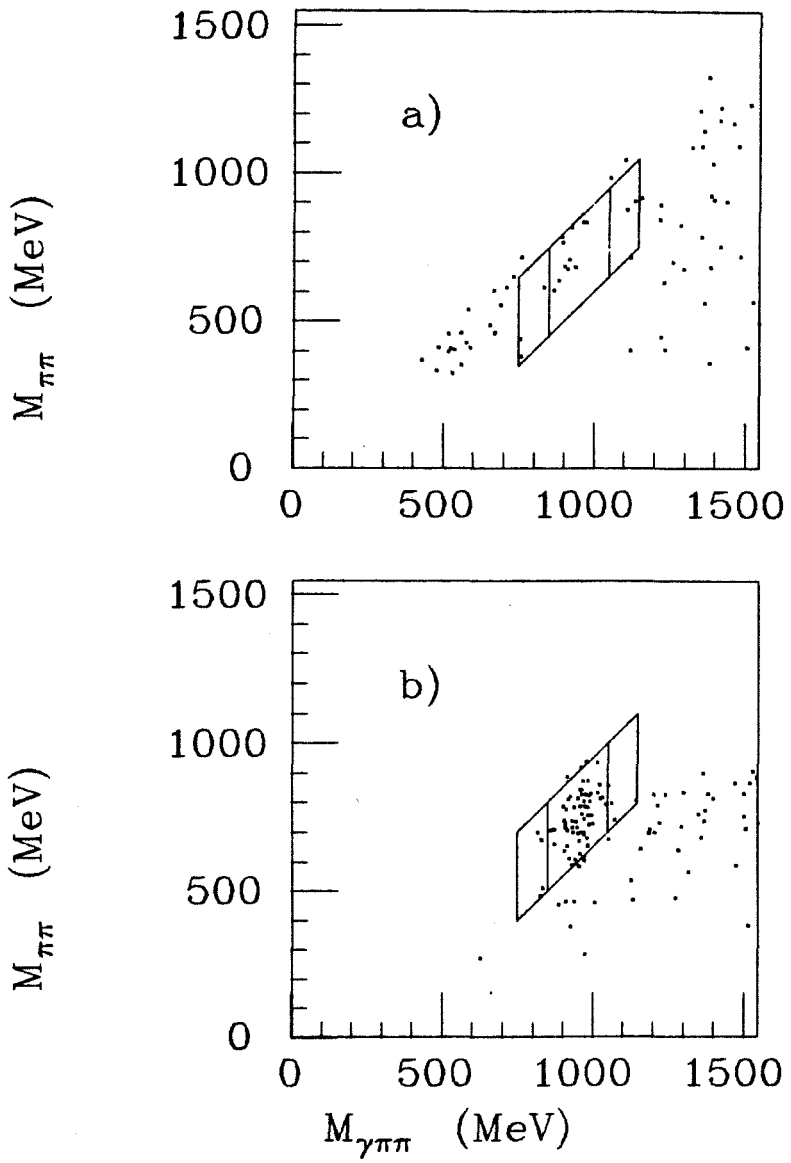

Figure 6.4 $M_{\pi\pi}$ vs $M_{\gamma\pi\pi}$ after splitoff cuts for a) real $\psi \to \gamma\gamma\eta\pi^+\pi^-$ events, and b) $\psi \to \gamma\eta\eta'$ phase space Monte Carlo events. The η' and sideband regions, used to select $\gamma\eta\eta'$ events, are indicated on the plots.

presumably still leak through. Assuming that this residual background is still concentrated along the diagonal band $M_{\pi\pi} \approx M_{\gamma\pi\pi}$, and is relatively flat in $M_{\gamma\pi\pi}$, then the cuts used will ensure that the background will equally populate the signal and sideband regions.

The specific size of these regions was based on a study of $\eta' \to \gamma\rho$ decays using Monte Carlo events as well as real ψ data. The prominent radiative decay $\psi \to \gamma\eta'$ provides one means of studying the $\eta' \to \gamma\rho$ decay using ψ data. Events were fit to the hypothesis $\psi \to \gamma\gamma\pi^+\pi^-$ and rejected if the $\gamma\gamma$ mass was consistent with a π^0 or η. Events were also rejected if either γ appeared to be a splitoff, using criteria similar to the ones described above. Selecting events with $M_{\pi\pi}$ in the range 550-850 MeV yields the $\gamma\pi\pi$ mass spectrum of Figure 6.5a. Fitting this spectrum to a Gaussian gives a mass of 953 ± 2 MeV, and a mass resolution σ = 48 ± 2 MeV. This probably provides an upper limit to the η' mass resolution that we expect to see in $\psi \to \gamma\eta\eta'$. The $\psi \to \gamma\eta'$ process produces an η' with a large momentum $p_{\eta'}$ = 1400 MeV. This causes the η' decay products to emerge in a fairly small cone, and thus angular errors can contribute significantly to the η' mass determination. On the other hand, for $\psi \to \gamma\eta\eta'$, and particularly for $\psi \to \gamma\theta(1700)$, $\theta \to \eta\eta'$, we expect a broad distribution of η' momenta at lower values, leading to larger opening angles among the η' decay products and better mass resolution.

To study η' identification for the $\gamma\eta\eta'$ final state, 1000 Monte Carlo events were generated according to the decay chain $\psi \to \gamma\eta\eta'$, $\eta \to \gamma\gamma$, $\eta' \to \gamma\rho$, and $\rho \to \pi\pi$, using an isotropic phase space distribution for the $\gamma\eta\eta'$ system. Figure 6.5b shows the $\gamma\pi\pi$ mass distribution for these events after applying the same selection criteria as applied to the data, and indeed we see a narrower peak; a fit yields σ = 31 ± 6 MeV. Thus the $\gamma\pi\pi$ mass cut used to define the η' signal region,

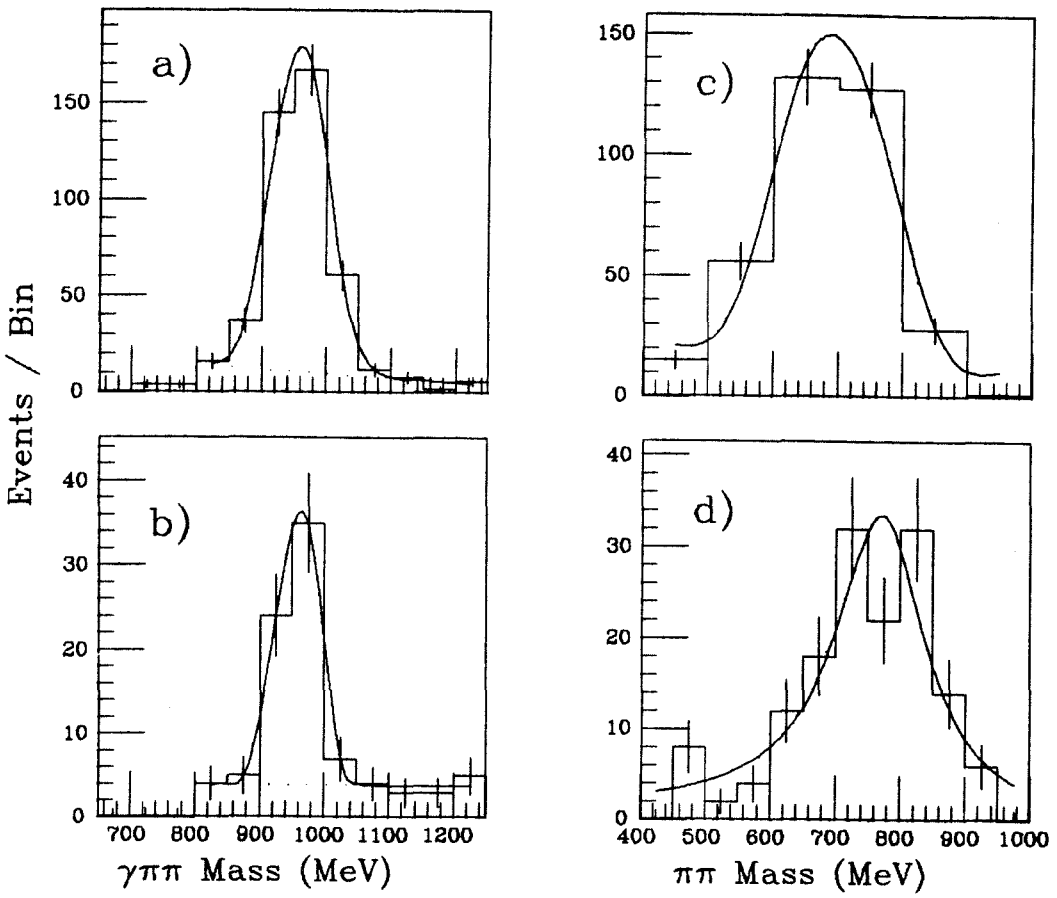

Figure 6.5: Mass distributions used to determine the $\pi\pi$ and $\gamma\pi\pi$ mass cuts employed in selecting η' events:

a) η' mass resolution for real $\psi \to \gamma\eta'$ decays.

b) η' mass resolution for $\psi \to \gamma\eta\eta'$ Monte Carlo events.

c) ρ mass distribution for real $\psi \to \gamma\eta'$ decays.

d) ρ mass distribution for $\psi \to \gamma\eta\eta'$ Monte Carlo events.

$850 < M_{\gamma\pi\pi} < 1050$ MeV, corresponds to 3σ limits based on the phase space Monte Carlo, or 2σ limits based on the $\psi \to \gamma\eta'$ data sample.

The diagonal cut on $M_{\pi\pi}$ vs $M_{\gamma\pi\pi}$ is slightly more complicated, due to the large ρ width and to distortion of the ρ spectrum in η' decays due to phase space effects. Once again, both real $\psi \to \gamma\eta'$ events and Monte Carlo $\psi \to \gamma\eta\eta'$ events were used to study the $\rho \to \pi\pi$ mass distribution. For the ψ data, Figure 6.5c shows the $\pi\pi$ mass spectrum for those events in the $\gamma\gamma\pi^+\pi^-$ dataset with $M_{\gamma\pi\pi}$ in the range 850-1050 MeV. The resonance parameters for a relativistic Breit-Wigner fit are determined to be $M_\rho = 705 \pm 10$ MeV and $\Gamma = 152 \pm 7$ MeV. This low value for the ρ mass is due to the limited phase space in the decay $\eta' \to \gamma\rho$. Since the spin-parity structure of this decay, $0^- \to 1^- 1^-$, implies that the minimum orbital angular momentum is $l=1$, we can expect strong phase space suppression of the high mass side of the ρ distribution. Figure 6.5d shows the $\pi\pi$ mass distribution for the $\gamma\eta\eta'$ phase space Monte Carlo events. The Monte Carlo does not properly treat phase space effects for the $\eta' \to \gamma\rho$ decay, and in fact we see no suppression in the high mass side of the ρ: a fit yields $M_\rho = 770 \pm 10$ MeV and $\Gamma = 170 \pm 20$ MeV.

Based on the ψ data, we define a ρ window $550 < M_{\pi\pi} < 850$ MeV for events at the center of the η' mass region ($M_{\gamma\pi\pi}$=950 MeV), and let this window vary linearly with the $\gamma\pi\pi$ mass. Thus we obtain the diagonal cut $100 < M_{\gamma\pi\pi} - M_{\pi\pi} < 400$ MeV. For determining the efficiency of the analysis for the Monte Carlo $\gamma\eta\eta'$ events, we must shift this window to reflect the improper treatment of the $\eta' \to \gamma\rho$ decay in the Monte Carlo. Thus for the Monte Carlo events, we use the modified cut $50 < M_{\gamma\pi\pi} - M_{\pi\pi} < 350$ MeV, corresponding to a ρ cut of 600-900 MeV at the center of the η' window.

With this justification for the η' and sideband region cuts, we can search for the process $\psi \to \gamma\eta\eta'$. Returning to Figure 6.4a, we find 10 events in the η' signal region, and 5 events in the sideband region. Subtracting the sideband region, we find an excess of 5.0±3.9 $\gamma\eta\eta'$ events. The overall efficiency of this method is determined by passing the Monte Carlo $\gamma\eta\eta'$ events through the same analysis. Figure 6.4b shows the $M_{\pi\pi}$ vs. $M_{\gamma\pi\pi}$ distribution for the Monte Carlo events (with the η' and sideband regions shifted up as described above). Based on the original Monte Carlo dataset of 1000 events, 61 events are found in the signal region, with 7 events in the sidebands. Including a 10% systematic error to account for uncertainties in the Monte Carlo, we arrive at an overall efficiency of 5.4 ± 1.3 %. (This does not include the $\eta \to \gamma\gamma$ and $\eta' \to \gamma\rho$ branching fractions, which we take to be .391 and .300, respectively [6.8].) Thus we conclude that we see no evidence for the process $\psi \to \gamma\eta\eta'$, with a 90% confidence limit

$$BF(\psi \to \gamma\eta\eta') < 8.4 \times 10^{-4}.$$

We can also place a more stringent limit on the process $\psi \to \gamma\theta(1700)$, $\theta \to \eta\eta'$ by examining the $\eta\eta'$ spectrum of events in the η' signal region. Figure 6.6 shows the $\eta\eta'$ mass spectrum for the signal region of a) the ψ data, and b) the $\gamma\eta\eta'$ phase space Monte Carlo. Knowing the original phase space distribution, one can calculate as a function of $\eta\eta'$ mass the efficiency for $\gamma\eta\eta'$ events to survive all cuts and lie in the η' signal region. This efficiency is plotted in Figure 6.7. It is a fairly flat function of $\eta\eta'$ mass, and takes the value 5.1±1.5% in the mass range 1500-1900 MeV. The $\eta\eta'$ mass spectrum of Figure 6.6a has been fit to a relativistic Breit-Wigner centered at 1700 MeV, with Γ= 150 MeV, plus a phase space distribution whose shape is determined by a fit to the Monte Carlo $\eta\eta'$ mass spectrum of Figure 6.6b. Demanding a non-negative number of events for

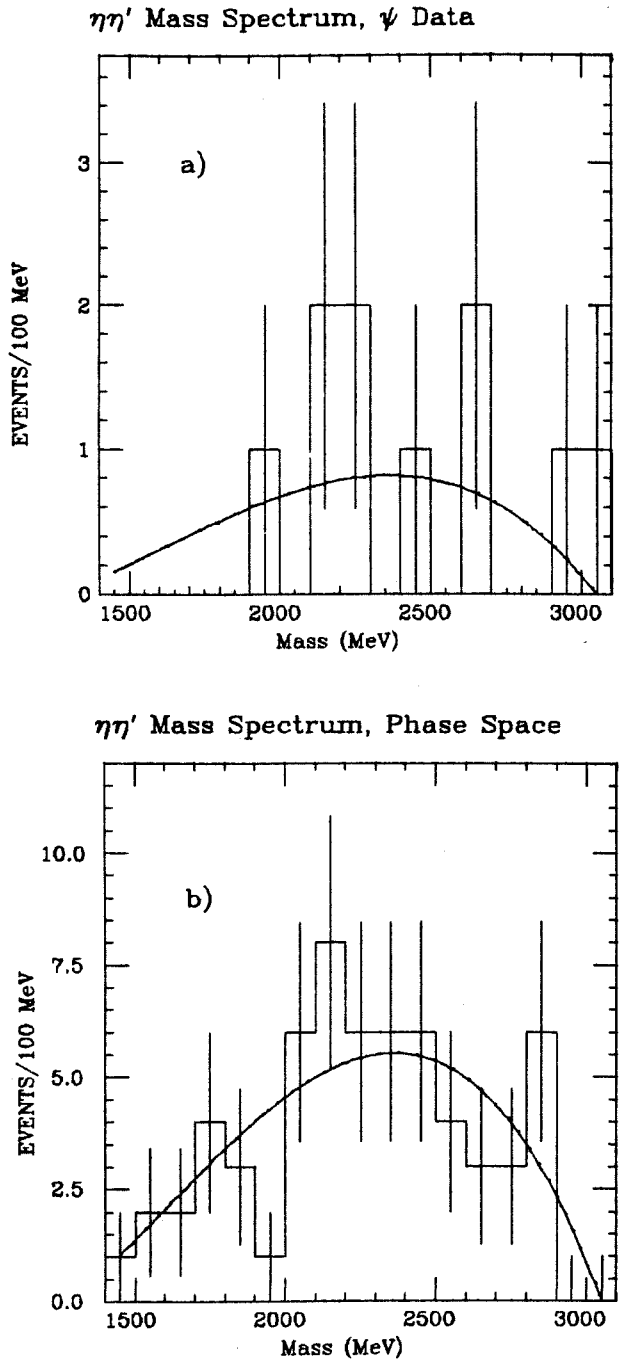

Figure 6.6: $M_{\eta\eta'}$ in $\psi \to \gamma\eta\eta'$, for a) data, and b) Monte Carlo. The polynomial fit to the Monte Carlo phase space distribution of Figure 6.6b is used as the background shape for Figure 6.6a. The fit in 6.6a also includes a term for the $\theta(1700)$.

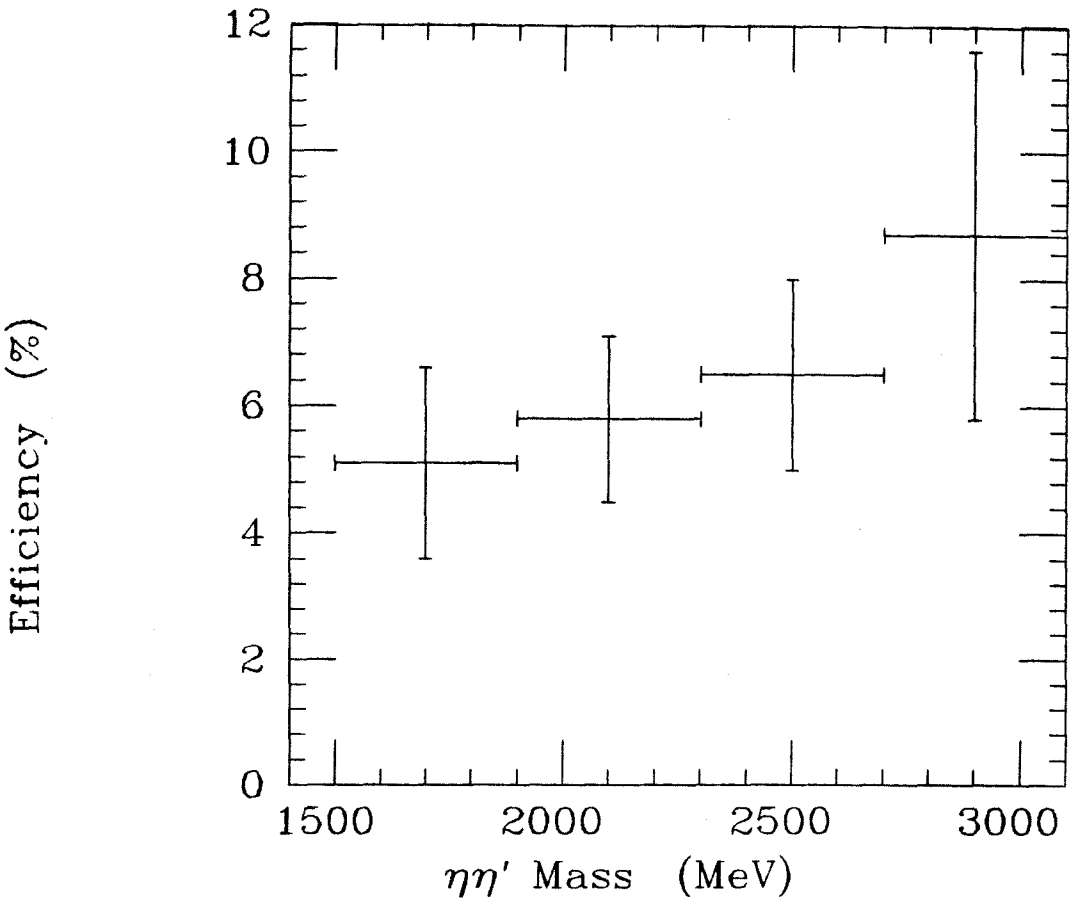

Figure 6.7: Efficiency for $\psi \to \gamma\eta\eta'$ Monte Carlo events to survive all cuts, including η' identification, as a function of $\eta\eta'$ mass.

the signal, the best fit is obtained for zero signal events, allowing us to set a 90% confidence level limit for the $\theta \rightarrow \eta\eta'$ decay:

$$BF(\psi \rightarrow \gamma\theta) \times BF(\theta \rightarrow \eta\eta') < 2.1 \times 10^{-4}$$

and on the ratio

$$\frac{\Gamma(\theta \rightarrow \eta\eta')}{\Gamma(\theta \rightarrow \eta\eta)} < 0.63 \qquad (90\% \text{ C.L.}).$$

This is well below the predicted ratio of 2.09 predicted by Schechter's model in the case of constructive interference.

6.4 Conclusions

We have searched for the decay $\psi \rightarrow \gamma\eta\eta'$ in an effort to study the $\eta\eta'$ decay mode of the $\theta(1700)$. Within the context of an effective Lagrangian model, we have seen how glueball - η_0' mixing could lead to an enhancement of the $\theta \rightarrow \eta\eta'$ decay rate well above naive phase space considerations. An analysis of the data, however, shows no $\gamma\eta\eta'$ signal, permitting limits to be placed on the process $\psi \rightarrow \gamma\eta\eta'$ and on the ratio of the $\eta\eta'$ to the $\eta\eta$ decay modes of the θ. This rules out the constructive interference solution of Schechter's model.

Chapter 6 References

[6.1] C. Edwards *et al.*, Phys. Rev. Lett. 48, 458 (1982). E. Bloom, Rapporteur talk presented at the International Conference on High Energy Physics, Paris, SLAC-PUB-3005, 1982.

[6.2] J. Schechter, Phys. Rev. D27, 1109 (1983).

[6.3] M. Franklin, Ph.D. thesis, SLAC-Report 254, 1982.

[6.4] W. Toki, invited talk given at the 1983 SLAC Summer Institute on Particle Physics.

[6.5] J. L. Rosner and S. F. Taun, Phys. Rev. D27, 1544 (1983).

[6.6] J. L. Rosner, Private communication, 3/15/84.

[6.7] K. Koenigsmann and F. Bulos, Crystal Ball Note No. 154, 1980 (unpublished).

[6.8] Particle Data Group, Phys. Lett. 111B, 1982. The Meson Table entry for the f' lists the $K\overline{K}$ mode as "dominant."